Trinity College Dublin
Coláiste na Tríonóide, Baile Átha Cliath
The University of Dublin

Beneath the Surface: Mathematical Perspectives on Flows Generated by Submarine Volcanic Eruption in Stratified Oceans

Manish Kanojia

kanojiam@tcd.ie

Faculty of Science, Technology, Engineering and Mathematics

Doctor of Philosophy

February 20, 2025

Declaration

I declare that this thesis has not been submitted as an exercise for a degree at this or any other university and it is entirely my own work.

I agree to deposit this thesis in the University's open access institutional repository or allow the Library to do so on my behalf, subject to Irish Copyright Legislation and Trinity College Library conditions of use and acknowledgement.

I consent to the examiner retaining a copy of the thesis beyond the examining period, should they so wish (EU GDPR May 2018).

Manish

Signature

Acknowledgments

I would like to express my gratitude and appreciation to Professor Biswajit Basu and Professor Amala Mahadevan, my supervisors, for their unwavering encouragement and support throughout my research. Their guidance and advice were instrumental in helping me navigate all stages of my project. Additionally, I am thankful to the Government of India's Ministry of Social Justice and Empowerment for financing my research through the National Overseas Scholarship, as well as to my colleagues Saravanan Gurusamy and Conor O'Reilly who generously provided me with their time and invaluable feedback.

Lastly, I am deeply grateful for the unwavering support and blessings of my family, my mother, Mrs. Asha Kanojia, my father, Mr. Sushil Kanojia, and my brother, Saurav Kanojia. I also would like to extend my heartfelt thanks to my friends Inderjeet Singh, Kumar Utkarsh, and Amrutha, whose constant encouragement, positivity, and companionship have been invaluable to me throughout this journey.

Contents

Abstract

This thesis addresses critical gaps in understanding the fluid dynamics generated by submarine volcanic eruptions in both shallow and deep ocean environments. The research utilizes a combination of analytical and numerical models in two and three dimensions, integrating heat and mass flux associated with volcanic activity within stratified ocean systems. For deep-sea eruptions, the primary focus is on developing a comprehensive three-dimensional framework to analyze flow dynamics, with particular attention to the generation of convective flows. The influence of oceanic stratification, specifically temperature and salinity gradients, is systematically investigated to elucidate their role in modulating convective flow patterns and shaping complex marine processes. The research further investigates how different stratification intensities ranging from strong to weak affect the behavior of volcanic plumes, as well as the rotational dynamics that develop during sustained or gradual eruptions.

A significant component of the study involves examining how variations in ocean stratification, which are increasingly affected by climate change and rising sea surface temperatures, alter the generation and propagation of tsunamis triggered by submarine eruptions. This aspect is explored using a two-dimensional potential theory model to analytically evaluate the impact of stratification on tsunami wave dynamics. Also, a 3-dimensional computational model is used to generate gravity waves by applying a high heat flux at the seabed in a shallow environment. In addition, the study presents a detailed analysis of the influence of submarine volcanic activity on equatorial oceanic flows. This is accomplished by applying an established model for equatorial ocean dynamics, deriving analytical solutions for flow velocities, and examining the interaction between volcanic-induced perturbations and ambient currents.

To simulate complex three-dimensional processes, the Process Study Ocean Model

(PSOM) is employed, incorporating the effects of thermal and salinity stratification and heat flux in both deep and shallow oceanic settings. These simulations provide insight into the interplay between submarine volcanic activity and broader ocean circulation, contributing to a more refined understanding of how such eruptions influence oceanic flows and potentially impact global marine systems.

This thesis contributes to a deeper understanding of submarine volcanic phenomena, providing new insights into how stratification modifies flow dynamics and surface wave formation, with implications for predicting the impacts of volcanic eruptions in changing oceanic conditions.

List of Figures

Chapter 1

Introduction

The deep sea is the largest museum on earth, it contains more history than all the museums on land combined, and yet we're only now penetrating it.

— Robert Ballard

Volcanic eruptions serve as pivotal mechanisms in the dynamic processes of magma genesis and crustal accretion within the Earth's geological framework. Operating across temporal scales from transient events lasting mere hours to transformative processes unfolding over years, these eruptions facilitate the deposition of newly formed lava and fragmented ejecta. They also transmit thermal energy and magmatic volatiles from the subterranean depths to the overlying atmosphere or aqueous environments, instigating significant alterations to the surrounding terrain morphology and perturbations to local ecosystems. Approximately 80 % of volcanic activity on Earth occurs beneath the ocean's surface, predominantly concentrated along subduction zones and mid-ocean ridges within the geodynamic framework [7]. The intricate interplay of deep-seated mantle dynamics governs this phenomenon, profoundly influencing the chemical and bio-geochemical dynamics of the global oceans. Submarine volcanic eruptions are intricately linked with hydrothermal processes, accompanied by the release of high-temperature magmatic gases. This complex phenomenon engenders both perilous hazards and promising prospects for future endeavors, catalyzing discourse on mineral deposit formation and the contentious domain of marine resource exploitation [8].

Hydro-thermal activity also supports an astonishing diversity of seafloor vent ecosystems influencing global carbon and nutrient cycles [9, 10]. Most of the known modern seafloor hydro-thermal systems, with their associated mineral deposits and chemo-synthetic microbial biomes, occur at MORs and mature back–arc spreading centers, typically at water depths of 2000 to 4000 meters [11, 12]. Five new hydrothermal vents have been identified recently along the East Pacific Rise (EPR) in close proximity to the 10°N latitude. Situated within the extensive mid-ocean ridge system, these vents emerge where two tectonic plates diverge at a rate of approximately 11 centimeters (4.3 inches) annually [13]. The discovery of these novel sites, coupled with the examination of rock samples, offers an unprecedented opportunity for scientists to elucidate the velocity and trajectory of lava eruptions, as well as to comprehend the profound implications of deep-sea lava emissions on hydrothermal vent dynamics. This is particularly significant given the inherent challenges associated with detecting and observing submarine eruptions at depths exceeding 500 meters [14]. Such investigations contribute invaluable insights into the complex interactions between volcanic activity and hydrothermal systems within the deep ocean environment.

Subaquatic volcanoes located within 500 meters of the ocean's surface possess the potential for immense explosions [15]. The eruption of the Tonga volcano in January 2022 stands out as the most explosive event of its kind in the past three decades. A significant contributing factor to this eruption's magnitude is attributed to the shallow depth of the volcano's crater, estimated to be within the upper 200 meters from the ocean's surface [15, 16]. In shallow water eruptions, when the molten lava interacts with the ocean water, an almost instantaneous conversion into steam occurs. This rapid phase transition results in an exponential expansion, as steam occupies over 1000 times the volume of liquid water. Consequently, the sea water's transformation into steam disrupts the lava into smaller fragments. These fragments subsequently collide with other areas of liquid water, inducing further steam generation. This cascading effect, known as the runaway effect, significantly contributes to the heightened intensity observed in the Tonga volcanic eruption. The resultant tsunami, triggered by the Tonga volcanic eruption, propagated across vast expanses, impacting regions including Tonga, Fiji, American Samoa, Vanuatu, and the broader Pacific rim. This included the generation of far-field tsunamis which inflicted damage in distant locations such as New Zealand, Japan, the United States, the Russian Far East, Chile, and Peru.

Marine life is often attracted to and thrives around the sights of volcanic eruptions [17]. During studies of the volcanoes near Guam, scientists discovered a notable increase in the population of animals inhabiting the summits of these volcanoes, including shrimp, crabs, and barnacles. These organisms flourish in the harsh, chemical-filled circumstances that prevail atop undersea volcanoes, deriving nutrition from the eruptive magma/tephra [17]. Additionally, hydrothermal vents, abundant in chemicals, serve as energy sources for animal life, fostering rich and productive ecosystems. This discovery has reshaped scientists' understanding of the conditions capable of supporting life on Earth and potentially elsewhere in the solar system. It underscores the importance of learning more about volcanic and hydrothermal systems in the deep sea, where new seafloor is formed, and unique communities of animals thrive in high-pressure and high-temperature environments. Exploring these dynamic ecosystems can provide valuable insights into the origins and sustenance of life in extreme environments, shedding light on the broader questions of habitability and biodiversity in the universe.

There is a substantial dearth of observational data regarding submarine volcanoes deep beneath the ocean's surface. This scarcity primarily stems from several formidable challenges. Firstly, the immense pressure at great depths necessitates specialized and costly equipment capable of withstanding extreme conditions. Secondly, the high temperatures emitted by submarine volcanoes can harm equipment and pose safety hazards. Moreover, the unpredictable nature of volcanic activity, including eruptions and releases of toxic gases, complicates close observation and data collection efforts. Accessibility is another significant hurdle, with many submarine volcanoes situated in remote and difficult-to-reach locations, requiring extensive logistical planning and financial investment. Additionally, current underwater drones, sensors, and other equipment are still evolving to meet the demands of deep-sea exploration, posing technical limitations. The overall expense of such missions is prohibitive, restricting their frequency and scale. Furthermore, transmitting data from deep-sea environments to the surface is challenging due to signal absorption and scattering in water, necessitating robust data storage and retrieval systems.

The considerable lack of observational data on submarine volcanoes deep below the surface significantly impedes the study of these geological features. This limitation poses challenges in accurately assessing volcanic hazards in underwater environments, potentially affecting marine ecosystems and underwater infrastructure. Moreover, the scarcity of data restricts the study of submarine volcanoes' roles in global geochemical cycles, vital for understanding Earth's climate dynamics and ecosystem health. However, advancements in technology, such as improved remotely operated vehicles (ROVs), autonomous underwater vehicles (AUVs), and better sensor systems, alongside international collaborations, are gradually enhancing our ability to study submarine volcanoes.

1.1 Aim

This thesis seeks to address key gaps in the current understanding of the flows generated by submarine volcanic eruptions in both shallow and deep ocean environments. The research focuses on developing analytical and numerical models in both two and three dimensions, incorporating the heat and mass fluxes generated by submarine volcanic eruptions in stratified ocean systems. In the case of deep ocean volcanic eruptions, one of the primary aim is to provide a comprehensive three-dimensional flow analysis, examining the mechanisms behind plume formation. Additionally, the study will assess how temperature and salinity stratification influence convective flow patterns in these dynamic marine environments. To further extend this, the study will examine how ocean stratification, driven by climate change and rising sea surface temperatures, affects the generation and propagation of tsunamis triggered by submarine eruptions.

1.2 Central research questions

This thesis will be centered around the following central research questions:

RQ1 : What kind of rotational, buoyant and horizontal flows are produced by the gradual eruption of underwater volcanoes located deep beneath in the stratified ocean?

RQ2 : How does the intensity of stratification (strong versus weak) influence the buoyant rise of the plume?

RQ3 : What kind of rotational motion is generated by gradual volcanic eruptions deep beneath in the stratified ocean?

RQ4 : How do submarine volcanic eruptions affect equatorial oceanic flows?

RQ5 : How are surface waves generated by shallow submarine volcanic eruptions influenced by the ambient pycnocline in the ocean?

1.3 Objectives

RO1 **Numerical modeling:** To utilize Process Ocean Study Model (PSOM) [18, 19] to simulate submarine volcanic eruptions occurring deep within stratified oceans. The model will incorporate ocean stratification in terms of temperature and salinity, along with heat flux at the seabed, to investigate the convective flows generated by these volcanic eruptions. A full 3-dimensional analysis of these flows will be carried out, and the impact of stratification intensity on the vertical ascent of the plume in two stratified cases will be studied.

RO2 **Free surface disturbances:** To investigate the impact of gradually erupting volcanoes deep in the oceans on free surface disturbances, focusing on two cases defined by stratification related to temperature and salinity.

RO3 **Impact on equatorial oceanic flows:** To develop a 3-dimensional model based on the methodologies in [20, 21] and derive analytical solutions to study the impact of submarine volcanic eruptions on equatorial oceanic flows.

RO4 **Impact of stratification on surface waves:** To develop a 2-dimensional linear model using potential function theory and the displacement potential function to model submarine volcanic eruptions. This model will incorporate ambient stratification (thermocline/pycnocline) in the ocean to study the impact of stratification on the surface waves generated by large submarine volcanic eruptions in shallow environments.

RO5 **Heat flux to ignite surface waves:** To introduce large heat flux in a shallow environment to generate surface waves from submarine volcanic eruptions using ocean flow models such as the Process Study Ocean Model (PSOM).

1.4 Overview of the thesis

This thesis is divided into nine chapters.

Chapter 1 presents a general introduction to submarine volcanic eruptions and the phenomena associated with these eruptions, including tsunamis, their impact on and harboring of marine life, hydrothermal vents, and the economic and geopolitical implications of these events. It also outlines the aims, objectives, and central research questions of this work.

Chapter 2 reviews the existing literature related to submarine volcanic eruptions and other oceanography-related topics utilized in this study, providing a critical evaluation of previous research.

Chapter 3 introduces the general fluid dynamic equations (mass conservation, conservation of momentum, heat equation etc.) used to model fluid flow and discusses various approaches to modeling submarine volcanic eruptions, along with some challenges inherent in modeling such phenomena.

Chapter 4 provides an introduction to a geophysical model designed to study ocean flows. This model is developed using the equations presented in Chapter 3, and the incorporation of a volcanic eruption into the PSOM model is also discussed. Additionally, some applications of the PSOM model are reviewed, which proved useful in setting up the PSOM experiment conducted as part of this study.

Chapter 5 and 6 focus on studying sub-aquatic flows generated by submarine volcanic eruptions. **Chapter 5** applies the model developed in Chapter 4 to numerically simulate deep and gradual submarine volcanic eruptions by introducing heat flux at the seabed in two stratified scenarios: one based on temperature and the other on salinity. These simulations cover regions spanning mid to high latitudes. Chapter 5 examines the rotational, radially convective, and vertical flows generated by these eruptions. The local surface elevation in the two stratified cases is compared, and the impact of stratification intensity on the buoyant rise of the plume is discussed.

The focus in **Chapter 6** shifts to developing a model to study the impact of these eruptions on equatorial oceanic flows and deriving analytical solutions for flow velocities. The submarine eruption is incorporated by appropriately modifying the density function, after which the Constantin-Johnson model for equatorial ocean flows is employed to study the resulting dynamics including the ambient stratification. The developed three-dimensional nonlinear model includes terms accounting for the Coriolis effect and adheres to the β-plane approximation. Exact solutions are obtained using an asymptotic system of equations.

Chapter 7 and 8 explore the flows generated on the free surface by submarine volcanic eruptions in stratified domains. **Chapter 7** develops a two-dimensional model that incorporates ambient stratification and a velocity potential source function to examine the impact of submarine volcanic eruptions on the free surface in a stratified environment. Analytical solutions are derived for cases with and without stratification, with the velocity potential source function applied at the seabed. Surface elevations are plotted and compared for both scenarios. The impact of the volcanic source's distance from the free surface and the size of the volcano on surface elevation is also discussed.

Chapter 8 presents an alternative approach to modeling surface waves generated by submarine volcanic eruptions. The three-dimensional nonlinear PSOM model introduced in Chapter 4 is employed to study these gravity waves. By introducing a large heat flux at the seabed in a shallow environment with a pycnocline, Chapter 8 examines the impact of convective flows on the free surface. The study compares the effects of varying eruption intensities at the same depth on the free surface and explores the impact of eruptions of the same intensity occurring at different depths.

Finally, **Chapter 9** summarizes the conclusions of this research, highlighting the major findings from Chapters 5, 6, 7, and 8. Broader implications and potential applications of the work are discussed, along with possible directions for future research based on the findings presented in this thesis.

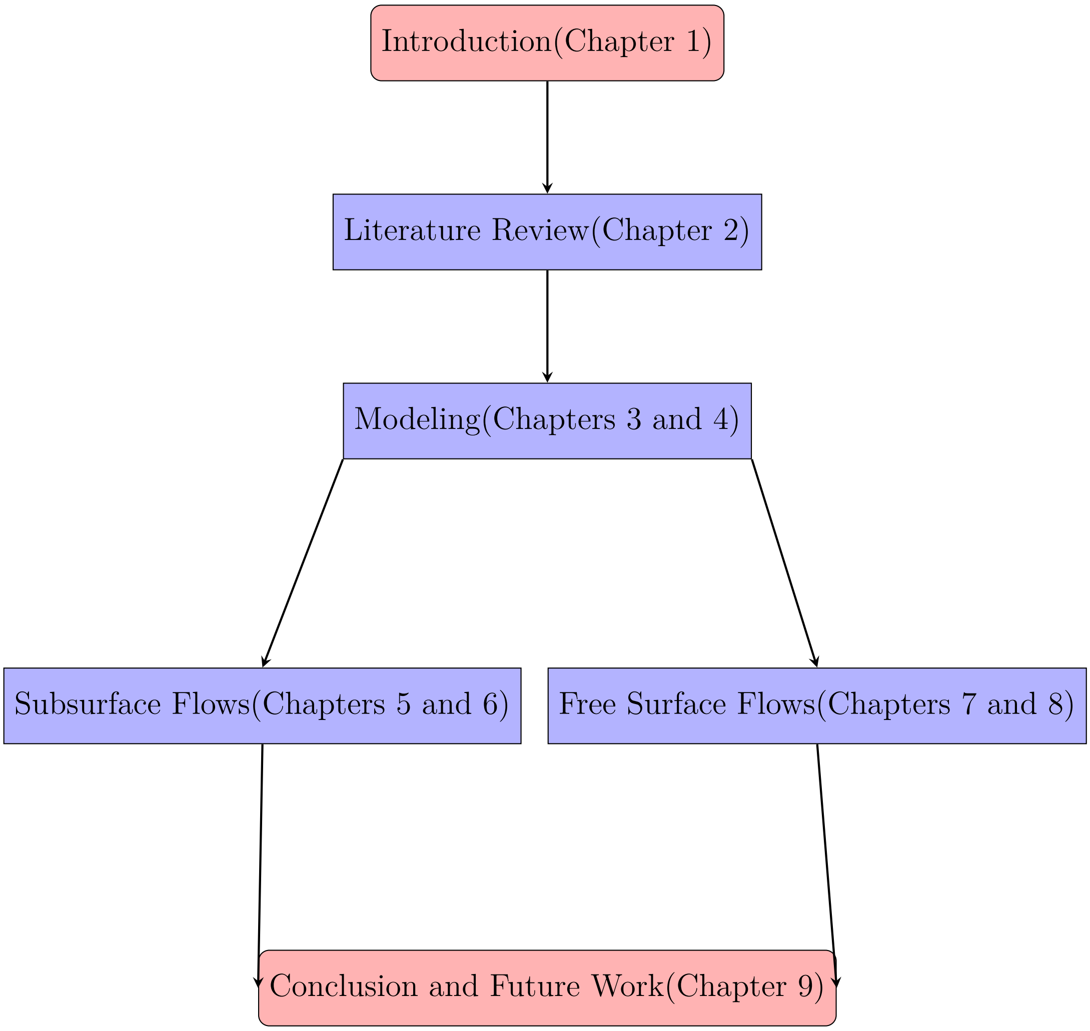

Chapter 2

Literature Review

2.1 Submarine volcanoes

Submarine volcanoes, often known as underwater volcanoes, are cracks or fissures on the earth's surface that are located underwater. These underwater volcanoes behave similarly to those on land. They have the ability to erupt and create magma. There are thousands of submarine mountains throughout the deep ocean, and nearly all of them are volcanoes [22]. They form long continuous ridges along the extended centre of the seafloor, arcuate chains along the subduction zone, and both linear chains away from plate boundaries and widely distributed individually on seafloors. Submarine volcanism is one of the most important geological processes on the planet, forming a dense, low-lying, igneous crust that floors the vast ocean basins and covers nearly two-thirds of Earth's surface. Studies on active volcanoes around the Earth provide important information for understanding the extent of volcanic activity in different environments, but they focus on the aerial environment. Deep-sea eruptions are much more difficult to detect and observe than aerial eruptions, but knowledge on these eruptions is growing rapidly [6, 23, 24, 14].

The most famous collection of underwater volcanoes is part of the Ring of Fire. It is an area in the basin of the Pacific Ocean in which an unusually high number of eruptions and earthquakes occur. In the ring, there are volcanic arcs and belts, as well as plate movement. There are approximately 452 volcanoes present in the ring [17]. Some of the submarine volcanoes which are part of Ring of Fire lie in the equatorial region in the Pacific and Indian Ocean (see Figure 2.1).

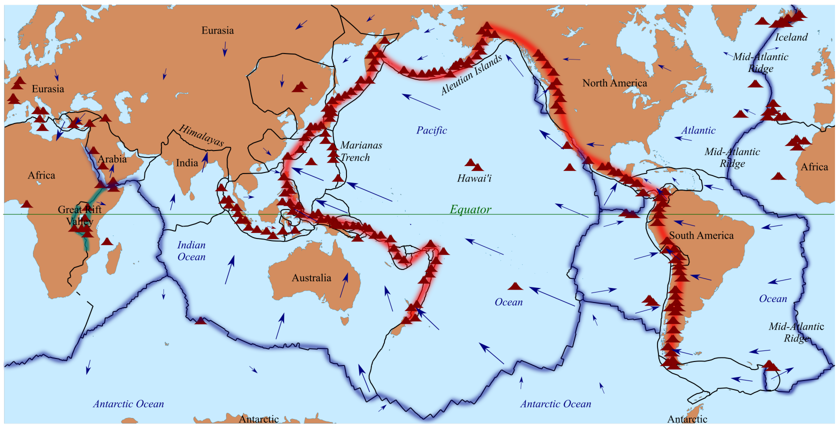

Figure 2.1: Land and submarine volcanoes in the ring of fire. Figure also depicts the presence of submarine volcanoes in the equatorial region. Image source: Ring of Fire Astroskiandhike CC BY-SA 4.0, via Wikimedia Commons.

Loihi Seamount, situated approximately 35 km southeast of the Big Island of Hawaii, has long served as a pivotal case study in understanding volcanic processes. The diverse range of basalt compositions found at Loihi has significantly reshaped our understanding of the compositional evolution of Hawaiian and other oceanic islands. Additionally, the discovery of various volcaniclastic materials, spanning from glassy ash to basalt breccias, has enriched our knowledge of volcanic activity in such environments [25, 26]. Despite its scientific importance, conducting regular and detailed observations of Loihi has posed significant challenges. The seamount's peak, located nearly 1000 m below sea level, presents formidable obstacles to comprehensive observation efforts, primarily due to the associated high costs involved.

The summit of the active submarine volcano Monowai, located in the Kermadec Arc north of New Zealand, undergoes episodic elevation changes near the water surface, fluctuating rapidly over periods ranging from weeks to decades. These fluctuations are attributed to recurring cycles of volcano growth and swift flank collapse [27, 28]. Monowai exhibits exceptionally high rates of growth and collapse, with volume changes estimated at 0.11 km^3 per year for collapse and 0.63 km^3 per year for growth. Notably, the 2011 lava eruption of Axial Seamount, situated at the convergence of the Cobb hotspot and the Juan de Fuca spreading center, was anticipated through meticulous monitoring initiated after its 1998 eruption [29]. Furthermore, active Vailulu'u Seamount, in close proximity to the Samoa hotspot and currently submerged at a depth of 590 meters, is experiencing such rapid growth that it is projected to breach the ocean surface within decades [30].

The 2011–2012 submarine eruption off the coast of El Hierro in the Canary Islands represents a unique event due to its proximity to land and the shallow depth at which it occurred. This allowed for convenient monitoring and extensive studies, distinguishing it from similar eruptions in the Pacific Ocean. The eruption, which occurred approximately 2 km off the southern coast of the island, led to the formation of a new volcanic structure that underwent significant morphological changes over a four-month period, evolving from a single cone into a linear array of four cones. Collapse of the edifice accompanied its rise, with streams of debris moving down the valley in which the volcano was growing. The total volume of the volcanic complex was estimated at 329×10^6 m^3, with the actual cone constituting one third of this volume. Notably, more than 200 similar cones have been identified on the submarine flanks of El Hierro. Seismic activity preceding the eruption began in July 2011, with earthquakes increasing in magnitude and migrating southward over subsequent months. These seismic events were interpreted as reflecting magma migration from the upper mantle to crustal depths, followed by relaxation around the magma reservoir [31, 32].

The Hunga Tonga-Hunga Ha'apai volcano, part of the Tonga archipelago in the South Pacific Ocean, has a history of eruptions dating back to 1912, with notable events occurring in 1937, 1988, 2009, and 2014-2015. The volcano consists of two small uninhabited islands located approximately 65 km from Tonga's capital, Nuku'alofa. In December 2021 and January 2022, the volcano experienced significant explosive eruptions, with plumes reaching heights of up to 20-30 km. These eruptions triggered tsunami warnings, and a minor tsunami was observed on 14th January 2022. The subsequent massive eruption on 15th January 2022 resulted in a powerful shock wave felt across nearby countries and even heard as far away as New Zealand, Alaska, and Canada. The shockwave propagated globally and was detected by weather stations around the world, highlighting the extraordinary scale of the event. The eruption, described as a once-in-a-thousand-year event, led to significant atmospheric disturbances, with pressure waves observed circling the Earth multiple times. The United

States Geological Survey (USGS) estimated the preliminary magnitude of the events as 5.8, and active seismicity in the region was recorded leading up to the eruption [33].

The 1850 tragedy involving the French warship Bayonnaise and the Beyonesu Rocks epitomizes the inherent risks associated with maritime exploration in volcanic regions. Situated within the largely submerged Myojinsho caldera, the Beyonesu Rocks represent a fragment of the caldera's rim, concealing a turbulent subaqueous landscape characterized by volcanic unrest. The ill-fated encounter occurred amidst the vessel's surveying expedition of volcanic islands south of Tokyo Bay, where the unsuspecting crew found themselves amidst the volatile realm of Myojinsho. The eruption, shrouded beneath the tranquil surface of the ocean, unleashed submarine pyroclastic flows, which swiftly overwhelmed the Bayonnaise, resulting in the tragic loss of all 31 souls aboard [34]. This poignant event underscores the imperative for a comprehensive understanding of volcanic hazards and their implications for maritime activities. The Bayonnaise tragedy stands as a sobering reminder of the profound interplay between human exploration and the formidable forces of nature, enriching the discourse on the complex dynamics of volcanic risk management in maritime contexts.

2.2 Ocean stratification

The distribution of water layers in bodies is determined by temperature and salinity. The uppermost layer, called the epipelagic zone or sunlight zone, interacts with wind and waves, promoting water mixing and heat distribution. Below this zone lies the thermocline, which separates the warmer mixed surface water from the cooler deep water. The thermocline is characterized by a rapid temperature drop from the mixed layer to the colder deep water. The depth and intensity of the thermocline vary seasonally and regionally, with semi-permanence in tropical regions, variability in temperate zones (usually deepest in summer), and shallowness or absence in polar regions where the water column remains cold throughout.

Another form of stratification is found in estuaries and coastal waters, where a layer of low-salinity water, produced by river flowing into the sea, lies on top of the layer of salty water. The interface between the low- and high-salinity water is called a halocline. Stratification can therefore be produced by temperature and salinity and sometimes by both acting together. The interface between the water of different density is called pycnocline.

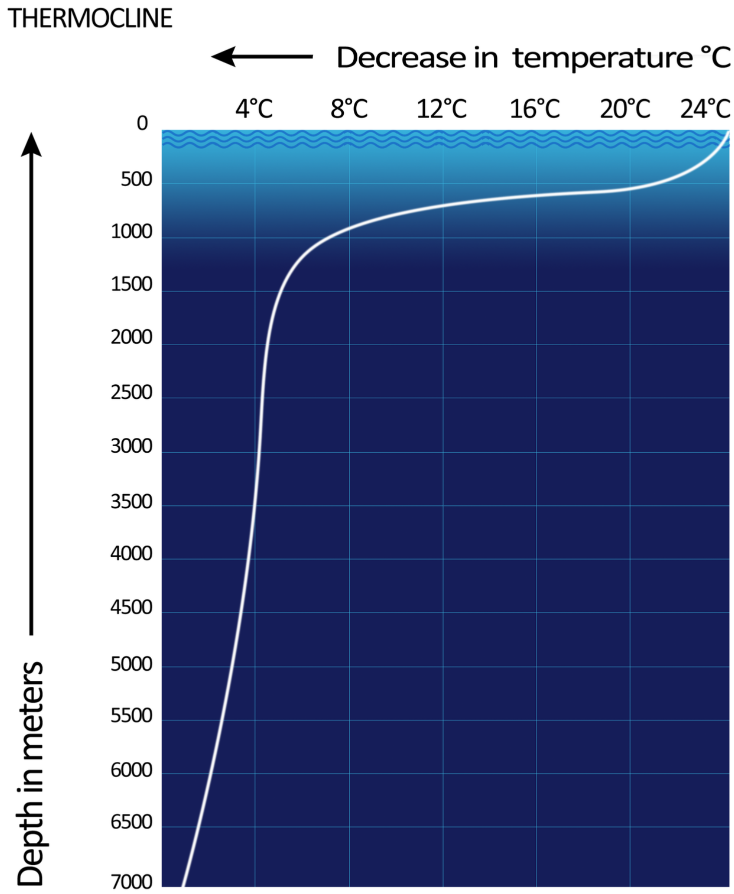

Figure 2.2: Graph illustrating the temperature-depth profile of a tropical ocean thermocline, emphasizing the abrupt temperature shift between 100 and 1000 meters. Additionally, highlight that the temperature remains relatively stable beyond a depth of 1500 meters. Image source: CC BY-SA 3.0, https://commons.wikimedia.org/w/index.php?curid=31055923.

Ocean stratification, including the presence of the thermocline, acts as a barrier to water mixing and affects the vertical exchange of heat, carbon, oxygen, and other constituents. In recent decades (1960-2018), there has been a substantial global increase of approximately 5.3 % in ocean stratification (see [35, 36] for more discussions on increased ocean stratification). This increase hampers the penetration of heat from climate warming into the deep ocean, leading to surface temperature elevation. It also reduces the ocean's capacity to store carbon, which exacerbates global warming. Additionally, ocean stratification inhibits the vertical exchange of nutrients and oxygen, impacting the food supply of marine ecosystems.

When there is a significant stratification of water, it can lead to the creation of internal waves at the boundary between two distinct layers [37]. These internal waves exhibit a much greater vertical displacement, often reaching tens of meters, and move at a slower pace compared to surface waves. One of the earliest instances of observing these internal waves occurred in the Kattegat, a strait located between Denmark and Sweden. In Kattegat, there is a layer of freshwater from the Baltic Sea that sits atop the saltier water from the North Sea. The Swedish oceanographer Otto Petterson designed a buoy with specific characteristics: it had sufficient weight to descend through the upper layer of water but lacked the weight to pass through the deeper layer. As a result, this buoy remained positioned at the boundary between these two layers. Attached to this buoy was a slender pole that extended above the water's surface. As the internal waves propagated along this interface, the tip of the pole was observed to oscillate vertically, reaching heights of up to 5 meters [37].

2.3 Tsunami generated by sub-aquatic volcanic eruptions

Landslides, volcanic eruptions, changes in barometric pressure, and other events can cause non-seismic tsunamis. Compared to tsunamis caused by tectonic earthquakes, they often have a more complex source mechanism. Roughly 6 to 15% of all tsunamis are incepted from non-seismic origins [38]. Volcanic eruptions account for a larger portion of them. See Figure:2.3 for several causes of volcanic eruption induced tsunami. Field observations suggest that explosive eruptions at depths less than approximately 500 m can disturb the free surface enough to give rise to water waves, e.g. Kick'em Jenny in 1939 [39], Myojinsho volcano in 1952 [40, 41, 42], Ritter Island in 1972, 1974 [43, 44, 45], Karymskoye Lake in 1996 [46, 47, 48], Tonga volcanic eruption in 2022 [49, 16, 50, 51]. The erupting volcanic material perforate the water surface and create a crater-like cavity (initial downward displacement) enveloped by a cylindrical bore [52, 53, 54, 55, 53]. This is followed by a formation of a water dome (upward displacement) while the cylindrical bore propagates radially from the source to form a leading wave. The consecutive gravitational collapse of the water dome generates the second bore. The two bores, followed by smaller waves, travel radially from the source [52, 56, 57, 53]. The initial surface displacement and the subsequent cavity collapse have the potential to generate destructive tsunamis [40, 58, 46, 59]. Few of the models developed to study the tsunami caused by sub-aquatic volcanic eruptions are presented in [60, 61, 62, 63].

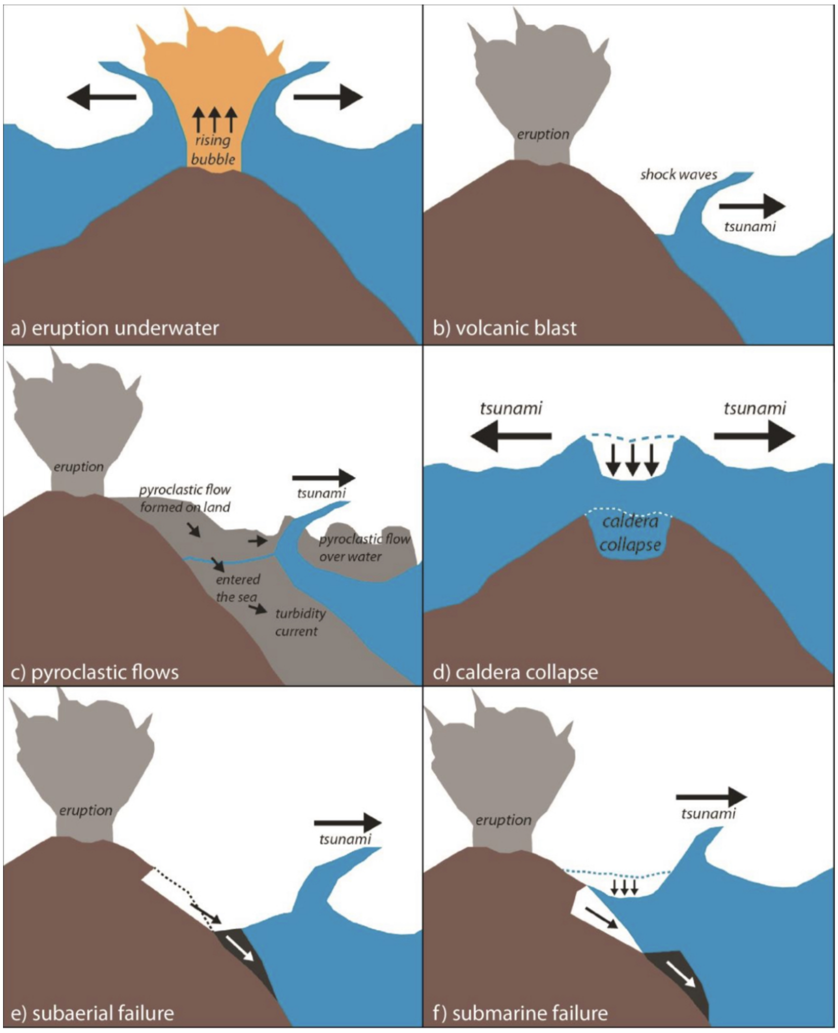

Figure 2.3: Several causes of volcanic eruption induced tsunami: a) underwater explosion; b)blast; c) pyroclastic flows; d) caldera collapse; e) subaerial failure; and f)submarine failure [1]. Image source: Volcanic Eruption-Induced Tsunami in Indonesia: A Review [2] IOP Conf. Ser.:Earth Environ. Sci. Copyright IOP Publishing.

A two-dimensional linear model developed in [61], gives an estimate of the surface waves elevation caused by sub-aquatic volcanic eruptions for a point source suspended in water at some elevation, using potential function approach. This work is an extension of the work presented in [60], to study the sea-surface disturbances generated by underwater volcanic eruptions in compressible and incompressible seas with elastic and stiff bottom.

2.3.1 Tsunami generated by Tonga volcanic eruption

The Hunga Tonga-Hunga Ha'apai (HTHH) submarine volcano, situated in the remote Kingdom of Tonga in the South Pacific, erupted on January 15, 2022, with incredible force. The eruption caused a succession of tsunami waves that were felt both nearby and far away [16]. See Figure:2.5 for travel time plot of tsunami waves generated by Tonga volcanic eruption. The west coast of Tongatapu, 'Eua, and certain islands in the Ha'apai group were all reportedly hit by the waves, which reached heights of up to 15 m, reported by the government of Tonga [16]. The wave heights of 0.2–1.2 m [16] were observed on the tide gauges installed in ports and harbours of capital cities in surrounding South Pacific Island nations, including Fiji, American Samoa, Cook Islands and Vanuatu. For the Hawaiian Islands in the Central Pacific, the highest wave heights were recorded on the northern shores of Kauai (Hanalei: 0.82 m) and Maui (Kahului: 0.83 m) [16]. Japan, more than 7000 km away in the Northwest Pacific, recorded tsunamis along the eastern coasts of the southern and northern islands. Tsunami heights of 1.2 m and 1.1 m were observed in Kagoshima prefecture and Iwate prefecture, respectively [16]. On the other side of the Pacific Rim, more than 10,000 km from the Tonga eruption, on the coasts of Peru and Chile in the Southeastern Pacific, a 2 m tsunami was observed.

Economic damage caused by Tonga volcanic eruption and tsunami generated by it are estimated to be US$90 million which is about 18.5% of Tonga's GDP [64]. Such events impact tourism, agriculture, commerce and infrastructure activities. Nearly 20% of economic damage is caused by the agricultural, forestry and fishing sectors, indicating the risk faced by small island states like Tonga, with an exceptionally high degree of exposure to coastal flooding [64]. The tsunami had a significant impact on neighboring countries in the region. Fiji, specifically the Lau Group, experienced substantial damage to its schools, infrastructure, and fishing vessels. In New Zealand, particularly in the North Island, several marinas faced the loss of floating docks and vessels. Even in more distant places like Chile and Mexico, similar reports of damage were noted [33]. The most extensively documented damage occurred in California and Peru. In California, various harbors experienced damage to both aquatic structures such as floating docks and terrestrial assets like vehicles, facilities, and dredging equipment. The estimated damage in Santa Cruz Harbor alone is approximately 6.5 million [16]. In the latter, the oil tanker Mare Doricum broke its mooring ropes at the La Pampilla oil terminal, causing a polluting oil spill with subsequent environmental problems [65].

The tsunami waves heavily impacted the archipelago southeast of Fiji. The resulting damage included the destruction of coral reefs, causing a significant loss of marine life as many fish either died or migrated elsewhere. The catastrophe exacerbated the challenges faced by Tongans, a majority of whom depended on subsistence reef fishing, as indicated by 2019 World Bank statistics. In response to the disaster, the Tongan government announced its intent to secure $240 million for recovery efforts, particularly focusing on enhancing food security. In the immediate aftermath, the World Bank contributed $8 million towards relief and recovery initiatives [66]. The majority of Tonga's territory is ocean, spanning nearly 700,000 square kilometres, where subsistence fishing plays a crucial role in the nation's diet despite commercial fisheries contributing a mere 2.3% to the economy. The eruption incurred significant losses, estimated at $7.4 million in the fisheries and aquaculture sector, mainly due to damaged fishing vessels—especially impacting the small-scale fisheries—although commercial vessels were also affected. The eruption's precise impact on fish harvests remains challenging to gauge due to the lack of detailed government tracking of subsistence fishing.

Scientists have observed troubling signs indicating a prolonged recovery for fisheries: young corals in the eruption affected coastal waters struggle to mature, once thriving reefs are now barren, likely smothered by volcanic ash, depriving fish of crucial habitats. A government survey noted the absence of marine life near the volcano, while the tsunami disrupted coral formations, leaving fields of coral rubble. The vibrant sounds of a healthy underwater ecosystem vanished, replaced by an unsettling silence, indicating a significant disturbance in Tonga's reefs, as reported in the survey.

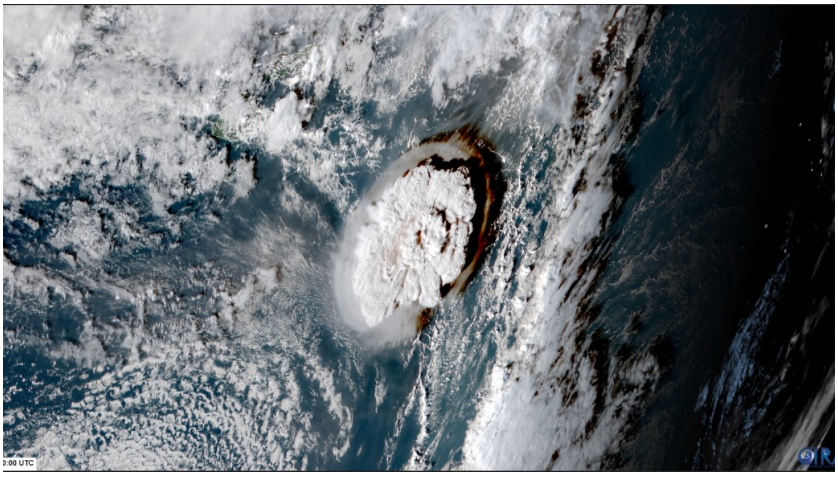

Figure 2.4: A major tsunami event occurred in the Pacific basin on January 15, 2022, at 4:27 GMT due to an undersea volcanic eruption near the Tonga Islands. The National Oceanic and Atmospheric Administration's Center for Operational Oceanographic Products and Services (CO-OPS) detected the initial tsunami wave at their monitoring station in Pago Pago, American Samoa, less than an hour after the eruption. The tsunami wave had an estimated height of around 1.8 feet. The figure shows the satellite image of the volcanic eruption in the Tonga-Hunga Ha'apai region [3]. Image credit: CSU/CIRA and JAXA/JMA

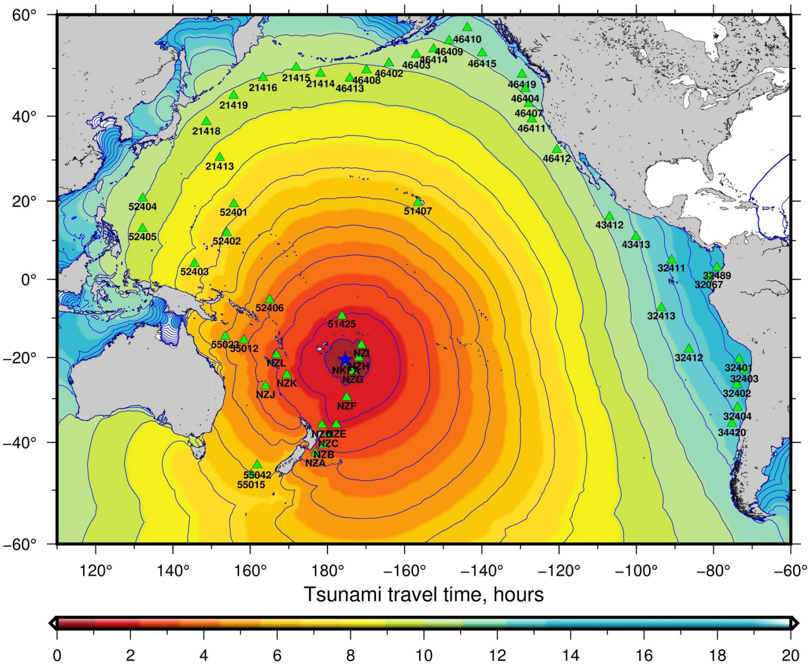

Figure 2.5: Travel time plot for the Tsunami generated by Tonga volcanic eruption on January 15, 2022. DART stations (green triangles) and theoretical tsunami (long wave) travel time (TTT) map. The contour intervals for the TTT is 1 hour. Blue star represents the location of Hunga Tonga -Hunga Ha'apai volcano. Image source: Hunga Tonga-Hunga Ha'apai volcano-induced sea level oscillations and tsunami simulations, GNS Sci (2022) [4]. Copyright 2022 GNS Sci.

2.4 Subaqueous flows induced by underwater volcanic eruptions

Subaqueous flows generated by submarine volcanic eruptions represent a complex and understudied phenomenon. The extreme underwater conditions and limited accessibility make it challenging to observe and analyze these events in real-time. The creation of density currents during submarine volcanic eruptions adds another layer of complexity to our limited understanding of these phenomena. The interplay between the buoyant plumes of volcanic gases and the denser mixtures of volcanic material and seawater results in the formation of these currents. The recent volcanic eruption in Tonga provided a unique and valuable opportunity for researchers to gain insights into subaqueous flows induced by underwater volcanic events. This extraordinary event, which was extensively documented through satellite imagery and ocean sensors, allowed scientists to closely examine the formation and dynamics of density currents in real time. One of the key observations made during the study of subaqueous flows induced by the Tonga volcano eruption was the analysis of seabed topography and the presence of tephra deposits in the vicinity. Researchers closely examined the seafloor landscape to understand how its features influenced the direction and propagation of density currents.

The ejected debris from the Tonga volcano, including rocks and ash, swiftly collapsed into the ocean, forming exceptionally rapid volcaniclastic submarine density currents [67]. These currents, the fastest ever recorded, moved along the submerged volcano slopes and proceeded to travel across the seafloor, causing damage to nearly 200 kilometers of underwater cables, with one cable shifting more than 5 kilometers due to the force. These findings underscore the vulnerability of our global communication systems to the impact of underwater volcanic activity, particularly considering that approximately 95% of worldwide communications rely on these seafloor cables [68]. Moreover, the disruption caused by such events highlights the pressing need for improved monitoring and contingency plans to safeguard against future disturbances. In addition to the physical damage inflicted on the cables, the volcanic activity may also have long-term environmental consequences, affecting marine ecosystems and contributing to changes in oceanic conditions. As such, a comprehensive understanding of the interaction between underwater volcanic events and communication infrastructure is crucial for mitigating potential risks and ensuring the resilience of our interconnected world. Furthermore, the rapid response and coordination among international agencies following such incidents underscore the importance of collaborative efforts in addressing emerging threats to global telecommunications infrastructure.

In their study [67], Clare et al. reported that these density currents underwent a shift between two different flow behaviors, or rheologies. The appearance of the deposits left behind by these currents, as well as their deposition on steep slopes of the volcano, indicates that they likely started as dense, granular flows laden with particles and propelled by gas, resembling pyroclastic density currents found on land. Subsequently, the characteristics of the deposits suggest that these currents then transformed into water-borne, particle-laden submarine density currents, commonly referred to as turbidity currents. This transition between rheological behaviors not only underscores the complex dynamics of underwater volcanic events but also highlights the need for refined models to accurately predict the behavior and impact of such phenomena on submarine infrastructure. Moreover, understanding the mechanisms driving these transitions is crucial for assessing the potential hazards posed by volcanic activity in submarine environments and devising effective risk management strategies. By elucidating the underlying processes governing the evolution of density currents, researchers can better anticipate and mitigate the impacts of future volcanic eruptions on underwater communication networks and other critical infrastructure.

2.5 Convection driven by heating at bottom boundary

The phenomenon characterized by a horizontal temperature or heat flux difference along a single boundary in a fluid is now recognized as 'horizontal convection.' This type of convection sets itself apart from the more familiar Rayleigh–Bénard and Grashof forms, which involve heat transfer between either two horizontal or two vertical boundaries. In horizontal convection, the transport of heat flux doesn't necessarily traverse the entire depth of the fluid. Traditionally, it was believed that only a gradual, diffusively-driven circulation could develop in proximity to the heat source and sink [69, 70]. However, laboratory experiments and numerical investigations introducing a horizontal temperature gradient have shown a circulation that extends throughout the depth of the container [71, 72, 73].

It has been reported in [73], two convection cells arranged vertically were observed. These cells circulated in the same rotational sense and extended the entire length of the tank. The lower cell exhibited a robust circulation, while the upper cell showed comparatively weaker movement, likely influenced by a minor horizontal temperature gradient generated by heat transfer between the two cells. Additionally, it was observed that in every instance, the flow in the two-cell mode underwent a gradual transformation. The ascending plume slowly extended higher until, barring the smallest heat fluxes, it ultimately reached the uppermost part of the container. This evolution was primarily regulated by the upward diffusion of heat through the depth of the upper cell, or at the very least, through a region characterized by a substantial temperature gradient.

Through the majority of its vertical extent, the plume displayed turbulent characteristics due to a pronounced mean shear existing between the ascending water and the comparatively stationary interior [73, 71]. It is also pointed out that the flow exhibited an extreme asymmetry between the size of the sinking and rising legs of the convective overturning as all heat enters and leaves through the bottom. It is in effect added by convection and eliminated by conduction. Thus, the asymmetry is maintained by the relative efficiencies of heat transfer [71, 72].

2.6 Subglacial volcanism under the West Antarctic Ice Sheet (WAIS)

The West Antarctic ice sheet (WAIS) faces a significant risk of collapse due to rising ocean and surface temperatures. Recent findings [5, 74, 75, 76] based on ice core tephra reveal that subglacial volcanism has the potential to breach the ice sheet's surface, posing a considerable threat to WAIS stability. Through micro-CT analyses on englacial ice core tephra, as well as in-depth shard morphology characterization and geochemical analysis, it has been indicated that two tephra layers originated from subglacial to emergent volcanism that penetrated the WAIS. These tephra deposits occurred at the center of the ice sheet, near WAIS Divide, and were preserved in the WDC06A ice core. The likely sources of these tephra layers are believed to be nearby subglacial volcanoes, such as Mt. Resnik, Mt. Thiel, and/or Mt. Casertz.

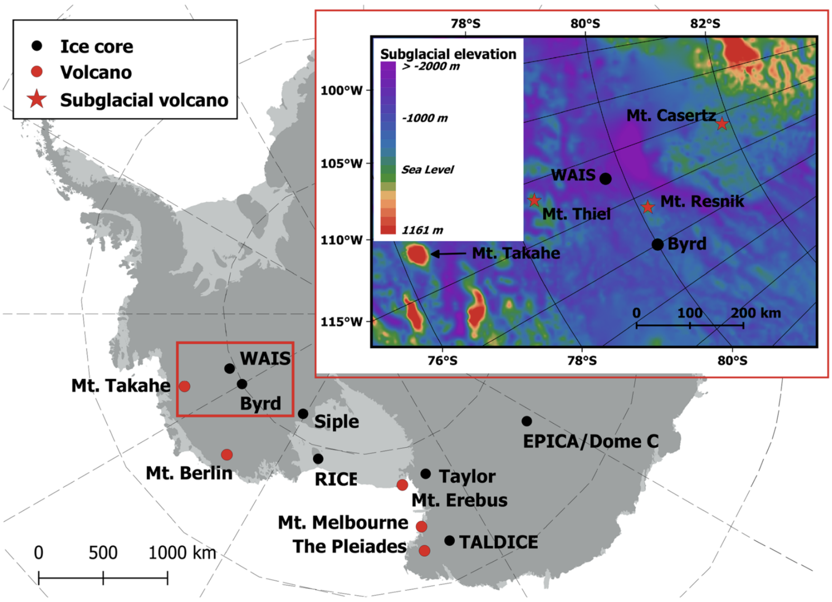

Figure 2.6: A depiction of Antarctica featuring the locations of ice cores and active volcanoes is presented. Additionally, an inset displays a topographical map of the subglacial bedrock beneath the West Antarctic Ice Sheet (WAIS), highlighting the positions of identified or inferred subglacial volcanoes. Image source:[5]. Copyright Nature Scientific reports.

Evidence extracted from tephra layers within the WDC06A ice core indicates that over the past 45,000 years, two subglacial eruptions breached the West Antarctic Ice Sheet (WAIS). At approximately 44.5 thousand years ago, a basanitic eruption occurred, depositing over 1 cm of tephra on the adjacent ice sheet. Subsequently, at 22.3 thousand years ago, a second eruption, characterized as trachyandesite to trachydacite, left a 2 cm thick layer of tephra, containing shards exceeding 200 μm in diameter. Micro-CT analysis conducted on these tephra layers revealed a complex eruption history, marked by a combination of magmatic and phreatomagmatic phases interspersed within predominantly phreatomagmatic eruptions. This marks the inaugural application of μCT to in situ ice core tephra, enabling the observation of spatial distribution of tephra particles on an unprecedented scale.

The ongoing loss of ice from the WAIS is projected to reduce the ice sheet's elevation, potentially triggering a positive feedback loop by elevating volcanism in West Antarctica. While there is currently no substantiated evidence linking heightened volcanism to the Quaternary collapse of the WAIS, an escalation in volcanic activity could generate increased basal meltwater, fostering enhanced ice flow and subsequent ice loss, thereby perpetuating a positive feedback loop. The delicate equilibrium between deglaciation and volcanism may exert a profound influence on the stability of the WAIS and, consequently, the ensuing rise in sea levels.

2.7 Equatorial oceanic flows

The seawater in the vicinity of the Pacific equator has several unique features. There is the surface current, which flows west in the proximity of the equator, and a greater current underneath it, which travels east the Equatorial Undercurrent (EUC) reported by Cromwell and his colleagues in 1954. The flow field under the EUC decays swiftly to a nearly quiescent abyssal layer [77, 78]. Equatorial ocean regions also present a pronounced stratification, greater than anywhere else in the ocean [79].

The equatorial flow dynamics can be summed up broadly in the following three properties

1. A shallow westward surface current flow (typically within the top 50m depth). This is primarily limited to a few degrees on either side of the equator.

2. A powerful eastward undercurrent running at a significantly quicker rate than the surface stream. This is largely in charge of vertically integrated transport. A somewhat faint flow exists under this undercurrent.

3. Flow westward on both sides of the EUC, with eastward countercurrents poleward of this. The Northern hemisphere has the strongest current, which touches the surface.

Constantin and Johnson have recently proposed a class of three-dimensional non-linear models based on the classical fluid-dynamics approach to study the equatorial oceanic flows [80, 20, 81, 82]. The mathematical model presented in [20] is mathematically consistent, capturing the essential properties of the flow observed in the Pacific equatorial undercurrent (EUC), and avoids any oversimplification. The model, for example, provides for the Coriolis effects caused by the Earth's rotation and preserves non-traditional terms introduced in the formulation. The model effectively gives asymptotic solutions based on the assumption of slow evolution of a two-layer flow in the equatorial direction. Some numerical simulations of this model to investigate the properties of velocity field and flow paths have been carried out in [83, 21].

2.8 Critical Evaluation of Existing Literature

The models discussed [72, 73, 84] are relatively basic and do not provide a comprehensive three-dimensional analysis of the flows resulting from the introduction of heat flux at the bottom boundary. The research presented in [71, 72, 73] also overlooks the stratification in the fluid, and the experiments [73, 71] lack sufficient measurement of horizontal flows induced by the introduction of heat flux at the bottom. While the experimental results [84] consider fluid stratification based on salinity, the primary focus is on studying vertical buoyant flows, neglecting the analysis of horizontal velocities. One aim of this thesis is to provide a full 3-dimensional analysis of the flows generated by the introduction of heat flux at the bottom in a stratified medium and see how the flow structures are affected when the medium is stratified with respect to (a) temperature and (b) salinity.

The model outlined in [61] for estimating surface wave elevation due to submarine volcanic eruptions does not incorporate ambient stratification. Despite this limitation, it extends the previous work [60] to analyze sea-surface disturbances resulting from underwater volcanic events across various sea conditions, such as compressible and incompressible seas with elastic and stiff bottom characteristics. Integrating ambient stratification into the model could provide further insights into the dynamics of such phenomena and enhance its applicability to a wider range of scenarios. One of the objective of this study is to formulate a two-dimensional model aimed at examining the gravitational wave dynamics prompted by submarine volcanic eruptions within stratified ocean environments.

Traditional models for tsunami generation focus on the displacement potential function [61, 60], which captures initial surface displacement resulting from seismic or non-seismic events like landslides and geological shifts. This approach typically accounts for seabed displacement and mass flux but often does not fully incorporate the complex dynamics introduced by submarine volcanic eruptions. Unlike other events, submarine eruptions add not only mass but also significant heat to the water column. This heat flux triggers convection currents, where buoyant forces lift high-temperature, low-density water toward the surface, generating vertical flows that, in shallow environments, can penetrate the water surface and create surface waves, as has been pointed in [61, 60]. The inclusion of heat flux effects introduces complexities like plume formation and water entrainment, which substantially influence vertical velocities and, consequently, surface wave characteristics. To better understand these effects, a three-dimensional ocean flow model [18, 19] will be applied to simulate high heat flux scenarios in shallow water settings. By implementing a Gaussian heat flux profile with varied intensity (e.g., 10,000 and 20,000 W/m^2), differences in resulting surface waves will be observed, particularly in relation to volcano depth below the water surface.

The equatorial undercurrent plays a crucial role in ocean dynamics, exerting significant control over factors like temperature, salinity, and nutrient levels in the equatorial thermocline. It also affects biological productivity, carbon exchange with the atmosphere, and phenomena like the El Niño Southern Oscillation. Since Cromwell's discovery of these undercurrents in the 1950s, numerous studies have investigated their behavior [85]. In recent years, several models have been developed to simulate nonlinear equatorial ocean flows by researchers such as Constantin and Johnson (for further discussions, see [86]), with some numerical simulations also presented [87, 88]. However, there are currently no models that account for the influence of submarine volcanic eruptions on ocean flows near the equator in addition to the effects of the equatorial undercurrents. As a result, our aim is to enhance a three-dimensional nonlinear model based on the framework introduced in [20], incorporating the impact of submarine volcanic eruptions. We will then seek to derive the precise solution for the flow velocities under these conditions and contrast it with the scenario where volcanic activity is absent, as described in [20]. Fig. 2.1 shows some of the submarine volcanoes which are part of Ring of Fire lie in equatorial region in Pacific and Indian ocean.

Chapter 3

Modeling of submarine volcanic eruptions

To model the submarine volcanic eruptions we will first start with the equations governing the hydrodynamical flow of a viscous fluid of varying density and temperature. In this Chapter we will obtain these basic equations along with other equations governing the submarine volcanic eruptions we will also provide different ways to include submarine volcanic eruptions in a model and some general challenges that are faced during the modeling of submarine volcanic eruptions.

Consider then a fluid in which the density ρ is the function of position $x_j(j = 1, 2, 3)$. Let u_j denote the components of the velocity.

3.1 Equation of continuity

As the rate of change of mass contained in a fixed volume V of fluid is given by the rate at which the fluid flows out of it across the boundary S. We can write this in mathematical notation as

$$\frac{\partial}{\partial t} \int_V \rho \, d\tau = - \int_S \rho u_j \, dS_j, \tag{3.1}$$

where $d\tau (= dx_1, dx_2, dx_3)$ is the element of volume, S is the bounding surface of the volume V and dS_j represents a vector normal to the element of the surface dS. By Gauss's theorem the surface integral on the right hand side of equation (3.1) can be written in terms of volume integral and hence we have

$$\frac{\partial}{\partial t}\int_V \rho \, d\tau = -\int_V \frac{\partial}{\partial x_j}(\rho u_j) \, d\tau. \tag{3.2}$$

Since (3.2) is true for an arbitrary volume V we will have

$$\frac{\partial \rho}{\partial t} + \frac{\partial}{\partial x_j}(\rho u_j) = 0, \tag{3.3}$$

above equation is known as the conservation of mass. For an incompressible fluid the equation (3.3) reduces to

$$\frac{\partial u_j}{\partial x_j} = 0. \tag{3.4}$$

3.2 Equations of motion

We will first give an expression for the stress P_{ij} acting in the direction of x_j per unit area on a element of surface normal to x_i. The stress must be related to the rate of increase of strain e_{ij} in the fluid. The expression for strain is given as

$$e_{ij} = \frac{1}{2}\left(\frac{\partial u_i}{\partial x_j} + \frac{\partial u_j}{\partial x_i}\right). \tag{3.5}$$

Since the stress and strain are related linearly we can write

$$P_{ij} = \omega_{ij} + q_{ij;kl} e_{kl}, \tag{3.6}$$

where ω_{ij} is a symmetric tensor and P_{ij} tends to ω_{ij} when $e_{kl} = 0$ and $q_{ij;kl}$ is a tensor of fourth rank. For an isotropic fluid, the forms of equation (3.6) are irrelevant to arbitrary rotations and translations of the coordinate system. Thus ω_{ij} and $q_{ij;kl}$ are isotropic tensors (an isotropic tensor is a tensor that exhibits isotropy, which means it behaves the same way in all directions) and have the form

$$\omega_{ij} = -p\delta_{ij} \tag{3.7}$$

and

$$q_{ij;kl} = \lambda\delta_{ij}\delta_{kl} + \mu(\delta_{ik}\delta_{jl} + \delta_{il}\delta_{jk}), \tag{3.8}$$

where p, λ and μ are arbitrary scalar functions of x_i and δ is Kronecker delta. Note, for a second-order tensor (e.g., a stress or strain tensor), isotropy implies that the tensor's components are the same in all coordinate directions and for a fourth order tensor, it is characterized by a combination of constants that ensure isotropy in all directions. Substituting the equations (3.7) and (3.8) in equation (3.6) we have

$$P_{ij} = -p\delta_{ij} + \lambda\delta_{ij}e_{kk} + 2\mu e_{ij}. \tag{3.9}$$

When there is no strain, we define p as an isotropic pressure at x_i. Hence we have

$$P_{ii} = -3p = -3p + 2\mu e_{ii} + 3\lambda e_{kk}, \tag{3.10}$$

which will give

$$\lambda = -\frac{2}{3}\mu, \tag{3.11}$$

therefore, P_{ij} now takes the form

$$P_{ij} = -p\delta_{ij} + 2\mu e_{ij} - \frac{2}{3}\mu\delta_{ij}e_{kk}, \tag{3.12}$$

the coefficient μ is known as the coefficient of viscosity. Terms proportional to μ in equation (3.12) define the stress due to viscosity p_{ij} which is given as

$$p_{ij} = \mu\left(\frac{\partial u_i}{\partial x_j} + \frac{\partial u_j}{\partial x_i}\right) - \frac{2}{3}\mu\frac{\partial u_k}{\partial x_k}\delta_{ij}. \tag{3.13}$$

If the fluid is incompressible using equation (3.4) viscous tensor takes the form

$$p_{ij} = \mu\left(\frac{\partial u_i}{\partial x_j} + \frac{\partial u_j}{\partial x_i}\right). \tag{3.14}$$

In terms of the stress P_{ij} we can write the hydrodynamical equation of motion as

$$\rho\frac{\partial u_i}{\partial t} + \rho u_j\frac{\partial u_i}{\partial x_j} = \rho X_i + \frac{\partial P_{ij}}{\partial x_j}, \tag{3.15}$$

where X_i is the ith component of whatever external force maybe acting on the fluid. Substituting the value of P_{ij} in the above equation, we have

$$\rho\frac{\partial u_i}{\partial t} + \rho u_j\frac{\partial u_i}{\partial x_j} = \rho X_i - \frac{\partial p}{\partial x_i} + \frac{\partial}{\partial x_j}\left(\mu\left(\frac{\partial u_i}{\partial x_j} + \frac{\partial u_j}{\partial x_i}\right) - \frac{2}{3}\mu\frac{\partial u_k}{\partial x_k}\right). \tag{3.16}$$

For an incompressible fluid with constant μ, above equation takes the form

$$\rho\frac{\partial u_i}{\partial t} + \rho u_j\frac{\partial u_i}{\partial x_j} = \rho X_i - \frac{\partial p}{\partial x_i} + \mu\nabla^2 u_i. \tag{3.17}$$

It can be shown that equation (3.15) represent the conservation of momentum. Integrating equation (3.15) over an arbitrary volume V we have

$$\int_V \rho\frac{\partial u_i}{\partial t}\, d\tau + \int_V \rho u_j\frac{\partial u_i}{\partial x_j}\, d\tau = \int_V \rho X_i\, d\tau + \int_V \frac{\partial P_{ij}}{\partial x_j}\, d\tau, \tag{3.18}$$

Using Gauss's theorem, integral by parts and equation of continuity the above equation can be written as

$$\frac{\partial}{\partial t}\int_V \rho u_i\, d\tau = \int_V \rho X_i\, d\tau + \int_S P_{ij}\, dS_j - \int_S \rho u_i u_j\, dS_j. \tag{3.19}$$

Equation (3.19) expresses the conservation of momentum. It says, the rate of change of the momentum contained in a fixed volume V of the fluid is equal to the volume integral of external forces acting on the fluid elements plus the surface integral of the normal stress acting on the surface S bounding the volume V minus the rate at which the momentum flows out of V across the bounding surface S.

3.2.1 Equations of motion in rotating frame of reference

Consider a fluid in rotation about some fixed axis with a constant angular velocity Ω. We will describe the motion as they appear to an observer at rest in a frame rotating about the same axis with same angular velocity. It should be noted that, the velocities and acceleration observed by the observer at rest in the rotating frame of reference will not be the same as the velocities and acceleration observed by an observer at rest with respect to fixed inertial frame. Consider the inertial frame (ξ, η, ζ) with respect to which the chosen coordinate system (x, y, z) is rotating with the angular velocity Ω about the ζ-axis. It is also considered that the axis ζ and z coincide. The transformation relating the two coordinate system is given as follows

$$x = \xi cos\Omega t + \eta sin\Omega t,\ y = -\xi sin\Omega t + \eta cos\Omega t,\ z = \zeta. \tag{3.20}$$

The components along the instantaneous directions of the axis of the rotating frame of a vector q (with components q_ξ, q_η, q_ζ) in inertial frame, will be given as

$$q_x^* = q_\xi cos\Omega t + q_\eta sin\Omega t,\ q_y^* = -q_\xi sin\Omega t + q_\eta cos\Omega t,\ q_z^* = q_\zeta. \tag{3.21}$$

Note that, $(*)$ is used to distinguish the components of vector obtained by this transformation with the one that will be observed by the observer at rest in the rotating frame, as having the physical meaning of q.

Differentiating (3.20) with respect to t we have

$$\frac{dx}{dt} = \left(\frac{d\xi}{dt} cos\Omega t + \frac{d\eta}{dt} sin\Omega t\right) + \Omega(-\xi sin\Omega t + \eta cos\Omega t), \tag{3.22}$$

$$\frac{dy}{dt} = \left(-\frac{d\xi}{dt} sin\Omega t + \frac{d\eta}{dt} cos\Omega t\right) - \Omega(\xi cos\Omega t + \eta sin\Omega t). \tag{3.23}$$

The quantities $\frac{dx}{dt}$ and $\frac{dy}{dt}$ will be recognized by the observer at rest in the rotating frame of reference as component u_x and u_y of the velocities of fluid element along x and y directions. The quantities in the first brackets on the right hand side of equation (3.22) and (3.23) are components along the instantaneous directions of x and y of what is the velocity in inertial frame, denoted by u_x^* and u_y^*. Equations (3.22) and (3.23) can now be written as

$$u_x = u_x^* + \Omega y,\ u_y = u_y^* + \Omega x,\ u_z = u_z^*. \tag{3.24}$$

Equations above can be combined to give single vector equation

$$\mathbf{u} = \mathbf{u}^* - \mathbf{\Omega} \times \mathbf{r}. \tag{3.25}$$

Differentiating equations (3.22) and (3.23) with respect to t and substituting the values of u_x^* and u_y^* from equation (3.24) we will have

$$\left(\frac{d\mathbf{u}^*}{dt}\right)^* = \frac{d\mathbf{u}}{dt} + 2\mathbf{\Omega} \times \mathbf{u} - \frac{1}{2} grad(|\mathbf{\Omega} \times \mathbf{r}|). \tag{3.26}$$

In the above expression term $2\mathbf{\Omega}\times\mathbf{u}$ represents the Coriolis acceleration and $\frac{1}{2}grad(|\mathbf{\Omega}\times\mathbf{r}|)$ represents the centrifugal force.

The equation of motion (3.16) will take the following form in the rotating frame of reference

$$\frac{\partial u_i}{\partial t} + u_j \frac{\partial u_i}{\partial x_j} = X_i + \frac{1}{\rho}\frac{\partial P_{ij}}{\partial x_j} + \frac{\partial}{\partial x_j}(\frac{1}{2}|\mathbf{\Omega} \times \mathbf{r}|^2) + 2\epsilon_{ijk} u_j \Omega_k. \tag{3.27}$$

where ϵ_{ijk} is Levi-Civita symbol given by

$$\epsilon_{ijk} = \begin{cases} 0, & \text{if } i = j \text{ or } j = k \text{ or } k = i \\ 1, & \text{if } (i, j, k) \text{ is } (1, 2, 3), (2, 3, 1) \text{ or } (3, 1, 2) \\ -1, & \text{if } (i, j, k) \text{ is } (3, 2, 1), (1, 3, 2) \text{ or } (2, 1, 3). \end{cases} \tag{3.28}$$

3.3 Viscous dissipation

Viscous dissipation refers to the conversion of mechanical energy into heat due to the internal friction or viscosity within a fluid. It occurs when a fluid flows and experiences shear stress, leading to the generation of heat as a result of the viscous forces acting within the fluid. We will now obtain an expression for the rate of viscous dissipation. Multiplying equation of motion (3.15) by u_i and integrating over the volume V we will have

$$\frac{1}{2}\int_V \rho \frac{\partial}{\partial t} u_i^2 \, d\tau + \frac{1}{2}\int_V \rho u_j \frac{\partial}{\partial t} u_i^2 \, d\tau = \int_V \rho u_i X_i \, d\tau + \int_V u_i \frac{\partial P_{ij}}{\partial x_j} \, d\tau. \tag{3.29}$$

Using integration by parts, Gauss's theorem and equation of continuity the above integral can be simplified to give an expression for the rate at which kinetic energy contained in a volume V of a fluid changes

$$\frac{1}{2}\frac{\partial}{\partial t}\int_V \rho u_i^2\, d\tau = \int_V \rho u_i X_i\, d\tau + \int_S u_i P_{ij}\, dS_j - \frac{1}{2}\int_S \rho u_i^2 u_j\, dS_j - \int_V P_{ij}\frac{\partial u_i}{\partial x_j}\, d\tau. \quad (3.30)$$

In the above equation, the first term on right hand side represent the rate at which the external forces do work on the element of the fluid in volume V, the second term represents the rate at which the stress P_{ij} works on the boundary S bounding the volume V, the third term represents the rate at which energy flows out of the volume V across S, finally, to explain the last term we need to expand the integrand first. Using the definition of e_{ij} equation (3.5) and P_{ij} equation (3.12) we have

$$P_{ij}\frac{\partial u_i}{\partial x_j} = P_{ij}e_{ij} = (-p\delta_{ij} + 2\mu e_{ij} - \frac{2}{3}\mu\delta ij e_{kk})e_{ij} = -pe_{jj} + 2\mu e_{ij}^2 - \frac{2}{3}\mu(e_{jj})^2. \quad (3.31)$$

The first term on the right hand side of above equation is

$$-pe_{jj} = -p\frac{\partial u_j}{\partial x_j} = \frac{p}{\rho}\left(\frac{\partial \rho}{\partial t} + u_j\frac{\partial \rho}{\partial x_j}\right), \quad (3.32)$$

note that the term on the right hand side of above equation is obtained using the equation of continuity . The volume integral of the quantity on the right hand side of above equation represents the increase in the internal energy due to compression which the fluid experiences. The remaining term

$$\Phi = 2\mu e_{ij}^2 - \frac{2}{3}\mu(e_{jj})^2 \quad (3.33)$$

therefore, represents the rate at which energy dissipated, irreversibly, by viscosity in each element of volume of the fluid.

We have seen that the law of conservation of mass and conservation of momentum leads to the equation of continuity (3.3) and equation of motion (3.16), respectively. Next, we will express the law of conservation of energy and see it will lead to the equation of heat transport which will be used to model the heat flux introduced by volcanic eruption in our study.

3.4 The equation of heat transport

The energy E per unit mass of the fluid can be written as

$$E = \frac{1}{2}u_i^2 + c_V T, \tag{3.34}$$

where c_V is the specific heat at constant volume (V) and T is the temperature. Considering the gain and loss of energy which occur in a volume V of the fluid, per unit time, we have

$$\begin{aligned}\frac{\partial}{\partial t}\int_V \rho E\, d\tau = {} & \text{rate at which the work is done on the boundary } S \text{ of } V \\ & \text{by the stress } P_{ij} + \\ & \text{rate at which work is done on each element of the fluid inside} \\ & V \text{ by external forces} - \\ & \text{rate at which energy is conducted in the form of heat across } S - \\ & \text{rate at which energy is convected across } S \text{ by the prevailing mass motion} \\ = {} & \int_S u_i P_{ij}\, dS_j + \int_V \rho u_i X_i\, d\tau + \int_S k\frac{\partial T}{\partial x_j}\, dS_j - \int_S \rho E u_j\, dS_j, \end{aligned} \tag{3.35}$$

where k is the coefficient of heat diffusion. Using equations (3.30), (3.31) and (3.32) we can write first term on the right hand side of equation (3.35) as

$$\begin{aligned}\int_S u_i P_{ij}\, dS_j = {} & \frac{1}{2}\frac{\partial}{\partial t}\int_V \rho u_i^2\, d\tau + \frac{1}{2}\int_S \rho u_i^2 u_j\, dS_j - \int_V \rho u_i X_i\, d\tau - \\ & \int_V p\frac{\partial u_j}{\partial x_j} + \int_V \Phi\, d\tau, \end{aligned} \tag{3.36}$$

also, an alternative forms for the third and the fourth terms in equation (3.35) are

$$\int_S k\frac{\partial T}{\partial x_j}\, dS_j = \int_V \frac{\partial}{\partial x_j}\left(k\frac{\partial T}{\partial x_j}\right) d\tau, \tag{3.37}$$

and

$$
\begin{aligned}
-\int_S \rho E u_j\, dS_j &= -\int_S \rho(\frac{1}{2}u_i^2 + c_V T)u_j\, dS_j \\
&= -\frac{1}{2}\int_S \rho u_i^2 u_j\, dS_j - \int_V \frac{\partial}{\partial x_j}(\rho u_j c_V T)\, d\tau. \quad (3.38)
\end{aligned}
$$

Substituting equations (3.36), (3.37) and (3.38) in equation (3.35) we have

$$
\begin{aligned}
\int_V \frac{\partial}{\partial t}(\rho c_V T)\, d\tau = \int_V \frac{\partial}{\partial x_j}\left(k\frac{\partial T}{\partial x_j}\right) d\tau - \int_V p\frac{\partial u_j}{\partial x_j}\, d\tau + \int_V \Phi\, d\tau - \\
\int_V \frac{\partial}{\partial x_j}(\rho u_j c_V T)\, d\tau. \quad (3.39)
\end{aligned}
$$

Equation (3.39) holds for arbitrary volume V and using equation of continuity we will have

$$
\rho\frac{\partial}{\partial t}(c_V T) + \rho u_j \frac{\partial}{\partial x_j}(c_V T) = \frac{\partial}{\partial x_j}\left(k\frac{\partial T}{\partial x_j}\right) - p\frac{\partial u_j}{\partial x_j} + \Phi. \quad (3.40)
$$

The equations (3.3), (3.12), (3.15), (3.33) and (3.40) are the basic hydrodynamic equations usually accompanied by the equation of state.

3.5 Incorporating volcanic eruptions into the model

Adding heat flux: One of the most apparent methods to integrate volcanic eruptions into a model is to incorporate the fluctuation of heat at the seabed or within the crater. The derived heat transport equation (3.40) can be used in this regard. In the model, this equation can be used to incorporate the heat flux generated by volcanic eruptions. This heat flux contributes to the formation of a buoyant vertical plume, as reported in [71, 72].

Adding vertical velocity flux at seabed: An alternative approach involves incorporating the vertical flow velocity at the seabed by modifying the bottom boundary condition. This adjustment is motivated by the understanding that seawater infiltrates the seafloor through cracks, undergoing heating by magma. This thermal process triggers chemical reactions, leading to the conversion of seawater into hydrothermal fluid. The resultant heated fluid is then expelled into the ocean, as detailed in [89].

It's important to highlight that incorporating both the heat flux and vertical flow at the seabed can collectively contribute to warming the incoming water, reducing its density. This interplay creates a density deficiency, leading to gravitational convection, as elaborated in [84].

Integrating temperature-driven density variations in upward plume movement: Another approach to account for the impact of a volcanic eruption involves adjusting the density in tandem with the temperature fluctuations induced by the buoyant plume. This entails acknowledging that the plume's temperature diminishes as it ascends through the ocean layers from the volcanic crater. This particular assumption was incorporated in a recent study [90]. Nonetheless, the aforementioned condition already takes into account the entrainment of water and the influence of buoyancy by adjusting the density function accordingly. This specificity is particularly tailored to the examination of density currents or submarine flows induced by volcanic eruptions.

Displacement potential source function: Modeling a sudden and significant eruption involves incorporating the instantaneous addition of mass flux to the system. This approach was initially pioneered by Unoki and Nakano in 1953 [63]. Subsequently, Duffy in 1992 adopted this methodology in [60] for investigating the surface waves produced by underwater volcanic eruptions. The function employed to model this phenomenon is referred to as the instantaneous Duffy source function or displacement potential source function. The Duffy source function models the initial sea surface displacement caused by an underwater volcanic eruption or a similar event. This displacement serves as the starting point for simulating the resulting tsunami waves. The Duffy displacement potential source function for the vent size of radius r_0 is represented as follows

$$S = [\theta(r) - \theta(r - r_0)]\theta(t) \tag{3.41}$$

where $\theta(\cdot)$ is the Heaviside step function.

3.6 Challenges of modeling volcanic eruptions in fluid dynamics

Modeling volcanic eruptions within oceanic fluid dynamics is particularly challenging due to the extreme and complex conditions of these events. Volcanic eruptions introduce intense heat, gases, high temperature, and particulates into the surrounding water, triggering rapid and dynamic processes that are difficult to capture using standard fluid dynamics models. Traditional numerical oceanographic models are designed to simulate gradual changes over broader spatial and temporal scales, making them less effective for handling the abrupt, localized effects of eruptions. Simulating these events requires fine spatial and temporal resolution to account for sudden shifts in temperature, density, salinity and chemical composition near the eruption site.

One of the primary obstacles is the harsh environment of underwater eruptions. At great depths, the high pressure around the seafloor alters the behavior of superheated fluids and gases. For example, water near an eruption site can be heated far beyond its typical boiling point without vaporizing due to the extreme pressure. This necessitates the use of specialized equations of state that incorporate deep-sea pressure and temperature and density dynamics. Additionally, interactions between the hot volcanic material and the colder surrounding seawater can trigger rapid cooling, condensation, hydrodynamic instabilities and sometimes explosive reactions, further complicating the modeling of heat and mass transfer.

Turbulence and mixing from eruptions add another layer of complexity. Hot, less dense fluids from eruptions create buoyant plumes that rise rapidly through denser, colder water, generating turbulent zones that are challenging to model. Such turbulent behavior introduces numerical instability, which are difficult to handle in large simulations with the current numerical framework. The turbulent mixing also involves intricate interactions between buoyancy, momentum, and shear forces, which require high-resolution modeling to represent accurately. However, such detailed modeling demands significant computational resources, making it impractical for long-term simulations. Ocean models typically use simplified approaches to approximate turbulence, but these approximations often fall short when applied to the intense, localized turbulence generated by volcanic eruptions.

Eruptions also release dissolved gases, vapors and particles that alter the physical and chemical properties of surrounding water, creating additional modeling challenges. Gases such as sulfur dioxide and carbon dioxide, along with ash, metals oxides and mineral particles, change water density, pH, and viscosity. The presence of solids and gases requires treating the fluid as a multiphase flow, a process that is computationally complex and involves modeling the interactions between the different phases. Simplifying these elements into bulk properties is a common workaround, but this often reduces the accuracy of models in capturing the full effects of eruptions on the ocean environment.

Another major challenge is the scarcity of observational data, as most eruptions occur in deep, remote areas. Limited access to direct measurements of temperature, pressure, and flow velocity around eruption sites due to high temperature, pressure and other extreme conditions makes data collection difficult and costly, often relying on indirect methods or specialized equipment like remotely operated vehicles (ROVs). The lack of observational data complicates model validation and limits the reliability of simulations. Furthermore, the unique characteristics of each eruption—such as variations in magma composition, intensity, and duration—mean that data from one eruption may not be applicable to others, requiring generalized assumptions that can reduce the models' specificity.

Finally, computational limitations pose a significant barrier to detailed eruption modeling. High-resolution models that can capture fine-scale dynamics and turbulence require substantial memory and processing power. Three-dimensional simulations add another layer of complexity, making it difficult to achieve both accuracy and computational efficiency. Consequently, many models alter spatial resolution or simplify physical processes to make simulations feasible, though this often sacrifices detail and accuracy.

Chapter 4

A geophysical model to study oceanic flows

Equations derived in Chapter 3 were utilized to develop a geophysical model called PSOM (Process Study Ocean Model). PSOM is a three-dimensional, non-hydrostatic computational fluid dynamical model for oceanographic applications [19, 18]. The model utilizes a smooth boundary-fitted curvilinear grid to discretize the ocean domain, mapping the domain into a uniformly discretized cube in which solutions are obtained. Here, only the independent variables (t, x, y, z) in physical space are transformed into $(\tau, \xi, \eta, \sigma)$ in the computational domain, with dependent variables retaining their cartesian orientation [91, 18]. The free surface of the ocean corresponds to the top face of the cube in the computational domain. The seabed corresponds to the bottom face of the cube and the four lateral boundaries of the ocean are taken to be vertical surfaces. A σ-coordinate system is employed vertically, adapting smoothly to both the varying bottom topography and the open water surface. The σ-coordinate is defined as

$$\sigma = \left(\frac{z+d}{h+d}\right) N_k, \tag{4.1}$$

equation where N_k is the number of grid intervals in the vertical direction, d is the depth of the ocean floor, h is the free-surface elevation and z is measured positive upwards with reference to the mean sea level. The grid interval $\Delta\sigma$ is taken to be 1 and equation (4.1) is differentiated to obtain $\sigma_t, \sigma_x, \sigma_y, \sigma_z$ and can easily be modified for graded grid or stretched grid.

The domain is discretized into a consistent smooth curvilinear grid (ξ, η) in the horizontal plane, which remains constant over time. Since, the grid is same at each σ levels. Hence

$$\xi_t = 0, \eta_t = 0, \xi_z = 0, \eta_z = 0.$$

The time variable is independent of spacial coordinates and is unchanged by the mapping i.e., $\tau = t$, Hence

$$\tau_t = 1, \tau_x = 0, \tau_y = 0, \tau_z = 0.$$

The model applies the control volume formulation and position the variables as in [92]. The grid indices i, j, k corresponds to ξ, η, σ directions. N_i, N_j, N_k denotes the number of grid intervals in each direction. For $\Delta\xi = \Delta\eta = \Delta\sigma = 1$, the values of ξ, η, σ coincides with the grid indices and range from 0 at the boundary surface to N_i, N_j, N_k at the opposite boundary surface of the domain. Inside the domain, grid cells are denoted using the indices i, j, k, where $i = 1, ..., N_i, j = 1, ..., N_j, k = 1, ..., N_k$. To specify the boundary conditions, a layer of ghost cells has been placed outside the domain's boundary (at $i = 0, i = N_i + 1, j = 0, j = N_j + 1, k = 0, k = N_k + 1$). For every grid cell, there are specific faces: east, west, north, south, top, and bottom, represented as e, w, n, s, t, and b respectively. More details on the arrangements of grid and variables can be found in [18].

The model can be operated in two different modes: hydrostatic and non-hydrostatic [93, 94]. The approach employed is highly efficient and takes advantage of the fact that the ocean's depth is much smaller compared to its length, resulting in skewed problem. This leads to the quicker solution for the non-hydrostatic pressure through the use of multi grid method. The non-hydrostatic model has been utilized in various process studies, such as how nutrients are transported vertically for phytoplankton production [95] and examining the dynamics of submesoscale processes [94, 96]. The non-hydrostatic model is a suitable and well-defined approach with open boundaries, making it possible to use it as a nested model with high resolution, where time varying boundary conditions are employed from a general circulation model with coarser resolution. Therefore, this model is particularly useful for studies that require high-resolution modelling with specific and limited region [97].

4.1 Governing equations

Neglecting the viscous effect and wind forcing the non-dimensional system that constitute the quasi-non-hydrostatic free surface model presented in [19, 18] is given by

$$\frac{Ds}{Dt} = 0 \tag{4.2}$$

$$\frac{Du}{Dt} + \frac{1}{\epsilon}\left(gh_x + r_x + \delta q_x - fv + \epsilon\delta bw\right) = 0 \tag{4.3}$$

$$\frac{Dv}{Dt} + \frac{1}{\epsilon}\left(gh_y + r_y + \delta q_y + fu\right) = 0 \tag{4.4}$$

$$\frac{Dw}{Dt} + \beta\left(q_z - bu - \epsilon\lambda\frac{(u^2+v^2)}{a}\right) = 0 \tag{4.5}$$

$$u_x + v_y + \epsilon w_z = 0 \tag{4.6}$$

$$\rho = \rho(s, T) \tag{4.7}$$

$$\frac{\partial h}{\partial t} + \frac{\epsilon}{\mathcal{F}^2}\left[\frac{\partial}{\partial x}\left(\int_{-d}^{H/Dh} udz\right) + \frac{\partial}{\partial y}\left(\int_{-d}^{H/Dh} vdz\right)\right] = 0 \tag{4.8}$$

where

$$\frac{D}{Dt} = \frac{\partial}{\partial t} + u\frac{\partial}{\partial x} + v\frac{\partial}{\partial y} + \epsilon w\frac{\partial}{\partial z} \tag{4.9}$$

Here x and y are eastward and northward distances and z is the distance from the surface in a direction anti-parallel to gravity, t is time, ϵ is the Rossby number, $\mathcal{F}$ is the Froude number and u, v and w are the velocity components in x, y and z direction respectively. f and b are the dimensionless Coriolis parameters resolved in the normal and tangential component on earth's surface at a given point and are twice the earth's angular velocity. s represents the salinity, T the potential temperature, h the elevation of the free surface, q the non-hydrostatic component of the pressure, r the hydrostatic component of the pressure, ρ the potential density and a the distance from the center of the earth. λ is the ratio of characteristic horizontal length scale to the characteristic value of the earth's radius, δ is the ratio of depth to length scale (aspect ratio) and H/D is the ratio of characteristic free-surface elevation to depth scale. The transformed form of the equations (4.2)-(4.8) in the curvilinear coordinates can be found in [18].

To simulate the volcanic eruption, we introduced a Gaussian heat flux profile at the seabed (see Figure 4.1). By considering a small heat flux system will resemble a slow volcanic eruption. Hence, we will use the equation of heat transport provided in Chapter 3, to model the heat flow.

The governing equations outlined in Chapter 3 can be simplified to the provided equations by taking into account the considerations and non-dimensionalization methods detailed in [19].

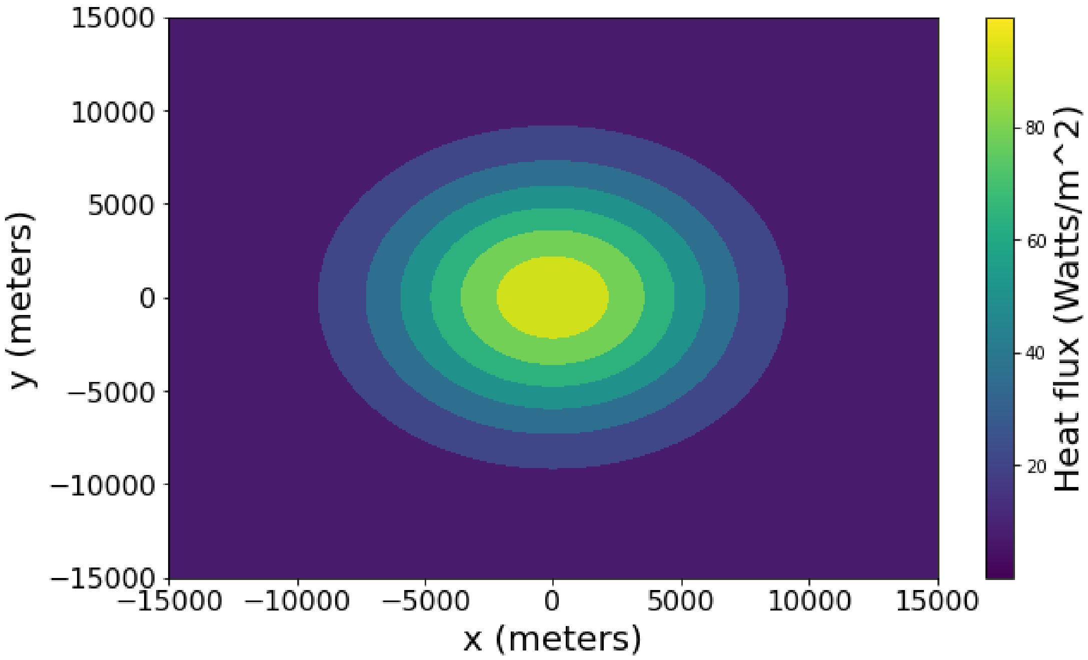

Heat flux profile

Figure 4.1: Example of Gaussian heat flux profile introduced at the seabed.

4.2 Boundary and initial conditions

The boundary conditions in the transformed coordinates are as follows:

The flux components u and v are assumed to be zero at the lateral boundaries of the domain.

Due to heat flux at the bottom boundary we introduce the boundary condition at seabed as

$$\kappa \frac{\partial T}{\partial z} = \frac{Q}{\rho c_p}, \tag{4.10}$$

where Q is specified heat flux at the bottom boundary, c_p is the heat capacity, ρ is the density.

At the time $t = 0$, the velocities u, v, and w are all initialized to zero, meaning the water is initially motionless.

The detailed solution procedure of the equations (4.2)-(4.10) can be found in [18].

4.3 Setting-up PSOM

Download PSOM from GitHub. The following additional packages are required:-

1. Install gcc and gfortran using `sudo apt-get install gcc gfortran`

2. NetCDF libraries

   (a) Install using `sudo apt-get install libnetcdf-dev libnetcdff-dev`

   (b) Check NetCDF-C and FORTRAN configuration

   `nc-config{all`

   `nf-config{all`

   (c) Install ncdump (used to view the data generated) using

   `sudo apt install netcdf-bin`

   (d) Install ncview (used to view the graphs) using

   `sudo apt install ncview`

3. Install Makedepend using

   `sudo apt-get install xutils-dev`

4. Install CMake using

   `sudo apt-get -y install cmake`

4.4 Running PSOM

After installing the required packages enter in the **code** folder and execute the following steps:

1. `optfile`: Open optfile using VIM or gedit and modify the following parameters:-
   (a) `fcomp = gfortran`
   (b) define `netcdf=T` (if netcdf is to be used or use F).
   (c) `define gotm=T` (if gotm is to be used or use F).
2. `sh tools/clean.sh`: Before the start of any simulation, the environment needs to be cleaned using this command (cleans all the contents inside the mkfile folder except the files: nh and Makefile).
3. `sh tools/configure.sh` (compile PSOM using default setup). To compile the specific experiment say experiment_A use

   `sh tools/configure.sh experiment_A`

   Running compile.sh will (1) create makefile in the folder mkfile, and (2) compile the Fortran code. A failure during running the compile.sh most likely indicates that there is an error in the Fortran code.
4. To run the model use

   `./exe/nh_experiment_A < ./experiment_A/namelist_experiment_A`

   It uses namelist file to define the experiment's parameters (exapmle, time step, output path, user variables, etc.) ' The output files are created in output directory under parent folder (outside code folder).
5. To plot the data contained in .cdf files, first change the current directory from **code** to **output** and then use

   `ncview filename`
6. To view the data contained in the .cdf files use

   `ncdump filename`

4.5 Opening NetCDF files in Python

The data generated in NetCDF file in output directory can be open in python using xarray package. The array data can then be plotted using Matplotlib library for visualisation.

```
In [1]: import numpy as np
        import xarray as xr
        import matplotlib.pyplot as plt
        import pandas as pd

In [2]: path='/Users/manishkanojia/Downloads/'
        fname='novolcano.cdf'
        ds=xr.open_dataset(path+fname)
        ds

Out[2]: xarray.Dataset

        ▶ Dimensions:      (x: 96, y: 192, time: 6, ntr: 1, nconsume: 1)
        ▶ Coordinates:  (0)
        ▶ Data variables:  (21)
        ▶ Attributes:  (0)

In [3]: path4='/Users/manishkanojia/Downloads/'
        fname4='zslice_032.cdf'
        ds4=xr.open_dataset(path4+fname4)
        ds4 #wf0.00001

Out[3]: xarray.Dataset

        ▶ Dimensions:      (x: 96, y: 192, time: 6, ntr: 1, nconsume: 1)
        ▶ Coordinates:  (0)
        ▶ Data variables:  (21)
        ▶ Attributes:  (0)
```

Figure 4.2: Example code snippet to effortlessly open NetCDF files in python.

4.6 Creating new experiment in PSOM

To begin a new experiment, you first create a directory for the experiment and include subdirectories for organization. For instance, if the experiment is named `Volcanic_flows`, you would first create a directory called `volcanic_flows/`, and within it, two subdirectories: `volcanic_flows/inc` and `volcanic_flows/src`.

Next, you would copy any relevant subroutines from the `model/` directory into the `volcanic_flows/src` subdirectory, where they can then be modified as needed. For example, to copy the subroutine `heat_flux.f90` from the `model/src` directory to the `volcanic_flows/src` directory, you would use the following command:

```
cp model/src/heat_flux.f90 volcanic_flows/src
```

The compiling step includes a superseding procedure that will take into account the new version of `heat_flux.f90` and disregard the standard version from `model/src`. More preciesely, it will create the makefile based on thie new state of the model (in `./mkfile`), compile and create the executable `exe/nh_my_experiment`.

4.7 Defining model grid

The grid size is defined in `size.h`. To modify the grid size, copy `size.h` in the experiment directory:

`cp model/inc/size.h volcanic_flows/inc`

Choose the grid dimensions NI, NJ, NK (i.e., number of grid cells in x, y and z directions) such that the grid can be subdivided a maximum number of times by a factor of 2 to form `ngrid` level of grids. For example, choosing $NI = 48$, $NJ = 24$ and $NK = 32$ constrains the grid levels to `ngrid`$= 4$, as:

$$NI : 48; 24; 12; 6; 3 \quad \textit{(Five grid levels)}$$

$$NI : 24; 12; 6; 3 \quad \textit{(Four grid levels)}$$

$$NI : 32; 16; 8; 4; 2 \quad \textit{(Five grid levels)}$$

4.8 Defining parameters for the experiment

The file `namelist` defines key parameters related to the experiment (e.g., grid resolution, time step, fplane, diffusion, time step, output, ...). This file should be coppied in experiment directory.

Some of the key parameters defined are as follows:

1. TIME SETTING

   nsteps=1000, (number of time steps)

   dtime_dim=60d0, (time step (in sec))

2. HYDROSTATIC

   fnhhy=1.0d0, (1 if simulation is non-hydrostatic, 0 otherwise)

3. PLANETARY VORTICITY

   fplane=0, (1 if simulation is on a f-plane, 0 if f varies as sin(latitude))

   phi0deg=48, (phiθdeg is the central latitude (in degree))

4. DIFFUSION AND FRICTION

   Kx=1d0, (diffusion in the horizontal, x direction (in m*m/s))

   Ky=1d0, (diffusion in the horizontal, y direction (in m*m/s))

   RR=0d0, (bottom friction (in m/s))

4.9 Application of PSOM model

Process Study Ocean Model (PSOM) has been widely used in oceanographic research, particularly for studying the physical processes driving ocean circulation, mixing, and turbulence at various scales [95, 94, 96, 98, 99, 100, 101, 102, 103, 104, 105, 97, 93, 106]. Here, we delve into the key applications of PSOM, with an emphasis on its relevance to the oceanographic research.

1. **Vertical mixing and ocean stratification:** Vertical mixing in the ocean is a fundamental process that influences the distribution of heat, nutrients, and dissolved gases between the surface and deeper layers. Ocean stratification, which refers to the layering of water masses with different densities, is maintained or disrupted by vertical mixing. This balance is critical for the ocean's role in regulating global climate and supporting marine ecosystems. PSOM has been instrumental in studying the small-scale physical mechanisms underlying vertical mixing, such as shear instabilities, internal wave breaking, and turbulence induced by wind and surface forcing.

   For instance, studies utilizing PSOM have shed light on how episodic wind events drive the vertical transport of nutrients from nutrient-rich deep layers to the euphotic zone, fostering biological productivity. Additionally, PSOM has been used to explore how stratification patterns evolve in response to seasonal changes and external forcing. The model's ability to resolve fine-scale processes provides an ease in investigating the feedback between mixing and stratification, with significant implications for climate modeling and ocean biogeochemistry.

2. **Submesoscale dynamics and eddies:** Submesoscale dynamics encompass processes at spatial scales of 1 to 10 kilometers, which are smaller than those typically resolved in traditional ocean circulation models. These processes, including the formation and dissipation of submesoscale eddies, play a vital role in the ocean's energy cascade, transport mechanisms, and vertical exchanges. PSOM's high-resolution capabilities make it particularly well-suited for exploring submesoscale features and their interactions with larger-scale flows.

   For example, PSOM has been employed to study the life cycle of submesoscale eddies and their role in vertical nutrient fluxes and horizontal dispersion. Such studies have revealed that submesoscale eddies significantly enhance mixing and redistribute heat, salt, and momentum, thereby influencing ocean circulation patterns and energy dissipation. Furthermore, PSOM's ability to model the impact of submesoscale instabilities on mesoscale features has provided insights into the processes that sustain small-scale variability in ocean systems.

3. **Upwelling and ocean surface currents:** Upwelling is a crucial oceanographic phenomenon where deep, nutrient-rich waters are brought to the surface, fostering primary production and supporting marine ecosystems. This process is particularly pronounced in coastal regions and areas influenced by ocean surface currents and eddy interactions. PSOM has been applied to investigate the mechanisms driving upwelling, including wind-driven circulation, Ekman transport, and interactions with bathymetric features.

   By simulating the coupling between surface currents and subsurface processes, PSOM has helped clarify the dynamics of upwelling in regions such as the California Current System and the Benguela Upwelling System. The model has also been used to assess how variations in wind forcing and mesoscale eddy activity influence the intensity and spatial extent of upwelling. These studies have important implications for fisheries management, carbon cycling, and the prediction of biological hotspots.

4. **Turbulent mixing and convection:** Turbulent mixing is a cornerstone of oceanic energy and mass transfer processes, driving the exchange of properties like heat, salt, and momentum. Convection, often triggered by surface cooling or brine rejection during sea ice formation, further enhances this mixing, particularly in polar and subpolar regions. PSOM has been widely used to investigate the intricate dynamics of turbulent mixing and convection under various forcing conditions.

   For example, PSOM simulations have provided detailed insights into how wind-driven turbulence interacts with surface buoyancy fluxes to produce mixed layer deepening. In regions such as the Southern Ocean, where strong winds and intense convection dominate, PSOM has been employed to study the formation of deep-water masses, a key component of the global thermohaline circulation. By resolving turbulence at small scales, the model enables researchers to quantify mixing rates and understand their variability across different ocean regimes.

5. **Modeling ocean heat transport:** Ocean heat transport plays a critical role in regulating Earth's climate by redistributing heat from the equator to the poles. Understanding the contribution of small-scale processes like submesoscale eddies and turbulent mixing to heat transport is vital for improving climate models. PSOM's capacity to simulate fine-scale processes has made it a valuable tool for exploring the complexities of ocean heat dynamics.

   For instance, PSOM has been used to assess how submesoscale features contribute to lateral and vertical heat fluxes in the upper ocean. Studies have also employed the model to evaluate the interplay between mesoscale and submesoscale processes in shaping regional heat budgets. These findings are crucial for predicting the response of ocean heat transport to climate change and its feedback on atmospheric circulation patterns.

6. **Ocean currents and deep water circulation:** Large-scale ocean currents, including the meridional overturning circulation (MOC), are fundamental to the global climate system. PSOM has been applied to study the dynamics of these currents and the role of eddies and small-scale mixing in modulating their

behavior. By resolving processes such as eddy-induced transport and bottom boundary layer interactions, PSOM has advanced our understanding of deep water formation and circulation.

For example, PSOM has been used to simulate the interaction between deep western boundary currents and topographic features, shedding light on how such interactions influence water mass transport. Additionally, the model has been employed to investigate the sensitivity of the MOC to changes in surface forcing, providing insights into its stability and potential tipping points under future climate scenarios.

7. **Oceanic fronts and boundary layers:** Oceanic fronts, characterized by sharp gradients in temperature, salinity, or velocity, are key sites of energy and mass exchange in the ocean. Boundary layers, where the ocean interacts with the atmosphere or seafloor, are equally critical for understanding momentum and heat transfer. PSOM has been widely used to explore the dynamics of these regions, which are often challenging to study in situ.

   For example, PSOM simulations have revealed how frontal instabilities generate submesoscale eddies, enhancing vertical fluxes of heat and nutrients. The model has also been applied to study the structure and variability of boundary layers under different wind and buoyancy forcing conditions, with implications for air-sea interaction and sediment transport.

8. **Ocean-atmosphere interaction and climate variability:** The interaction between the ocean and atmosphere drives many aspects of climate variability, including phenomena like El Niño-Southern Oscillation (ENSO) and the North Atlantic Oscillation (NAO). PSOM has been employed to investigate how changes in atmospheric forcing, such as wind stress and heat fluxes, affect ocean surface properties and circulation patterns.

   Studies using PSOM have highlighted the role of submesoscale processes in modulating air-sea fluxes and their feedback on larger-scale climate modes. For instance, the model has been used to explore how submesoscale eddies influence surface temperature anomalies during ENSO events, contributing to a more nuanced understanding of climate variability. These applications underscore PSOM's importance in bridging small-scale ocean dynamics and global climate systems.

9. **Seagrass Deformation and Instability in Canopy Flow:** One of the advanced applications of the Process Study Ocean Model (PSOM) is in simulating interactions between fluid flow and aquatic vegetation. A recent study used a non-hydrostatic version of PSOM to investigate the dynamics of submerged seagrass beds under unidirectional flow. The research focused on monami, a phenomenon characterized by the synchronized waving of seagrass blades in response to flow-induced instabilities. By incorporating the deformable and buoyant properties of seagrass into PSOM, the study revealed critical insights into the relationship between grass deformation, flow instability, and material exchange.

   The study also explored material exchange between the seagrass canopy and overlying water. Results showed that higher Reynolds numbers and buoyancy parameters produced stronger vortices and enhanced tracer exchange. However, excessive grass deformation dampened vortex strength and reduced exchange efficiency, highlighting an optimal range for material transport.

   This application of PSOM offers valuable insights into coastal ecosystem processes, such as nutrient transport and sediment dynamics. It also highlights the model's potential for further studies involving fluid-vegetation interactions and ecosystem management.

The above detailed overview illustrates that PSOM is a versatile numerical modeling framework and it has significantly contributed to advancing our understanding of ocean dynamics, particularly in areas requiring high-resolution insights. With the research presented in this thesis, we extend the application of PSOM model to the realm of submarine volcanoes and hydrothermal vents. The introduction of heat flux at seabed accounts for the heat introduced during these events.

Chapter 5

Convection induced by deep submarine volcanic eruption in stratified oceans

To investigate the flows produced by small underwater volcanic eruptions, we will utilize the PSOM model outlined in Chapter 4. In simulating the volcanic eruption, we will incorporate a modest heat flux at the seafloor, as elaborated upon in Chapter 3. The ocean is linearly stratified in temperature and salinity with respect to depth. However, the initial zonal, meridional and vertical velocities are all set to zero. This means that at the outset of the simulation, there are no initial movements in the horizontal and vertical directions. This initial condition provides a starting point for the model to capture the evolution of currents and velocities as influenced by the introduced heat flux during the underwater volcanic eruption. The subsequent dynamics of the system will be shaped by the interplay between the imposed heat source and the evolving flow patterns.

5.1 Scenarios explored through computational modeling

This study explores two distinct scenarios based on geographical locations on Earth. In scenario (a), the focus is on a region near the equator where temperature primarily governs stratification, and the presence of submarine volcanoes is notable, particularly within the Pacific Ring of Fire [74]. Recent modeling efforts [90] delve into the impact of submarine volcanic eruptions on equatorial flows, providing valuable insights. In scenario (b), attention shifts to regions near the poles where the stratification is primarily governed by salinity. The studies presented in [5, 74, 76, 75] discuss subglacial volcanism beneath the west Antarctic ice sheet.

With the buoyancy frequency $N^2 = 10^{-5}$ 1/s^2 and a density gradient of 0.00103 kg/m^4. The two aforementioned cases are initialized as follows in our study:

Case (a) maintaining a constant salinity of 32 ppt while the initial condition for temperature varies from 1.9°C to 16.2°C, resulting in density ranging from 1029 kg/m^3 at the seabed at a depth of 3000 meters to 1026 kg/m^3 at the free surface.

Case (b) maintaining a constant initial temperature of 0°C and varying salinity initially from 36.89 ppt to 33.07 ppt, corresponding to density changes from 1029 kg/m^3 at the seabed at a depth of 3000 meters to 1026 kg/m^3 at the free surface.

In both the cases, a Gaussian heat flux distribution was implemented at the seafloor, featuring a peak heat flux of 100 watts/m^2 at the center (see Figure 5.1 (a)), given by

$$Q = 100e^{-\left(\frac{(x-x_c)^2}{2(\sigma_x)^2}+\frac{(y-y_c)^2}{2(\sigma_y)^2}\right)}, \tag{5.1}$$

where x_c and y_c denotes the centre of the volcano with maximum heat flux and σ_x and σ_y denotes the standard deviation along the x and y axis. This applied heat flux decreases linearly in time to zero over the course of one week. Following this initial week, the heat flux remains at zero for another few days (see Figure 5.1 (b)).

In addition to the two primary cases mentioned above, we also consider two sub-cases where the initial intensity of stratification is reduced in comparison to the main cases.

Sub-case (a) maintaining a constant salinity of 34.5 ppt while varying initial temperature from 0°C to 4.5°C, resulting in density ranging from 1027.6 kg/m^3 at the seabed at a depth of 3000 meters to 1027.3 kg/m^3 at the free surface.

Sub-case (b) maintaining a constant initial temperature of 0°C and varying salinity from 34.5 ppt to 34.10 ppt, corresponding to density changes from 1027.6

kg/m^3 at the seabed at a depth of 3000 meters to 1027.3 kg/m^3 at the free surface.

The sub-cases are considered to assess the influence of stratification on the ascent of the plume, as experimental studies have highlighted that stratification governs the buoyant behavior of the plume [107, 108, 109].

The simulations were conducted on an f-plane, at a latitude of 45 degrees for scenario (a) and 65 degrees for scenario (b). We use positive f even though case (b) represents the southern ocean. The main objective is to present a comprehensive three-dimensional picture of the flow, focusing on the analysis of rotational and radial velocities to elucidate the mechanisms underlying plume formation and the entrainment of cold seawater within the plume. A primary aim is to discern the impact of temperature and salinity controlled stratification on the flows engendered by volcanic eruptions.

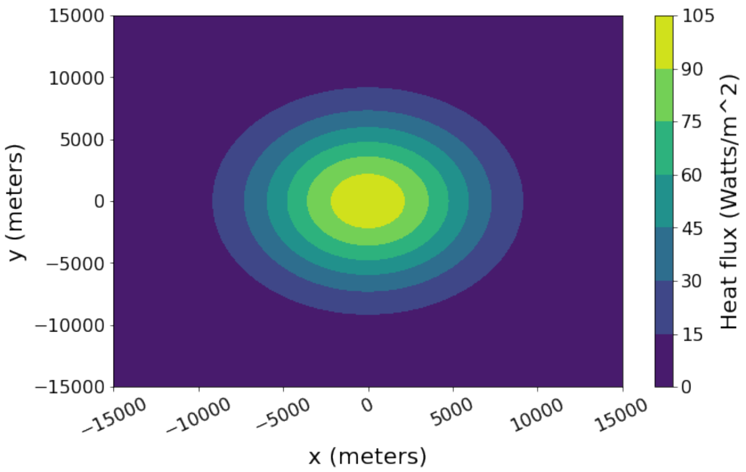

(a)

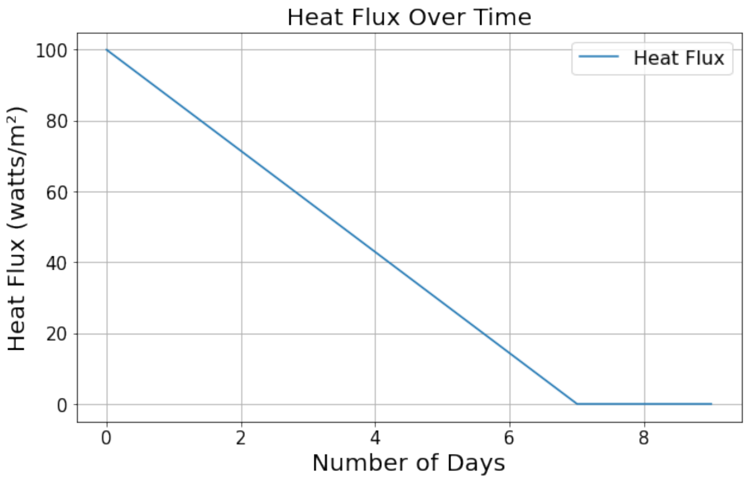

(b)

Figure 5.1: (a) Heat flux profile introduced at the seabed, (b) linear variation in heat flux with respect to time.

5.2 Model parameters

The domain's dimensions are 30 kilometers in both the x and y directions. The total depth of the ocean is taken as 3000 meters. Mean salinity $S_0 = 35.70$ ppt, mean temperature $T_0 = 15°$C and mean density $\rho_0 = 1027$ kg/m^3. The value of earth's angular velocity is 7.272×10^{-5} rad/sec, the magnitude of Coriolis parameter is 10^{-4} rad/sec, the acceleration due to gravity on the surface of the earth at sea level is 9.81 m/s^2, value of Earth's radius is 6371 km. The grid dimensions are as follows $NI = 128, NJ = 128$, and $NK = 36$ in x, y and z dimensions respectively. The diffusion and viscosity in both the horizontal x and y directions is 2 m^2/s and vertical diffusion is 10^{-5} m^2/s. Damping has been implemented at the boundaries to prevent reflections generated when the flow reaches the perimeter.

5.3 Results

5.3.1 Angular velocity

In both the cases (a) and (b), rotational flows were detected in the region spanning from the ocean floor to the free surface (Figure 5.2 (a)), a phenomenon highlighted in [71, 72, 73] due to convection. However, our simulations reveal a noteworthy observation: the flows gradually change from cyclonic near the seabed to anticyclonic and, maintain this direction until the free surface. This alteration in flow direction is consistent with findings in Rossby's experimental study [71]. Further, alternating behavior of the flow align with the sinusoidal pattern of vertical structure function (see Figure 5.2 (b)), this indicates that the angular velocity variations at different depths and horizontal positions are influenced by the structure of the baroclinic mode. The depth at which the first baroclinic mode has a single zero crossing exhibits a more varied pattern, with a shift between positive and negative values indicating the transition from cyclonic to anticyclonic in both the cases (see Figure 5.2). The identified rotational pattern further substantiates the conclusions outlined in [73], wherein two vertically aligned convective cells are delineated. The rotation observed in the upper cell is attributed to the heat transfer originating from the lower cell. In the current investigation, the upper cell exhibits an anticyclonic rotation, while the lower cell has cyclonic rotation.

In both the cases, higher rotational speed was noted in the vicinity of the volcano, with a subsequent decrease in rotational speed observed as one moves away from the volcano. Specifically, it can be stated that the lower cell exhibited higher rotational speed compared to the upper cell. On day 6, the peak angular velocity observed above the volcano in the lower cell reached 0.24 m/s for case (a) and 0.23 m/s for case (b). Meanwhile, the maximum angular velocity in the upper cell was 0.19 m/s for case (a) and 0.17 m/s for case (b).

5.3.2 Radial flows

In Figure 5.3 (a) and (b), the alternating red and blue bands along $r = 0$ represent radial convection cells. The distribution of these cells around the central axis indicates a balanced distribution of thermal energy and fluid flow in both the cases. This balance occurs because the energy input from the heat flux is balanced by the convective heat transport, resulting in a stable flow pattern. Such radial flow structures are consistent with observations reported in previous experimental studies [109, 108, 107]. Also, Figure 5.3 illustrates that as more heat is supplied to the system and the warm plume rises, the number of radially convective cells also increases. This trend continues until the heat flux approaches zero on day 7. Until this point, the intensity of both inward (blue) and outward (red) flow velocities were maximum near the central axis ($r = 0$), where the heat flux is most concentrated. As one moves horizontally away from the central axis, the alternating bands of flow intensity gradually diminish, reflecting the reduced influence of the heat flux with increasing distance from the center.

In case (b), axially symmetric cells emerge at the edges of the plume (Figure 5.3 (b) and 5.4). The development of such axially symmetric cells in salinity-stratified environments has been observed in earlier experimental studies [109, 108]. This phenomenon can be explained as follows: as the plume rises, radially convective cells form, and the outward movement of these cells transports heated fluid from the plume's core towards its outer edges. This process causes warm water to accumulate near

(a) Angular velocity

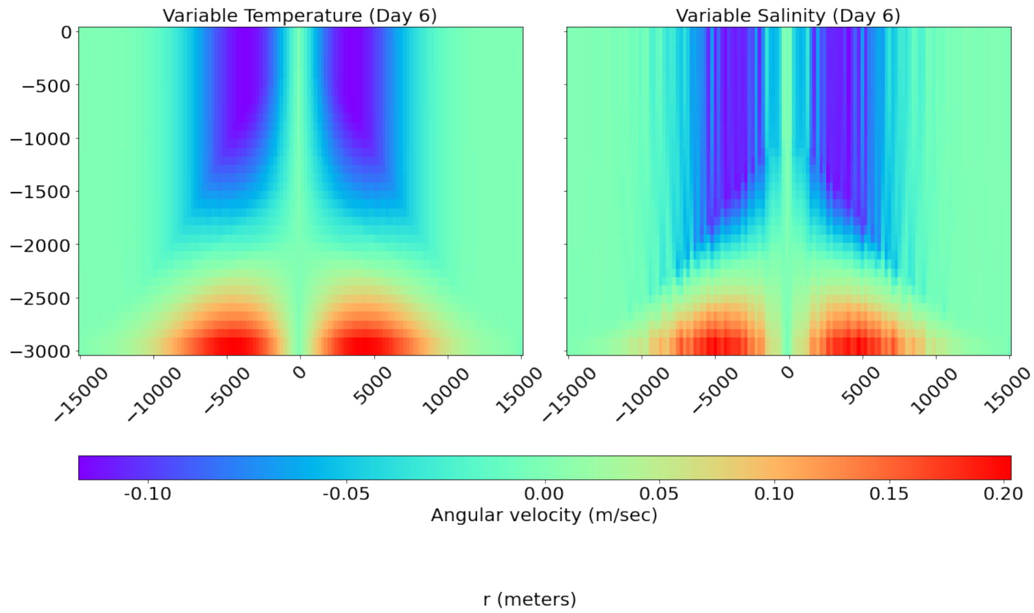

(b) First baroclinic mode

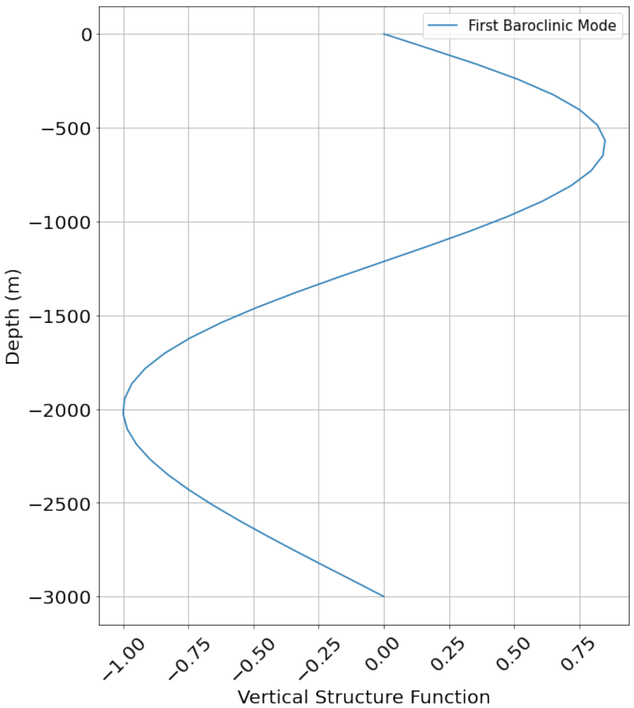

Figure 5.2: (a) Contour plots for angular velocity plotted in (r, z)-plane, showing a cyclonic rotation near the seabed and anti-cyclonic rotation near the free surface. (b) plot for first baroclinic mode.

the plume's boundary, creating a layer of heated fluid around the convective cells' edge. At the plume's periphery, the warm water encounters the cooler surrounding fluid, which is at a temperature of 0°C. This interaction results in sharp temperature gradients (see Figure 5.5) and corresponding horizontal density differences (see Figure 5.7 (b)). The combination of these gradients and the stratified environment leads to the formation of axially symmetric circular convective patterns around the plume (as seen in Figure 5.4 and Figure 5.6). It is evident from Figure 5.3 that axially symmetric flows also form in case (a), though they are relatively weak due to temperature stratification. The temperature gradient, caused by the water being transported to the plume's edge, is small and smooth (see Figure 5.5), leading to the development of a weak axial flow. However, this flow does not dominate the radial flows near the central axis $r = 0$ as in case (b) (see Figure 5.6 (c and d)).

In case (b), as time progresses, the outward flow of hot water persists, leading to an increased buildup of heat at the plume's edges. As the temperature differences between the warm boundary and the cooler surroundings intensify, the system becomes thermally unstable. This instability causes the breakdown of the symmetric cells (Figure 5.4), driving the system into a more chaotic or irregular state of convection (as shown in Figure 5.3 (b), 5.6 (c) and (d)). The fluid flow becomes less orderly and more turbulent as the heat continues to spread through the stratified liquid. Such chaotic fluid behavior has been previously noted in earlier studies [109, 108]. In Figure 5.3 (b), it is observed that the axisymmetric flow or sheet at the plume's edge moves inward toward the plume's center, progressively narrowing the plume. This process continues until it reaches the center (see Figure 5.6). As noted in previous studies [109, 108], a bell-shaped sheet structure forms outside the plume within a salinity-stratified environment. This is also observed in our experiment for case (b) as can be seen in Figure 5.4 (b), it should be noted that the axially symmetric cells formed on the periphery of the plume gives rise to this bell shaped structure as discussed in [109, 108].

Figure 5.6 shows line plots generated at various depths ($z = 0$ representing the free surface, $z = -1459$ for an intermediate depth, and $z = -2918$ just above the heat source), plotted against the variable x. As a continuous heat flux is applied to the system peaking on day 1 and gradually decreasing each day an inward flow appears directly above the volcano on days 1 and 3. As we move upward to intermediate depths, however, the flow shifts outward and continues outward to the free surface (see Figure 5.6 (a) and (b)). Notably, in case (b) on day 3, there is a minor outward flow near the bottom and a slight inward flow at both intermediate depths and the free surface. This pattern is attributed to axial flows created by the sharp and substantial temperature gradient in case (b) (see Figure 5.5), as discussed previously. On day 7, when the heat flux reduces to zero, an inward flow begins to develop at both the intermediate depth and the free surface near the central axis $r = 0$ in case (a). As the system progresses toward equilibrium, by day 9, an outward flow starts to emerge near the seabed, while a dominant inward flows appear at the intermediate depth and the free surface (see Figure 5.6 (c) and (d)). This can be attributed to cold water seeping into the plume, as no additional heat flux is being introduced into the system. It is important to note that, as previously mentioned, the system with variable salinity exhibits chaotic behavior. Here, the flow developing at the edge of the plume starts shifting toward the center, narrowing the plume and destabilizing the entire system, as shown in the radial velocity plots for day 7 and day 9 in case (b) (Figure 5.6, (c) and (d)) and density anomaly plots presented in Figure 5.7 (b).

5.3.3 Vertical flow

In Figure 5.7 (a) and (b), the vertical movement of the plume is evident from the observed positive vertical velocity directly above the heat source. The addition of heat to the system causes the water in this region to become warmer and, consequently, less dense. This temperature-induced reduction in density generates a buoyant force, which drives the heated fluid upwards. As a result, a vertical plume forms, with the warm, rising fluid being convected away from the heat source. This plume is a clear manifestation of the convective process, where the upward motion of the less dense, heated fluid displaces the cooler, denser fluid around it. The formation of such plumes is discussed in detail in [6, 110, 84]. Also, the fluid behavior observed in Figure 5.7 (a) and (b) is symmetric about $r = 0$, indicating that the plume is well-developed.

(a) Case (a)

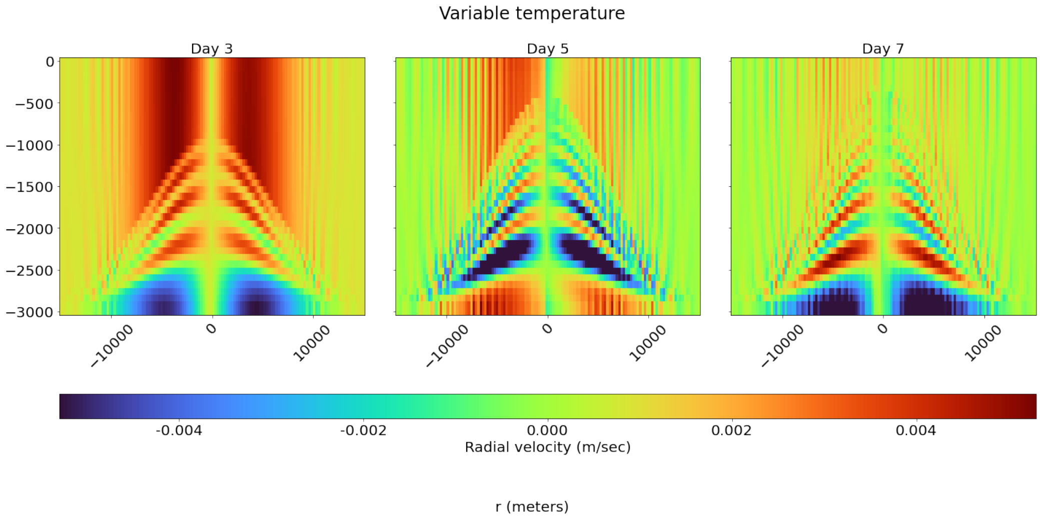

(b) Case (b)

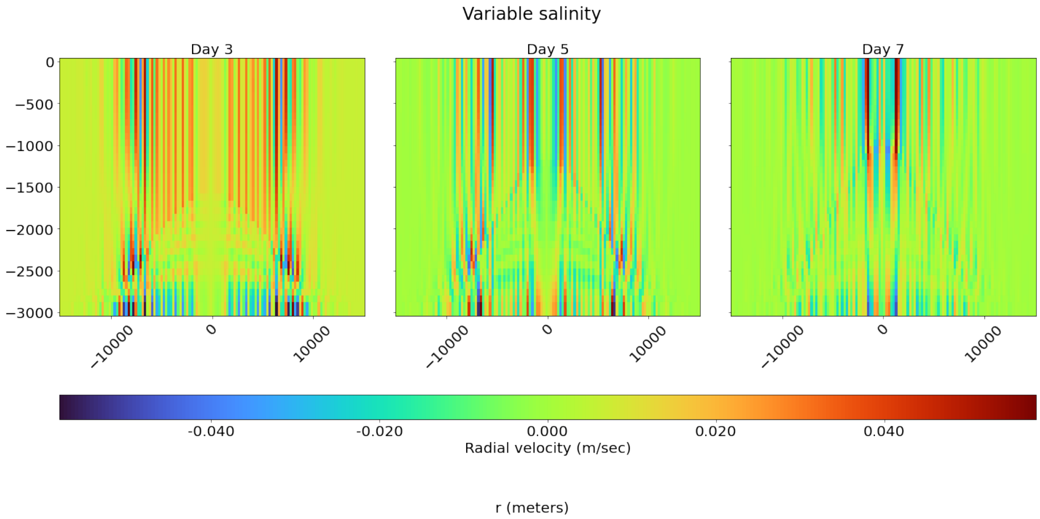

Figure 5.3: Contour plots for radial velocity plotted in (x, z)-plane with $y = 0$ meters, showing the radially convective cells in both cases and axially symmetric flow and chaotic behavior in case (b).

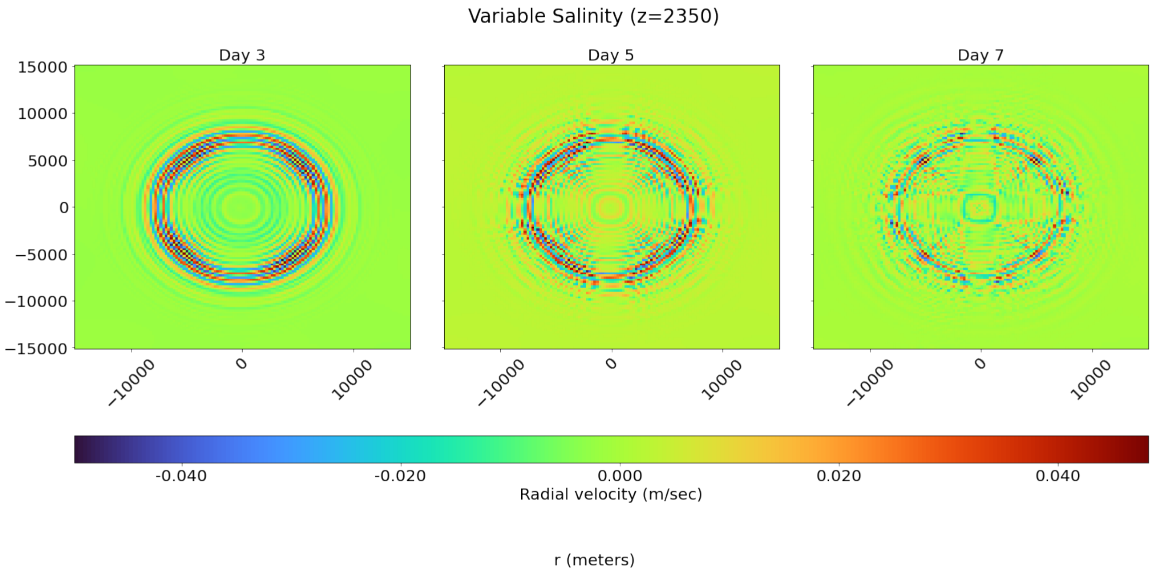

Figure 5.4: Contour plots for radial velocity for case (b) at z = 2350 in (x, y)-plane, showing the axially symmetric cells/sheets and turbulent behavior on and after day 5.

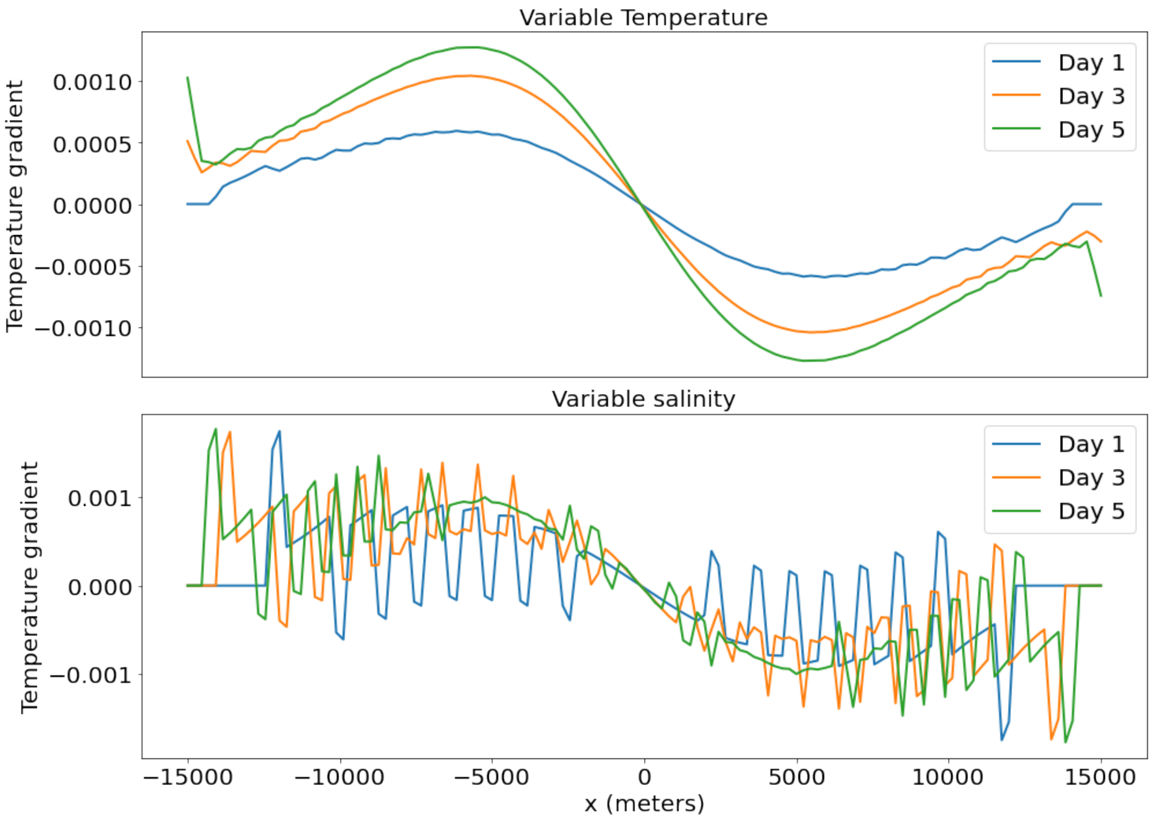

Figure 5.5: Temperature gradient at $z = 2837$ for both case (a) and (b).

(a) Day 1

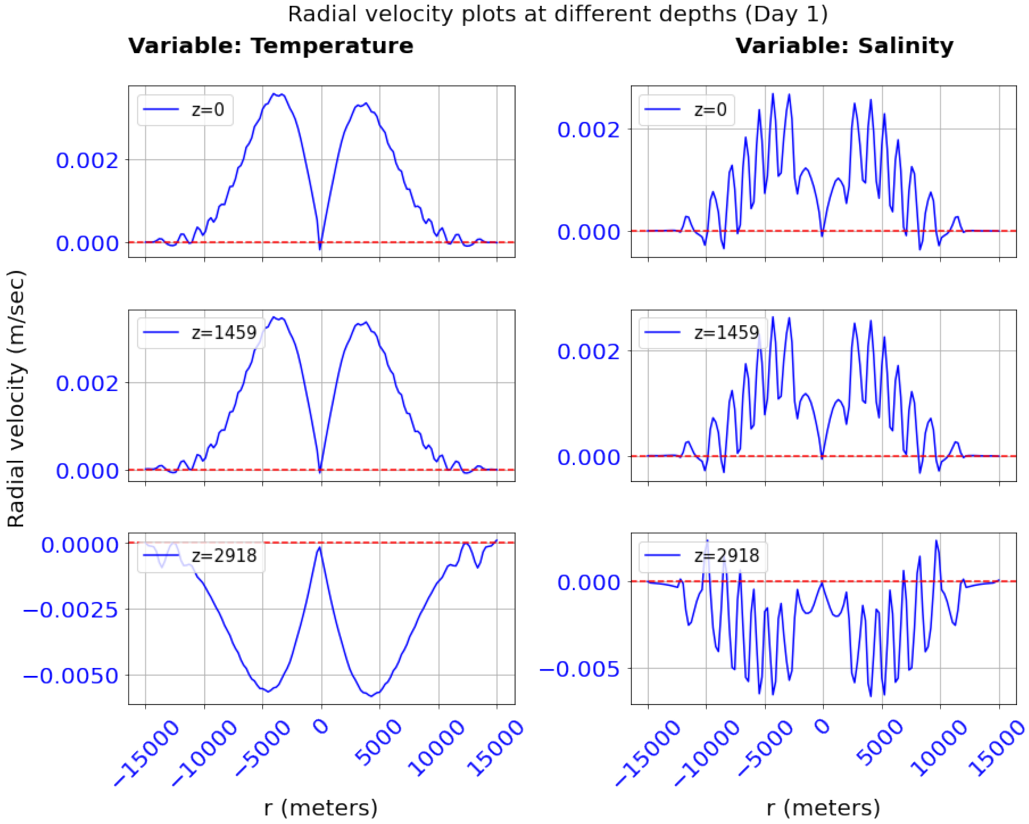

(b) Day 3

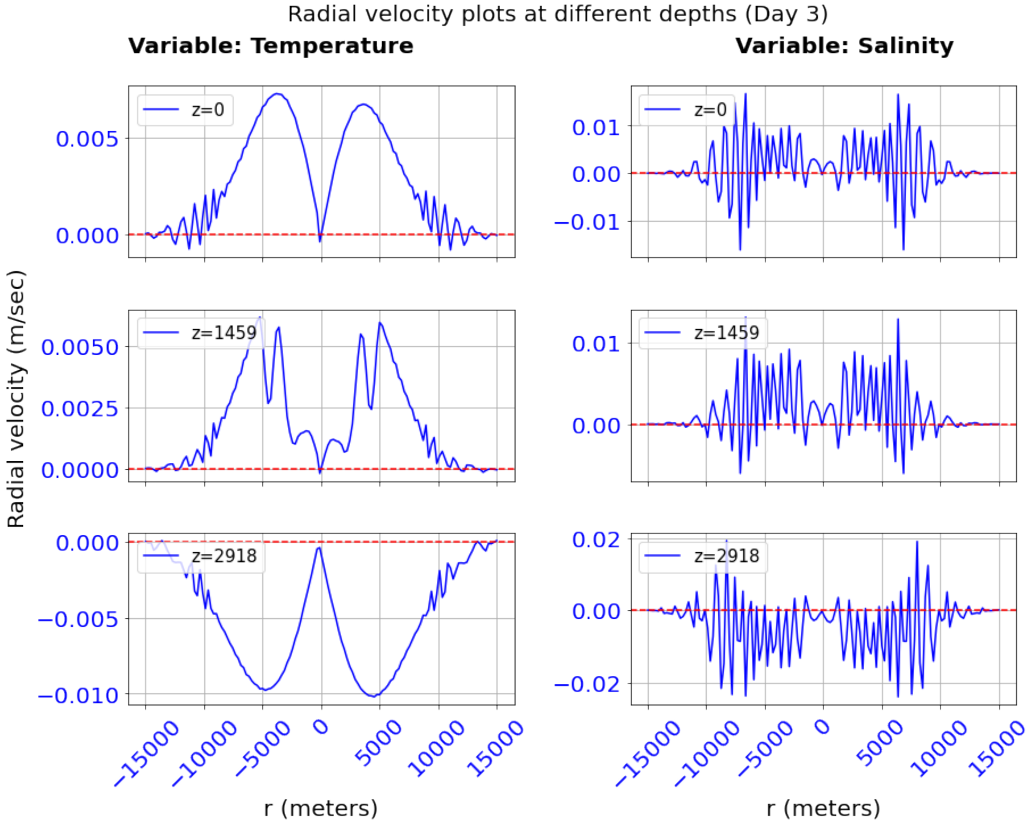

Figure 5.6: (a) Line plots for radial velocity (m/sec) at different depths for different days plotted against x (meters), red line shows the zero velocity value.

(c) Day 7

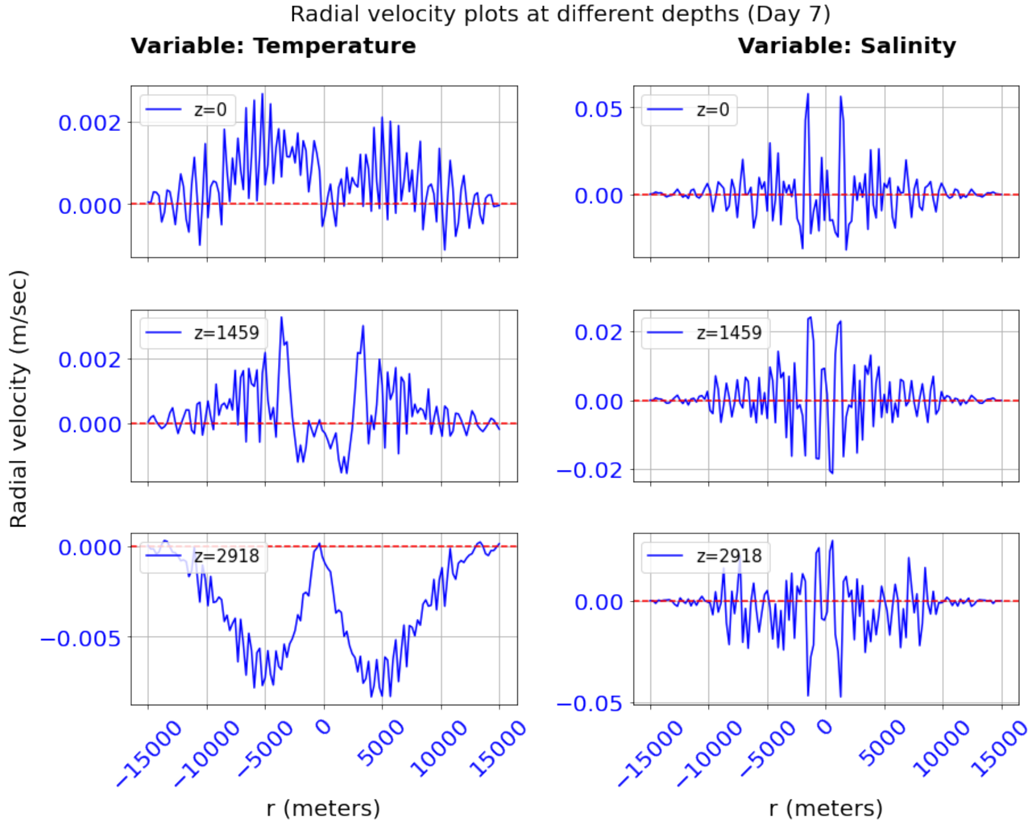

(d) Day 9

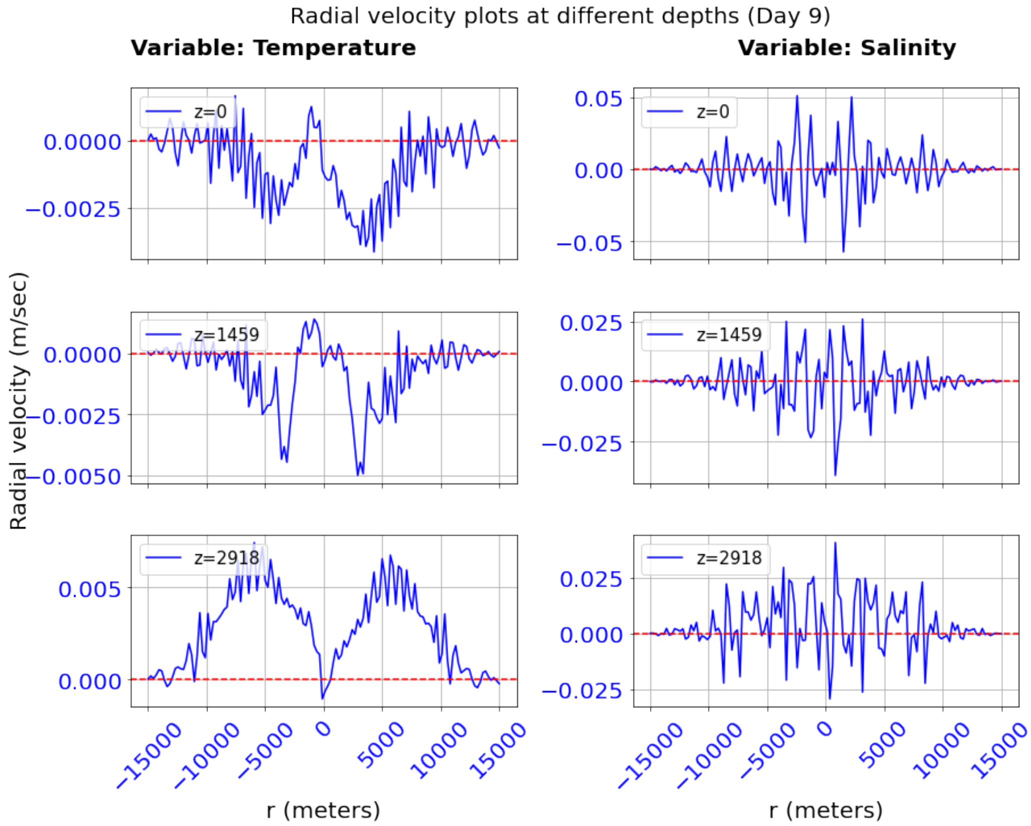

(Continued) Line plots for radial velocity (m/sec) at different depths for different days plotted against x (meters), red line shows the zero velocity value.

(a) Case (a)

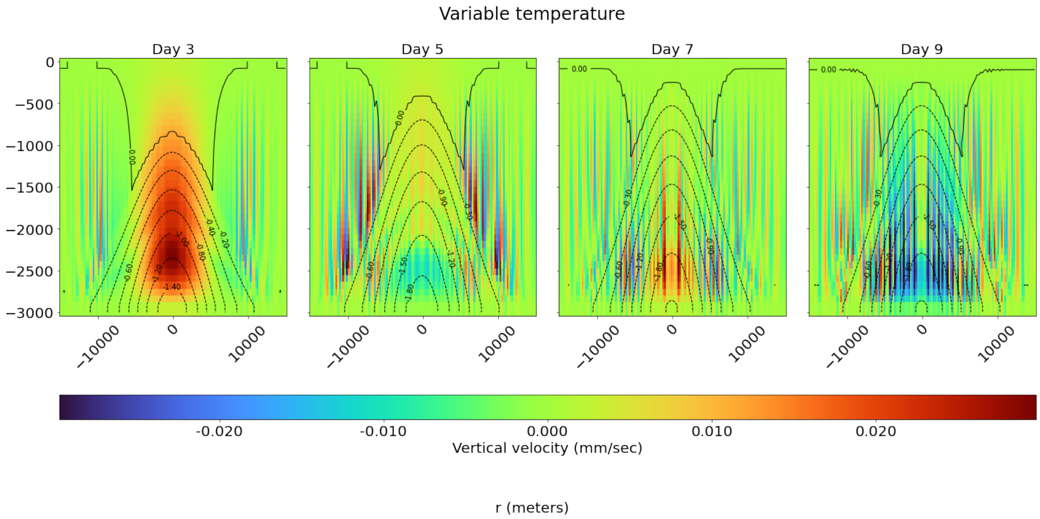

(b) Case (b)

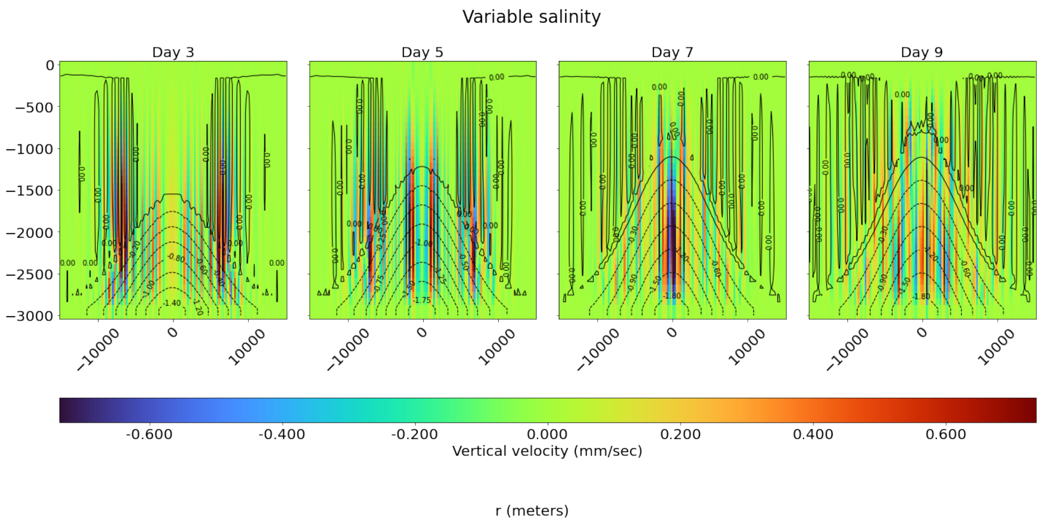

Figure 5.7: (a) Contour plots for vertical velocity plotted in (r, z)-plane and density anomaly (calculated as: density at a particular day - the initial density) contours for respective days, showing vertical movement of the plume and the corresponding density anomaly introduced in both the cases in the plume and outside the plume.

It can be observed from Figure 5.7 (a) and (b) that the horizontal extent of the plume spans approximately 5,500 meters on either side of the central axis at $r = 0$. Beyond this region, alternating upward and downward flows are visible, indicating the presence of vertical velocity gradients. These gradients arise from the accumulation of warm water at the edges of the plume [109, 108, 107], as previously discussed. The interaction between the rising warm water within the plume and the surrounding cooler water generates these vertical velocity fluctuations. These gradients manifest as alternating upward and downward flows in response to the differential buoyancy between the warm water and the cooler surrounding water, as seen in the red (upward velocity) and blue (downward velocity) bands outside the plume's core.

From Figure 5.7 (a), it is evident that for case (a) when the heat flux drops to zero on day 7, the upward flow within the plume begins to dissipate, and by day 9, the plume exhibits a fully downward motion with in the region extended approximately 5000 meters from either side of the central axis. However, warm water continues to move outward and accumulate at the edges of the plume, maintaining vertical velocity gradients, which are small. Once the heat flux ceases, the overall vertical velocity starts to decline. A maximum upward velocity of 3.39×10^{-2} mm/s and and a maximum downward velocity of 3.45×10^{-2} mm/s were recorded on day 5, while by day 9, the upward velocity decreased to 2.97×10^{-2} mm/s and downward velocity increased to 4.32×10^{-2} mm/s respectively.

From Figure 5.7 (a) and (b) , a noticeable difference can be observed in the plume structure between the two cases. In case (b), there is a distinct absence of strong upward motion within a region extending approximately 5500 meters from the central axis in both directions. This reduction in upward flow in the central area is likely caused by salinity stratification, which, as discussed in previous studies [109, 108, 107], inhibits the buoyant forces that drive vertical motion. Consequently, the central rising plume is weakened, resulting in narrower regions of upwelling and downwelling that are symmetrically positioned around $r = 0$ (see Figure 5.7 (b)). The density anomaly contours in Figure 5.7 (a) and (b) show that the region near the seabed with significant density changes is wider in Case (b) compared to Case (a). This difference is due to the surrounding water outside the plume being at 0°C in Case (b), which allows the transported hot water within the plume to accumulate toward its edges, creating a larger region with distinct density variations. In contrast, Case (a) features temperature stratification, so when hot water reaches the edge of the plume due to horizontal convection, it mixes with ambient water of similar temperature. This mixing stabilizes the temperature distribution and reduces sharp temperature gradients and density anomalies, which are much more prominent in Case (b) (see Figure 5.5(b) and 5.7(b)).

As highlighted by [109, 108], the sheet-like structure surrounding the plume gradually narrows towards the central axis ($x = 0$), intensifying the plume's instability, which is clearly visible in Figure 5.7 (b). This instability causes an increase in the velocity, as depicted in Figure 5.7 (b). Furthermore, it is worth noting that once the sheet reaches the plume's center, the flow becomes concentrated in the central region (Figure 5.7 (b)) and gradually weakens away from the plume's core.

5.3.4 Free surface elevation

Figure 5.8 illustrates the surface elevation for both cases, where the elevation is plotted along the x-axis with y set to 0 meters. The plots illustrate a clear trend where the surface elevation increases over time, peaking around day 7 for both salinity and temperature variations, before slightly decreasing by day 9. This suggests that the plume gradually builds in strength before reaching its maximum, after which it dissipates. Case with variable salinity exhibits a slower initial build-up. For example, on day 3, the surface elevation in the salinity variation case remains quite small compared to the temperature case. This suggests that salinity-driven processes have a slower impact on surface elevation compared to temperature-driven ones. In both cases, the surface elevation drops to zero at distances around 7500 meters from the plume's center. This suggests that in the deep submarine eruptions the impact of the plume is highly localized, with minimal disturbance far from the eruption site. In the case with variable temperature, the maximum surface elevation reaches approximately 1.5 cm on day 7, whereas in case with salinity stratification, the maximum elevation is lower, around 0.7 cm on day 7. The difference in elevation between the two cases can be attributed to the plume dynamics. In temperature stratified case, the plume reaches a higher height compared to salinity stratified case (see Figure 5.9 (a) and (b)) , leading to a more pronounced elevation. It should also be noted that in both the cases the plume remains submerged and does not reach the free surface. As a result, much of the energy from the deep-sea eruption is dissipated as it propagates through the water column, leading to a smaller surface elevation in both the cases. This relationship between surface elevation and the volcano's depth relative to the free surface is discussed in [111].

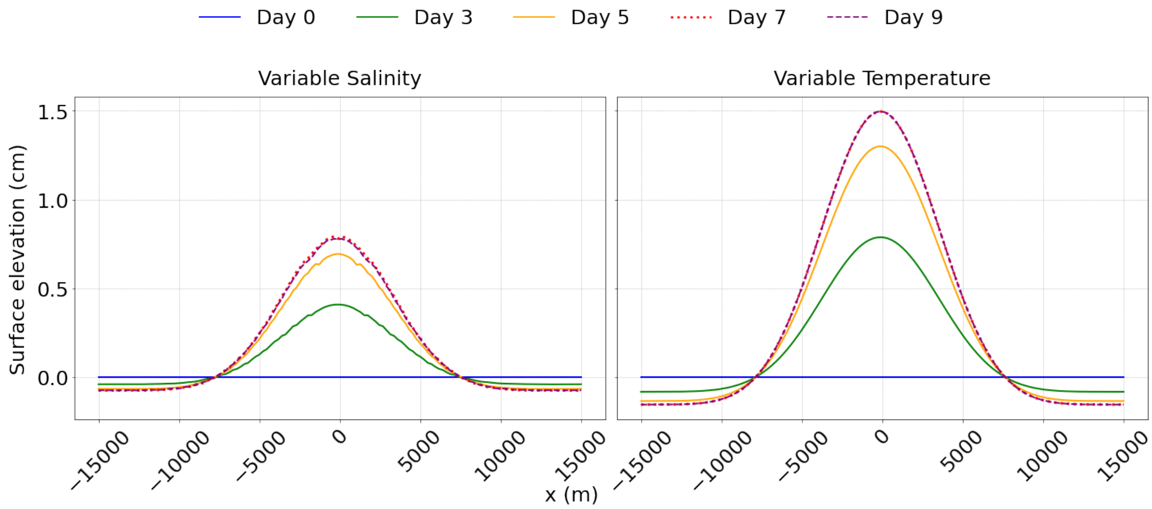

Figure 5.8: Free surface elevation plots plotted for variable x and fixed $y = 0$ meters.

5.3.5 Impact of stratification intensity on plume ascent

Figure 5.9 illustrate the temperature distribution along the depth across two primary cases and two sub-cases, capturing the vertical ascent of the plume. As described earlier, the sub-cases exhibit weak stratification, while the primary cases feature strong stratification. In Figure 5.9 (a), it is evident that in the sub-case (a) with weak stratification characterized by a temperature variations from 0°C to 4.5°C the plume reaches the free surface in 1 day and 7 hours from the start of eruption. In contrast, under strong thermal stratification, with a temperature range from 1.9°C to 16.2°C, the plume doesn't reach the free surface during the course of our simulations. While in sub-case (b), characterized by weak salinity stratification with salinity variations ranging from 34.10 ppt to 34.5 ppt, the plume reaches the free surface in 1 day and 11 hours, as shown in Figure 5.9 (b). However, in case where strong salinity stratification is present, with salinity variations between 33.07 ppt and 36.89 ppt, the plume does not reach the free surface at any point during the course of the simulations (see Figure 5.9(b)). The influence of stratification intensity on the vertical ascent of the plume has been discussed in previous studies [108].

The primary factor affecting the variations in plume behavior across these cases is the degree of stratification, whether driven by temperature or salinity, along with the resulting density gradients. In case of weak stratification, where density differences between layers are small such as a density gradient of 1.09×10^{-4} kg/m^4 in sub-cases (a) and (b) compared to 1.08×10^{-3} kg/m^4 in the two primary cases, limited temperature or salinity variations provide only slight resistance to the buoyant forces driving the plume. This allows the plume to rise more easily through the stratification, leading to a faster vertical ascent. The weaker density gradient reduces resistance, enabling the plume to move more rapidly through the water column. Conversely, in the strong stratification cases, the substantial density gradients caused by significant temperature or salinity differences create a much stronger barrier to the plume's vertical ascent. In both primary cases, strong stratification prevents the plume from reaching the surface for the entire duration of the simulations, effectively trapping it.

5.4 Remarks

This Chapter explored the dynamics of fluid flows generated by submarine volcanic eruptions, examining how temperature and salinity stratification impact flow structures in a stratified ocean environment. Through three-dimensional modeling, we observed distinct rotational, radial, and vertical flow behaviors under varying stratification conditions. Both stratified cases demonstrated a two-cell rotational structure, with cyclonic flow near the seabed and anticyclonic flow closer to the surface, consistent with previously observed patterns. Radial flows showed radially convective cells in both cases, with the temperature-stratified environment yielding more stable flows. In contrast, salinity stratification induced thermal instability over time, resulting in axially symmetric cells at the plume's periphery and chaotic flow patterns. This finding underscores the sensitivity of convective flows in salinity stratified case to thermal

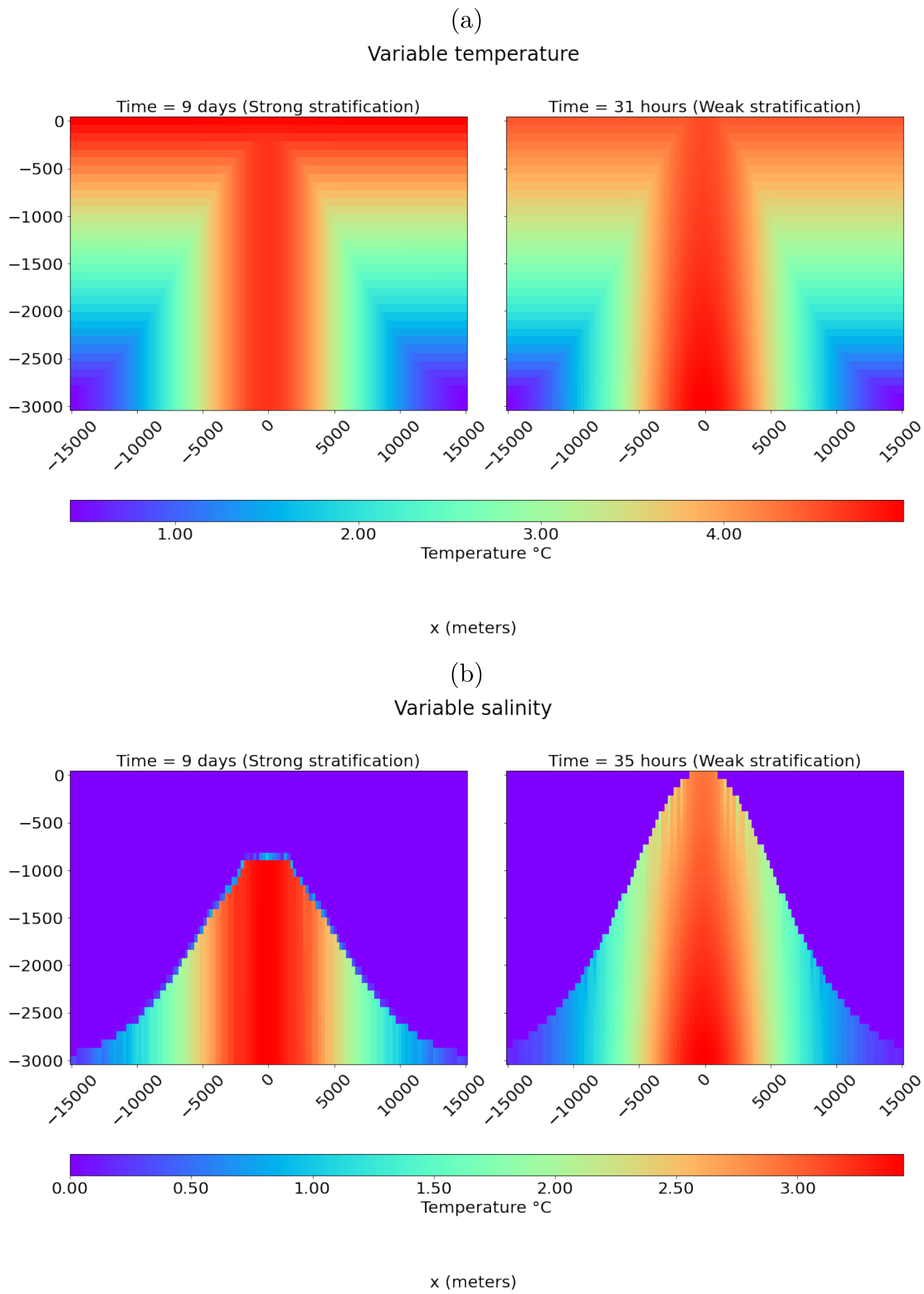

Figure 5.9: Contour plots for temperature variation in case (a) and (b) plotted in (x, z)-plane with $y = 0$ meters, showing plume is confined below the free surface in strong stratified cases but reaches the free surface with in 48 hours from the eruption.

gradients and stratification intensity.

Vertical flows showed consistent plume behavior across both stratification scenarios, with heated, buoyant water rising from the seabed. In temperature-stratified conditions, vertical velocity was initially high but decreased as the plume stabilized, while the salinity-stratified case exhibited a narrower flow due to limited buoyancy. Both cases displayed radially symmetrical vertical velocity patterns, with alternating upward and downward flows around the plume (more pronounced in the salinity case) due to interactions between warm and cool water. Stratification intensity played a crucial role: weak stratification allowed the plume to reach the surface within 48 hours, whereas strong stratification confined the plume below the surface, limiting vertical transport. Surface elevation was found to be localized, peaking around day 7 and reaching a maximum of 1.5 cm in the temperature case and 0.7 cm in the salinity case.

Overall, these findings improve our understanding of how stratified conditions affect underwater volcanic plumes, offering insights into their broader implications for ocean circulation and surface dynamics. Future studies could enhance this model by incorporating complex topographies and real-time eruption data, aiding in the prediction of subaqueous volcanic impacts and related hazards.

Chapter 6

Effect of submarine volcanic eruption on equatorial oceanic flows

In this Chapter, we develop a model inspired by the Constantin-Johnson model as the basis, incorporating the influence of the submarine volcanoes on the oceanic flows near the equator and derive analytical solutions. Unlike Chapter 5 where subsurface flows were studied using numerical modeling in two stratified cases accounting for mid and high latitudes, this Chapter focuses on the equatorial region (mid latitude). We modify the Constantin-Johnson model ([20]) to include the eruption from submarine volcanoes by considering appropriate density functions compatible with temperature variation. The solution of the governing equations is derived following a singular perturbation approach and this asymptotic technique leads to the exact results, retaining the nonlinear, three-dimensional structure of the model. Interestingly, the results also demonstrate the versatility of the fundamental Constantin-Johnson model to form the basis for other models representing several types of realistic situations.

6.1 Governing equations

We choose a coordinate system that rotates with the Earth, with $\bar{x}$ pointing due east, $\bar{y}$ due north, and $\bar{z}$ vertically upwards; see Figure 6.1 (We use over-bars to denote physical variables; these will disappear when we introduce our non-dimensional scheme). This chosen coordinate system is the one associated with the tangent plane (and therefore consistent with the β-plane approximation). The β-plane approximation adopts a local flat Cartesian coordinate sysem, while still capturing the effects of the curvature of the Earths surface. These coordinates are obtained from the original spherical coordinate system by using a two-stage manoeuvre. First, the great circle (the equator) is straightened to become the generator of a cylinder, its circular cross section now representing the interior of the sphere. The coordinate perpendicular to this, on the surface, is then be expressed as the arc length along the circular rim of the cylinder, following the circumference at a mean radius of the Earth. The coordinate $\bar{y}$ in Figure 6.1 is in the direction of the tangent at a point on the equator. This is, however, not the curvilinear coordinate which we denote by $\bar{\bar{y}}$. In typical Cartesian coordinates, the z-axis points vertically upwards from the centre of the Earth, for all points on the surface; we denote the corresponding cylindrical (radial) coordinate by $\bar{\bar{z}}$.

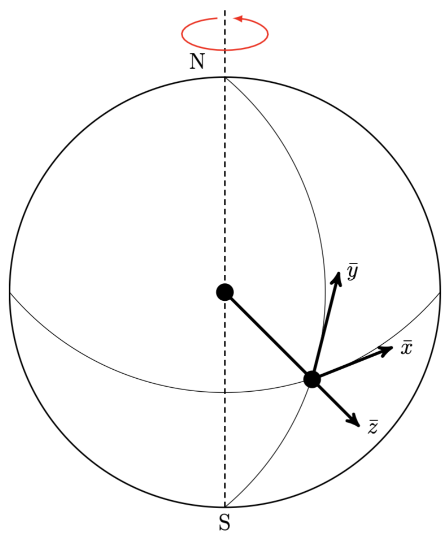

Figure 6.1: The rotating frame of reference based on tangent plane, with the $\bar{x}$ axis chosen horizontally due east, the $\bar{y}$ axis horizontally due north and the $\bar{z}$ axis vertically upward.

Governing equations (Euler and mass conservation) with spatially varying density are written as

$$\rho\frac{D\bar{\mathbf{u}}}{Dt} + 2\bar{\mathbf{\Omega}} \times (\rho\bar{\mathbf{u}}) = -\bar{\nabla}\bar{p} + \bar{\mathbf{F}},\ \ \bar{\nabla}.(\rho\bar{\mathbf{u}}) = 0 \tag{6.1}$$

where $\bar{\mathbf{u}} = (\bar{u}, \bar{v}, \bar{w})$ is the velocity of the fluid corresponding to $\bar{\mathbf{x}} = (\bar{x}, \bar{y}, \bar{z})$, $\bar{t}$ is the time (and $D/D\bar{t}$ the associated material derivative), while $\bar{p}$ and ρ are the pressure and the spatially varying density, respectively. The body force is represented by $\bar{\mathbf{F}}$ and $\bar{\mathbf{\Omega}} = \bar{\Omega}(0, \cos\theta, \sin\theta)$ is the angular-velocity vector describing the rotation of the Earth (with $|\bar{\mathbf{\Omega}}| = \bar{\Omega} \approx 7.29 \times 10^{-5} rad\, s^{-1}$ and θ the angle of latitude).

We now invoke a suitable approximation of the Coriolis term close to the equator. For small values of $\bar{\bar{y}}/\bar{R}$, where $\bar{R}$ is the average radius of the earth we write the term $2\bar{\mathbf{\Omega}} \times (\rho\bar{\mathbf{u}})$ as $2\bar{\Omega}(\bar{w} - \bar{\bar{y}}\bar{v}/\bar{R}, \bar{\bar{y}}\bar{u}/\bar{R}, -\bar{u})$, since $\sin\theta \approx \theta$ and $\cos\theta \approx 1$ for $|\theta| \ll 1$. This is in effect the β-plane approximation, which is regarded as acceptable within about 2° of the equator [78]. We therefore have $\bar{x}$ measured, equivalently, along the curvature of the equator (eastwards) and $\bar{\bar{y}}$ measured along a line of longitude (northwards). It may also be noted that with this same approximation, the curved surface of the earth drops below the $(\bar{x}, \bar{y})$-tangent-plane by an amount of $\bar{\bar{y}}^2/2\bar{R}$, approximately. This is indeed, consistent with, and a consequence of the β-plane approximation. We thus have $\bar{\bar{z}} = \bar{z} + \frac{1}{2}\bar{y}^2/\bar{R}$ and $\bar{\bar{y}} = \bar{y}$ (see [20] for more details). With this interpretation of the chosen coordinate system, the distance from the gravitational field (its negative gradient) becomes $(0, 0, -g)$. The gravity terms appear only in $\bar{\bar{z}}$-component equation.

The governing equations for a steady flow therefore become (writing $\bar{y}\, for\, \bar{\bar{y}}$)

$$\rho(\bar{u}\bar{u}_{\bar{x}} + \bar{v}\bar{u}_{\bar{y}} + \bar{w}\bar{u}_{\bar{\bar{z}}}) + 2\bar{\Omega}\rho(\bar{w} - \frac{\bar{y}}{\bar{R}}\bar{v}) = -\bar{p}_{\bar{x}} \ , \tag{6.2}$$

$$\rho(\bar{u}\bar{v}_{\bar{x}} + \bar{v}\bar{v}_{\bar{y}} + \bar{w}\bar{v}_{\bar{\bar{z}}}) + 2\bar{\Omega}\rho\frac{\bar{y}}{\bar{R}}\bar{u} = -\bar{p}_{\bar{y}} \ , \tag{6.3}$$

$$\rho(\bar{u}\bar{w}_{\bar{x}} + \bar{v}\bar{w}_{\bar{y}} + \bar{w}\bar{w}_{\bar{\bar{z}}}) - 2\bar{\Omega}\rho\bar{u} = -\bar{p}_{\bar{\bar{z}}} - \rho g, \tag{6.4}$$

and

$$(\rho\bar{u})_{\bar{x}} + (\rho\bar{v})_{\bar{y}} + (\rho\bar{w})_{\bar{\bar{z}}} = 0 \ , \tag{6.5}$$

with g as the constant acceleration due to gravity.

6.2 Modelling of density function

We now consider modelling the effect of the submarine volcano and the associated density function. We model the density function motivated by [6] considering the effect of temperature variation and volcanic ashes. We consider a hydrothermal plume generated by a heat input at the seafloor. The stem of the plume is modeled as a column of hot water that propagates vertically within the ambient density stratification of the ocean. The flow in the stem of the plume will entrain seawater, causing it to cool and eventually rise to a height where it is heavier than the seawater. Following an inertial overshoot, the flow will settle along a neutral level, forming the umbrella.

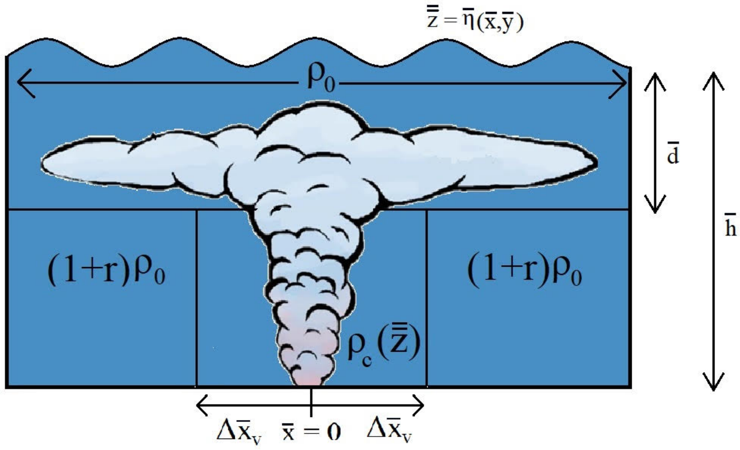

Figure 6.2: Density distribution (The hydrothermal plume forms a stem fed by lava heating and/or release of intracrustal fluid, which accumulates and cools following entrainment of ambient seawater, [6].)

We represent the variation in density by implicitly taking into account the thermodynamic influence and the effect of equation of state (see for example [6]) and hence modelling the effect of temperature variation and its impact on density. The water is warm at the bottom and colder above the stratified layer (due to the entrainment of the cold sea water), which gives rise to the inversion of density distribution i.e., lower density at the bottom and higher density at the top in the plumic region. The density of the plume eventually matches the density of the layer above the stratification where the water/tephra flows horizontally filling the umbrella. The mathematical formulation of this is presented as follows.

6.2.1 Mathematical formulation including the stem and umbrella of the plume

Let the volcano be located at $\bar{x} = 0$ on the seafloor. We also include the stratification along $\bar{\bar{z}} = \bar{T}(\bar{x}, \bar{y})$. We consider a constant density ρ_0 from $\bar{z} = \bar{T}(\bar{x}, \bar{y})$ to $\bar{\bar{z}} =$

$\bar{\eta}(\bar{x}, \bar{y})$(free surface). Due the presence of volcano there is a high temperature zone near $\bar{x} = 0$ at the seafloor and hence a lower density compared to a location at a shallow depth along $\bar{x} = 0$. This zone is assumed to have a width of $2\Delta\bar{x}_v$ representing the vertical plume until the level of the horizontal umbrella is reached. We assume the length of the volcano to be sufficiently large alonng the $\bar{y}$ axis as compared to the width of the volcano $2\Delta\bar{x}_v$. A cross-section in the $(\bar{x}, \bar{\bar{v}})$ plane is shown in Figure: 6.2. As we move up vertically from the sea-bed to $\bar{\bar{z}} = \bar{T}(\bar{x}, \bar{y})$ (along which there is a horizontal spread of the volcanic ashes/materials (see Figure 3.2)), the density increases linearly in the stem region of width $2\Delta\bar{x}_v$, due to the entrainment of the seawater in the stem of the vertical plume from either side of $\bar{x}$ axis. Outside the vertical stem of width $2\Delta\bar{x}_v$, we have a region of constant density $(1 + r)\rho_0$ (where r is a small scalar constant) bounded by the sea bed at the bottom and $\bar{\bar{z}} = \bar{T}(\bar{x}, \bar{y})$ at the top. In the top stratified layer, the density is assumed to have a uniform value of ρ_0. Also, we assume a linear variation of density on either side of the central vertical plane $\bar{x} = 0$ along the horizontal line $-\Delta\bar{x}_v \leq \bar{x} \leq \Delta\bar{x}_v$, within the stem of vertical plume for any given value of $\bar{z}$ between the seafloor and $\bar{\bar{z}} = \bar{T}(\bar{x}, \bar{y})$. Further, the density along the length of the volcano i.e., along the $\bar{y}$ axis in the plumic region of width $2\Delta\bar{x}_v$ is assumed to be constant. Hence, the general expression for the density below the stratified layer is expressed as

$$\rho(\bar{x}, \bar{\bar{z}}) = \rho_0\Bigg(\left(1 - \alpha\frac{\bar{\bar{z}} + \bar{d}}{\bar{d} - \bar{h}}\right) + \left((r + \alpha\frac{\bar{\bar{z}} + \bar{d}}{\bar{d} - \bar{h}})\frac{|\bar{x}|}{\Delta\bar{x}_v}\right)\Bigg),$$

where $0 \leq \alpha < 1$ is a scalar, and $\bar{d}$ and $\bar{h}$ are the distances of the stratified layer and the free surface respectively measured from the line $\bar{x} = 0$ on the sea-bed.

The vertical variation of the density in the plane $\bar{x} = 0$ in the layer below the stratification is thus given by $\rho_c(\bar{\bar{z}}) = \rho(0, \bar{\bar{z}}) = \left(1 - \alpha\frac{\bar{\bar{z}}+\bar{d}}{\bar{d}-\bar{h}}\right)\rho_0$.

We will first deal with the part in which we have variable density i.e., we first solve our system with sea bed $\bar{\bar{z}} = -\bar{H}(\bar{x}, \bar{y})$ and $\bar{\bar{z}} = \bar{T}(\bar{x}, \bar{y})$ as boundaries and consider the plume of vertical width $\Delta\bar{x}_v$ symmetrically located around $\bar{x} = 0$.

Boundary conditions that we require are

$$\bar{p} = \bar{P}_T(\bar{x}, \bar{y});\ \bar{w} = \bar{u}\bar{T}_{\bar{x}} + \bar{v}\bar{T}_{\bar{y}}\ on\ \bar{\bar{z}} = \bar{T}(\bar{x}, \bar{y}) \tag{6.6}$$

and

$$\bar{w} = \bar{u}\bar{H}_{\bar{x}} + \bar{v}\bar{H}_{\bar{y}}\ on\ \bar{\bar{z}} = \bar{H}(\bar{x}, \bar{y})\ . \tag{6.7}$$

6.3 Non-dimensionalization of equations

We now recast the governing equations in a suitable form by introducing non- dimensionalization of the variables so that we can carry out an asymptotic analysis. We will use the terminology used in ([20]) for simplification and non-dimensionalization of the equations. We consider the value of density on the right-hand side of the volcano (similar calculations will follow for the region on the left).

We use the following non-dimensionalization of the variables

$$\bar{\mathbf{x}} = (\bar{x}, \bar{y}, \bar{\bar{z}}) = (\bar{L}x, \bar{l}y, \bar{h}z),$$

$$\bar{\mathbf{u}} = (\bar{u}, \bar{v}, \bar{w}) = \bar{U}(u, \bar{l}v/\bar{L}, \bar{h}w/\bar{L})$$

$$\bar{p} = \rho_0 \bar{U}^2 p$$

where the length scales are $(\bar{L}, \bar{l}, \bar{h})$ and $\bar{U}$ is an appropriate speed scale. The velocity components have been non-dimensionalised in a form that guarantees the existence of a stream function, via a balance of terms of equal size, irrespective of whether the flow is in the (x, z) or (y, z) frame.
Normalizing with respect to ρ_o (6.2) - (6.5) become

$$\begin{aligned}&\left(1 - \alpha\left(\frac{z+d}{d-1}\right) + \left(r + \alpha\left(\frac{z+d}{d-1}\right)\right)\frac{x}{\Delta x_v}\right)(uu_x + vu_y + wu_z) + \\ &\quad 2\bar{\Omega}\frac{\bar{h}}{\bar{U}}\left(1 - \alpha\left(\frac{z+d}{d-1}\right) + \left(r + \alpha\left(\frac{z+d}{d-1}\right)\right)\left(\frac{x}{\Delta x_v}\right)\right)(w - \frac{\bar{l}^2}{\bar{R}\bar{h}}yv) = -p_x\ ,\end{aligned} \tag{6.8}$$

$$\frac{\bar{l}^2}{\bar{L}^2}\left(1-\alpha\left(\frac{z+d}{d-1}\right)+\left(r+\alpha\left(\frac{z+d}{d-1}\right)\right)\frac{x}{\Delta x_v}\right)(uv_x+vv_y+wv_z)+$$
$$2\bar{\Omega}\frac{\bar{l}^2}{\bar{U}\bar{R}}\left(1-\alpha\left(\frac{z+d}{d-1}\right)+\left(r+\alpha\left(\frac{z+d}{d-1}\right)\right)\frac{x}{\Delta x_v}\right)yu=-p_y\ , \tag{6.9}$$

$$\frac{\bar{h}^2}{\bar{L}^2}\left(1-\alpha\left(\frac{z+d}{d-1}\right)+\left(r+\alpha\left(\frac{z+d}{d-1}\right)\right)\frac{x}{\Delta x_v}\right)(uw_x+vw_y+ww_z)-$$
$$2\bar{\Omega}\frac{\bar{h}}{\bar{U}}\left(1-\alpha\left(\frac{z+d}{d-1}\right)+\left(r+\alpha\left(\frac{z+d}{d-1}\right)\right)\frac{x}{\Delta x_v}\right)u$$
$$=-p_z-\frac{\bar{h}}{\bar{U}^2}\left(1-\alpha\left(\frac{z+d}{d-1}\right)+\left(r+\alpha\left(\frac{z+d}{d-1}\right)\right)\frac{x}{\Delta x_v}\right)g\ , \tag{6.10}$$

$$\left(1-\alpha\left(\frac{z+d}{d-1}\right)+\left(r+\alpha\left(\frac{z+d}{d-1}\right)\right)\frac{x}{\Delta x_v}\right)(u_x+v_y+w_z)+$$
$$\left(r+\alpha\left(\frac{z+d}{d-1}\right)\right)\frac{u}{\Delta x_v}+\frac{\alpha}{d-1}\left(\frac{x}{\Delta x_v}-1\right)w=0 \tag{6.11}$$

with the boundary condition

$$p=\bar{P}_T(\bar{x},\bar{y})/(\rho_0\bar{U}^2)=P_0(x,y,z);\ w=uT_x+vT_y \text{ on } z=T(x,y) \tag{6.12}$$

and

$$w=uH_x+vH_y \text{ on } z=H(x,y) \tag{6.13}$$

where $d=\bar{d}/\bar{h}$ and $\Delta x_v=\bar{\Delta x}_v/\bar{L}$.

We redefine the pressure so that the pressure is expressed relative to the ambient hydrostatic pressure. We write it as

$$P(x,y,z)=p(x,y,z)+\frac{g\bar{h}}{\bar{U}^2}z\left(1-\alpha\left(\frac{z/2+d}{d-1}\right)+\left(r+\alpha\left(\frac{z/2+d}{d-1}\right)\right)\frac{x}{\Delta x_v}\right)\ . \tag{6.14}$$

Next, we set $\bar{l}=\sqrt{\bar{R}\bar{h}}$, $\frac{\bar{\Omega}\bar{h}}{\bar{U}}=\omega$. With this choice of $\bar{l}$ we invoke the limiting process described as $(\bar{h}/\bar{L})^2\to 0$ with $(\bar{l}/\bar{L})^2=(\bar{l}/\bar{h})^2(\bar{h}/\bar{L})^2\to 0$ and all other parameters fixed. The governing equations (6.8) - (6.11) therefore take the form

$$\left(1-\alpha\left(\frac{z+d}{d-1}\right)+\left(r+\alpha\left(\frac{z+d}{d-1}\right)\right)\frac{x}{\Delta x_v}\right)(uu_x+vu_y+wu_z)+$$
$$2\omega\left(1-\alpha\left(\frac{z+d}{d-1}\right)+\left(r+\alpha\left(\frac{z+d}{d-1}\right)\right)\frac{x}{\Delta x_v}\right)(w-yv)$$
$$=-P_x+\frac{zg\bar{h}}{\bar{U}^2\Delta x_v}\left(r+\alpha\left(\frac{z/2+d}{d-1}\right)\right)\ , \quad (6.15)$$

$$2\omega\left(1-\alpha\left(\frac{z+d}{d-1}\right)+\left(r+\alpha\left(\frac{z+d}{d-1}\right)\right)\frac{x}{\Delta x_v}\right)yu=-P_y\ , \quad (6.16)$$

$$2\omega\left(1-\alpha\left(\frac{z+d}{d-1}\right)+\left(r+\alpha\left(\frac{z+d}{d-1}\right)\right)\frac{x}{\Delta x_v}\right)u=P_z\ , \quad (6.17)$$

$$\left(1-\alpha\left(\frac{z+d}{d-1}\right)+\left(r+\alpha\left(\frac{z+d}{d-1}\right)\right)\frac{x}{\Delta x_v}\right)(u_x+v_y+w_z)+$$
$$\left(r+\alpha\left(\frac{z+d}{d-1}\right)\right)\frac{u}{\Delta w_v}+\frac{\alpha}{d-1}\left(\frac{x}{\Delta x_v}-1\right)w=0 \quad (6.18)$$

with the boundary conditions

$$P(x,y,z)=P_0(x,y,z)+T(x,y)\kappa(x,T(x,y));\ w=uT_x+vT_y \text{ on } z=T(x,y) \quad (6.19)$$

and

$$w=uH_x+vH_y \text{ on } z=H(x,y) \quad (6.20)$$

where

$$\kappa(x,T(x,y))=\frac{g\bar{h}}{\bar{U}^2}\left(1-\alpha\left(\frac{T(x,y)/2+d}{d-1}\right)+\left(r+\alpha\left(\frac{T(x,y)/2+d}{d-1}\right)\right)\frac{x}{\Delta x_v}\right).$$

It may be noted that on the right hand side in (6.15) an additional terms appears which modifies the pressure gradient and is caused due to the influence of the volcanic eruption.

6.4 Form of pressure function

Let us introduce

$$u(x, z - \frac{1}{2}y^2) = \phi_\zeta(x, z - \frac{1}{2}y^2) \text{ with } \zeta = z - \frac{1}{2}y^2$$

and

$$u(x, z - \frac{1}{2}y^2)\left(1 - \alpha\left(\frac{z+d}{d-1}\right) + \left(r + \alpha\left(\frac{z+d}{d-1}\right)\right)\frac{x}{\Delta x_v}\right) = \bar{\phi}_\zeta(x, z - \frac{1}{2}y^2, z)$$

leading to

$$P_y = -2\omega\bar{\phi}_\zeta y \ ,$$

$$P_z = 2\omega\bar{\phi}_\zeta \ .$$

We then have

$$P(x, y, z) = A(x) + 2\omega\bar{\phi}(x, z - \frac{1}{2}y^2, z) \tag{6.21}$$

where, $A(x)$ is an arbitraty function. Once u is prescribed, one can then determine ϕ and then $\bar{\phi}$. For convenience, we define $\phi(x, 0, \frac{1}{2}y^2) = 0$ which implies $\bar{\phi}(x, 0, \frac{1}{2}y^2) = 0$ if $u \neq 0$ at $z = \frac{1}{2}y^2$.

We now investigate pressure boundary condition in more detail. We first describe the boundary condition $z = T(x, y)$ relative to the tangent plane by setting

$$T(x, y) = \frac{1}{2}y^2 - \nu(x, y) \tag{6.22}$$

leading to the pressure on $z = T(x, y)$ as

$$P_0(x, y) = A(x) - \Big\{\frac{1}{2}y^2 - \nu(x, y)\Big\}\kappa\left(x, \frac{1}{2}y^2 - \nu(x, y)\right) + 2\omega\bar{\phi}(x, -\nu(x, y), T(x, y)) \tag{6.23}$$

where $\nu(x, y)$ is a scalar function of x and y.

6.5 Simplification of the model

Since the surface $z = T(x, y)$ is identified with a plane parallel to the tangent plane (and so follows the curvature in y direction), no further dependence on y is assumed, i.e. $\nu(x, y) = \nu(x)$. Also, this surface doesn't evolve significantly in x-direction and hence we remove the dependence on x, we have $\nu(x) = 0$. Pressure at $z = T(x, y)$ becomes

$$P_0(x, y) = A(x) - \left\{\frac{1}{2}y^2\right\}\kappa(x, \frac{1}{2}y^2) \ . \tag{6.24}$$

We also invoke the condition of constant pressure along $y = 0$ leading to $A(x) =$ constant.

The base of the ocean is identified with the plane parallel to the tangent plane (and so follows the curvature in y-direction), but we consider the dependence on x due the presence of volcano. Thus, we choose to set

$$z = H(x, y) = \frac{1}{2}y^2 - N(x) \ . \tag{6.25}$$

Therefore, our system now becomes

$$\begin{aligned}\left(1 - \alpha\left(\frac{z+d}{d-1}\right) + \left(r + \alpha\left(\frac{z+d}{d-1}\right)\right)\left(\frac{x}{\Delta x_v}\right)\right)(uu_x + vu_y + wu_z) + \\ 2\omega\left(1 - \alpha\left(\frac{z+d}{d-1}\right) + \left(r + \alpha\left(\frac{z+d}{d-1}\right)\right)\frac{x}{\Delta x_v}\right)(w - yv) \\ = -2\omega\bar{\phi}_x + \frac{zg\bar{h}}{\bar{U}^2\Delta x_v}\left(r + \alpha\left(\frac{z/2+d}{d-1}\right)\right)\end{aligned} \tag{6.26}$$

and

$$\begin{aligned}\left(1 - \alpha\left(\frac{z+d}{d-1}\right) + \left(r + \alpha\left(\frac{z+d}{d-1}\right)\right)\frac{x}{\Delta x_v}\right)(u_x + v_y + w_z) + \\ \left(r + \alpha\left(\frac{z+d}{d-1}\right)\right)\frac{u}{\Delta x_v} + \frac{\alpha}{d-1}\left(\frac{x}{\Delta x_v} - 1\right)w = 0\end{aligned} \tag{6.27}$$

with

$$w = yv \ on \ z = \frac{1}{2}y^2; \ w + uN' - vy = 0 \text{ on } z = -N(x) + \frac{1}{2}y^2 \ ; \tag{6.28}$$

where prime denotes the derivative with respect to x, and u is assumed given as a function of z on $y = 0$, and is therefore known across the (z, y) plane.

6.6 Method of solution

Due to the presence of the volcano there is a density difference which has an impact on the flow. Hence, there is a non-zero velocity between $z = T(x, y)$ and the sea-bed in the plumic stem region, and we consider a zero velocity at the bed (i.e. the layer of fluid just above the sea-bed is stationary).

Since $\phi(x, 0, \frac{1}{2}y^2) = 0$, we conclude that

$$\phi(x, \zeta) = -\int_{\zeta}^{0} u(x, \zeta')d\zeta' \text{ for } \zeta < 0 \tag{6.29}$$

and on using equation (6.27) in (6.26) we have

$$\begin{aligned}\left(1 - \alpha\left(\frac{z+d}{d-1}\right) + \left(r + \alpha\left(\frac{z+d}{d-1}\right)\right)\frac{x}{\Delta x_v}\right)(vu_y + wu_z - uv_y - uw_z) \\ + 2\omega\left(1 - \alpha\left(\frac{z+d}{d-1}\right) + \left(r + \alpha\left(\frac{z+d}{d-1}\right)\right)\frac{x}{\Delta x_v}\right)(w - yv) - \\ \frac{\alpha}{d-1}\left(\frac{x}{\Delta x_v} - 1\right)wu = -2\omega\bar{\phi}_x + \frac{zg\bar{h}}{\bar{U}^2\Delta x_v}\left(r + \alpha\left(\frac{z/2+d}{d-1}\right)\right) + \\ \left(r + \alpha\left(\frac{z+d}{d-1}\right)\right)\frac{u^2}{\Delta x_v}\end{aligned} \tag{6.30}$$

which will become

$$\left\{\frac{v}{u}E\right\}_y + \left\{\frac{w}{u}E\right\}_z = \frac{E}{u^2}\frac{2\omega\bar{\phi}_x - \frac{zg\bar{h}}{\bar{U}^2\Delta x_v}\left(r + \alpha\left(\frac{z/2+d}{d-1}\right)\right) - \left(r + \alpha\left(\frac{z+d}{d-1}\right)\right)\frac{u^2}{\Delta x_v}}{\left(1 - \alpha\left(\frac{z+d}{d-1}\right) + \left(r + \alpha\left(\frac{z+d}{d-1}\right)\right)\frac{x}{\Delta x_v}\right)} \tag{6.31}$$

where

$$E = \frac{\exp\left(2\omega\int_{\zeta}^{0}\frac{d\zeta'}{u(x,\zeta')}\right)}{\left(1 - \alpha\left(\frac{z+d}{d-1}\right) + \left(r + \alpha\left(\frac{z+d}{d-1}\right)\right)\frac{x}{\Delta x_v}\right)} \text{ with } \zeta = z - \frac{1}{2}y^2 \tag{6.32}$$

and

$$\bar{\phi}(x,y,\zeta) = \\ -\int_{\zeta}^{0} u(x,\zeta')\left(1-\alpha\left(\frac{\zeta'+\frac{1}{2}y^2+d}{d-1}\right)+\left(r+\alpha\left(\frac{\zeta'+\frac{1}{2}y^2+d}{d-1}\right)\right)\frac{x}{\Delta x_v}\right)d\zeta' \\ \zeta < 0 \ .$$

We now introduce a quasi-stream-function and set

$$\frac{v(x,y,z)}{u(x,y,z)}E(x,z-\frac{1}{2}y^2) = \Psi_z \ . \tag{6.33}$$

Integrating (6.31) with respect to z we have

$$\Psi_y + \frac{w}{u}E = -\hat{I} \tag{6.34}$$

where

$$\hat{I}(x,y,z) = \\ \int_z^{1/2y^2} \frac{2\omega\bar{\phi}_x(x,z'-\frac{1}{2}y^2) - \frac{z'g\bar{h}}{\bar{U}^2\Delta x_v}\left(r+\alpha\left(\frac{z'/2+d}{d-1}\right)\right) - \left(r+\alpha\left(\frac{z'+d}{d-1}\right)\right)\frac{u^2}{\Delta x_v}}{\left(1-\alpha\left(\frac{z'+d}{d-1}\right)+\left(r+\alpha\left(\frac{z'+d}{d-1}\right)\right)\frac{x}{\Delta x_v}\right)}\frac{E}{u^2}dz' \ . \tag{6.35}$$

Expressions for v and w now becomes

$$v = \frac{u}{E}\Psi_z \text{ and } w = -\frac{u}{E}(\Psi_y + \hat{I}) \text{ with } u = u(x,\zeta) \ . \tag{6.36}$$

We can write (6.26) as

$$\left(1-\alpha\left(\frac{z+d}{d-1}\right)+\left(r+\alpha\left(\frac{z+d}{d-1}\right)\right)\frac{x}{\Delta x_v}\right)(u_x - \frac{yu_\zeta}{E}\Psi_z - \frac{u_\zeta}{E}(\Psi_y+\hat{I})) - \\ 2\omega\left(1-\alpha\left(\frac{z+d}{d-1}\right)+\left(r+\alpha\left(\frac{z+d}{d-1}\right)\right)\frac{x}{\Delta x_v}\right)(\frac{\Psi_y+\hat{I}}{E}+\frac{y\Psi_z}{E}) \\ = \frac{-2\omega\bar{\phi}_x + \frac{zg\bar{h}}{\bar{U}^2\Delta x_v}\left(r+\alpha\left(\frac{z/2+d}{d-1}\right)\right)}{u} \tag{6.37}$$

which gives

$$
\begin{aligned}
&-\left(\frac{\left(1-\alpha\left(\frac{z+d}{d-1}\right)+\left(r+\alpha\left(\frac{z+d}{d-1}\right)\right)\frac{x}{\Delta x_v}\right)(yu_\zeta+2\omega y)}{E}\right)\Psi_z- \\
&\qquad\left(\frac{\left(1-\alpha\left(\frac{z+d}{d-1}\right)+\left(r+\alpha\left(\frac{z+d}{d-1}\right)\right)\frac{x}{\Delta x_v}\right)(u_\zeta+2\omega)}{E}\right)\Psi_y = \\
&\qquad\qquad\frac{-2\omega\bar{\phi}_x+\frac{zg\bar{h}}{\bar{U}^2\Delta x_v}\left(r+\alpha\left(\frac{z/2+d}{d-1}\right)\right)}{u}- \\
&\qquad\left(1-\alpha\left(\frac{z+d}{d-1}\right)+\left(r+\alpha\left(\frac{z+d}{d-1}\right)\right)\left(\frac{x}{\Delta x_v}\right)\right)u_x+ \\
&\qquad\left(1-\alpha\left(\frac{z+d}{d-1}\right)+\left(r+\alpha\left(\frac{z+d}{d-1}\right)\right)\left(\frac{x}{\Delta x_v}\right)\right)\left(\frac{u_\zeta+2\omega}{E}\right)\hat{I}\ .
\end{aligned}
\tag{6.38}
$$

Let us define

$$
F(x,\zeta,z) = -\frac{\left(1-\alpha\left(\frac{z+d}{d-1}\right)+\left(r+\alpha\left(\frac{z+d}{d-1}\right)\right)\frac{x}{\Delta x_v}\right)(u_\zeta+2\omega)}{E}\ . \tag{6.39}
$$

Then from (6.38), we have

$$
y\Psi_z+\Psi_y = G(x,\zeta,z)/F(x,\zeta,z) \tag{6.40}
$$

with

$$
\begin{aligned}
G(x,\zeta,z) = &\frac{-2\omega\bar{\phi}_x+\frac{zg\bar{h}}{\bar{U}^2\Delta x_v}\left(r+\alpha\left(\frac{z/2+d}{d-1}\right)\right)}{u}- \\
&\left(1-\alpha\left(\frac{z+d}{d-1}\right)+\left(r+\alpha\left(\frac{z+d}{d-1}\right)\right)\frac{x}{\Delta x_v}\right)u_x+ \\
&\left(1-\alpha\left(\frac{z+d}{d-1}\right)+\left(r+\alpha\left(\frac{z+d}{d-1}\right)\right)\left(\frac{x}{\Delta x_v}\right)\right)\left(\frac{u_\zeta+2\omega}{E}\right)I
\end{aligned}
\tag{6.41}
$$

where

$$
\begin{aligned}
&I(x,\zeta,z) = \\
&\int_\zeta^0 \frac{2\omega\bar{\phi}_x(x,\zeta')-\frac{(\zeta'+\frac{1}{2}y^2)g\bar{h}}{\bar{U}^2\Delta x_v}\left(r+\alpha\left(\frac{\zeta'/2+\frac{1}{4}y^2+d}{d-1}\right)\right)-\left(r+\alpha\left(\frac{\zeta'+\frac{1}{2}y^2+d}{d-1}\right)\right)\frac{u^2}{\Delta x_v}}{\left(1-\alpha\left(\frac{\zeta'+\frac{1}{2}y^2+d}{d-1}\right)+\left(r+\alpha\left(\frac{\zeta'+\frac{1}{2}y^2+d}{d-1}\right)\right)\left(\frac{x}{\Delta x_v}\right)\right)}\frac{E}{u^2}d\zeta\ .
\end{aligned}
\tag{6.42}
$$

We now find the characteristic curves for the solutions of (6.40) from the following

$$\frac{dz}{y} = \frac{dy}{1} = \frac{d\Psi}{G(x, \zeta, z)/F(x, \zeta, z)} \ . \tag{6.43}$$

The trajectories of the characteristic curve are given by the differential equation

$$y\frac{dy}{dz} = 1 \ . \tag{6.44}$$

Thus, the characteristic curves take the form

$$z - \frac{1}{2}y^2 = C \tag{6.45}$$

where C is an arbitrary constant. Noting the form of the characteristics of the solution of (6.40), we define a function

$$\xi(y, z) = z - \frac{1}{2}y^2 \ . \tag{6.46}$$

Let us seek a solution for Ψ in (6.40) of the form

$$\Psi(x, y, z) = y\bar{\psi}(x, \xi(y, z)) \ . \tag{6.47}$$

This is consistent with the fact that the velocity v along $y = 0$ should be zero (for symmetry). Therefore, we have

$$\Psi_y = \bar{\psi} - y^2\bar{\psi}_\xi \quad \text{and} \quad \Psi_z = y\bar{\psi}_\xi \ . \tag{6.48}$$

Expressions in (6.48) when substituted in (6.40), gives

$$\bar{\psi} = \frac{G}{F} \tag{6.49}$$

leading to

$$\Psi(x, y, z) = y\frac{G}{F} \ . \tag{6.50}$$

Substituting the value of Ψ in v and w, we have

$$v = \frac{uy}{E}\left(\frac{FG_\zeta - GF_\zeta}{F^2}\right) \tag{6.51}$$

and

$$w = \frac{-u}{E}\left(\frac{G}{F} - \frac{y^2 G_\zeta}{F} + \frac{y^2 G F_\zeta}{F^2} + \hat{I}\right) . \tag{6.52}$$

6.7 Example of a velocity profile

First, we present a possible example for the velocity profile for the classical flow of undercurrents. We describe the free surface $z = \eta(x, y)$ relative to the tangent plane and set

$$z = \eta(x, y) = \frac{1}{2}y^2 + \sigma(x, y) .$$

Free surface is identified with the plane parallel to the tangent plane (and so follows the curvature in the y- direction), but we consider the dependence on x due to the presence of the volcano. Thus, we choose to set

$$z = \frac{1}{2}y^2 + \sigma(x);\ \zeta = \sigma(x) .$$

The profile we consider is one of the classical profiles given in ([20]) for the flow of undercurrents. The velocity is given by a quadratic-quartic profile as

$$u_c(x, \zeta) = \begin{cases} U(x) - \gamma(x)\zeta^2 - \delta(x)\zeta^4, & \sigma(x) \geq \zeta \geq -\mu(x) \\ 0, & -\mu(x) > \zeta \end{cases}$$

with

$$\mu(x) = \sqrt{\frac{-\gamma + \sqrt{\gamma^2 + 4\delta U}}{2\delta}} ,$$

where the simplest pair of rational powers (quadratic and quartic) are used. We assume $U > 0, \gamma > 0, \delta > 0$ and $\mu > 0$. The quadratic-quartic structure here describe the whole profile down to a zero speed, and then stagnant (stationary) conditions below that. (There is another zero, of course, near to the surface, where switch from westwards to eastwards. The maximum azimuthal speed is at $\zeta = 0$ and most of the observed data indicate that the thermocline is situated above the line of maximum azimuthal speed (see [20] for more details).

The speed of the spread of tephra (~ 0.14 m/s [6]) in the layer above the stratification is much higher then the current speed usually observed (typically <0.6 cm/s) ([6]). This is indicative of additional horizontal flow in the umbrella region of the plume due to volcanic flow. Hence, an additional flow velocity symmetrical about a point (in the umbrella region) vertically corresponding to the origin of the volcano, needs to be added to the equatorial undercurrent profile and the modified undercurrent profile is thus given by

$$u(x,\zeta) = \begin{cases} u_c(x,\zeta) + u_{um} \;, & \zeta \geq 0 \\ u_c(x,\zeta) \;, & \text{otherwise} \end{cases}$$

where, $u_{um} = U_{um}$ if $x \geq 0$ and $u_{um} = -U_{um}$ if $x < 0$. The term U_{um} is a positive scalar representing the speed of the flow of the water/ash in the umbrella fed from the vertical stem of the plume.

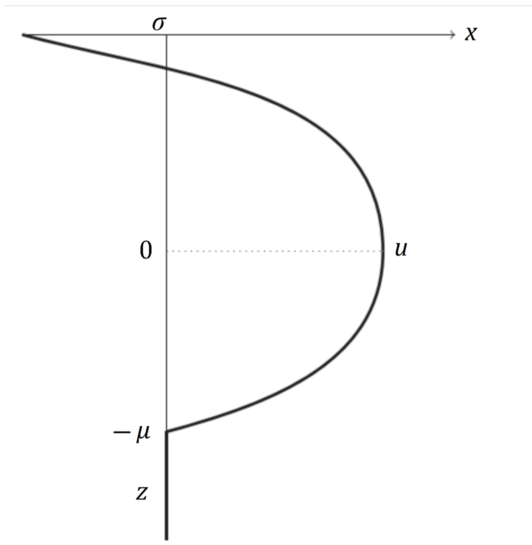

Figure 6.3: An example of a quadratic-quartic profile, with zero conditions deeper down.

6.8 Remarks

The model proposed in this chapter shows that the flow velocities of the undercurrents are influenced by parameters associated with the submarine volcanic eruptions such as the width of the vertical buoyant plume containing the ashes (related to Δx_v) and the temperature gradient along the vertical direction in the plume (related to α). It may be observed that when $\alpha \to 0$ and $\Delta x_v \to \infty$ we recover the original Constantin-Johnson model for the oceanic flows. Also, at the two vertical boundaries of the zone containing volcanic ashes/materials, as $x \to \pm\Delta x_v$ the solution for the flow velocities match the classical solutions from the Constantin-Johnson model. It is also worth pointing out that there is a singularity in the solution when $u_\zeta + 2\omega = 0$. However, this singularity appeared in the solutions in the Constantin-Johnson model too and similar treatment can be pursued. It can also be noted from equations (6.51) and (6.52) that the change in horizontal flow velocity will also affect the velocities in the vertical direction.

Chapter 7

Surface waves generated by submarine volcanic eruption in a stratified ocean

In this Chapter, we develop an analytical model by introducing the ambient stratification in the ocean to study the surface waves generated by sub-aquatic volcanic eruption, unlike Chapter 5 and 6 where the focus was to study the subsurface flows. The developed equations with the initial and boundary conditions were linearized. The linearized equations were solved using joint Laplace and Hankel transform Green's function method. The solutions were computed and the surface elevation was obtained for an instantaneous Duffy source function revealing a beating phenomenon in stratified ocean.

7.1 Model formulation

7.1.1 Governing equations

We express the following hydrodynamic model for conservation equation written in terms of the potential function ϕ with volcanic excitation as

$$\triangle\phi^* = -2q^*(t^*)\frac{\delta(r^*)\delta(z^* - z_0^*)}{r^*\rho} \tag{7.1}$$

where $\triangle$ denotes the Laplace operator in cylindrical coordinate, t^* is the time, z^* is the vertical coordinate (positive upwards), r^* is the radial coordinate, ρ denotes the density, $\delta(\cdot)$ denotes the Dirac delta function and $q^*(t^*)$ is the volcanic excitation source strength as a function of time t^* (see Figure 7.1 for schematic of the system). A formulation of volcanic eruption without stratification in the ocean can be found in [61].

While the domain under consideration has complex shape (that contains free surface and uneven bottom), we concentrate on the problem with cylindrical symmetry and with the ocean depth independent of horizontal coordinates. As shown by Pelinovskij [38], the method of wave ray tubes can also be used for tsunami waves. Within the ray the variation of bottom depth in the direction orthogonal to ray can be ignored, and the main evolutionary effect comes from ray divergence, which is similar to one taking place in the model with cylindrical symmetry.

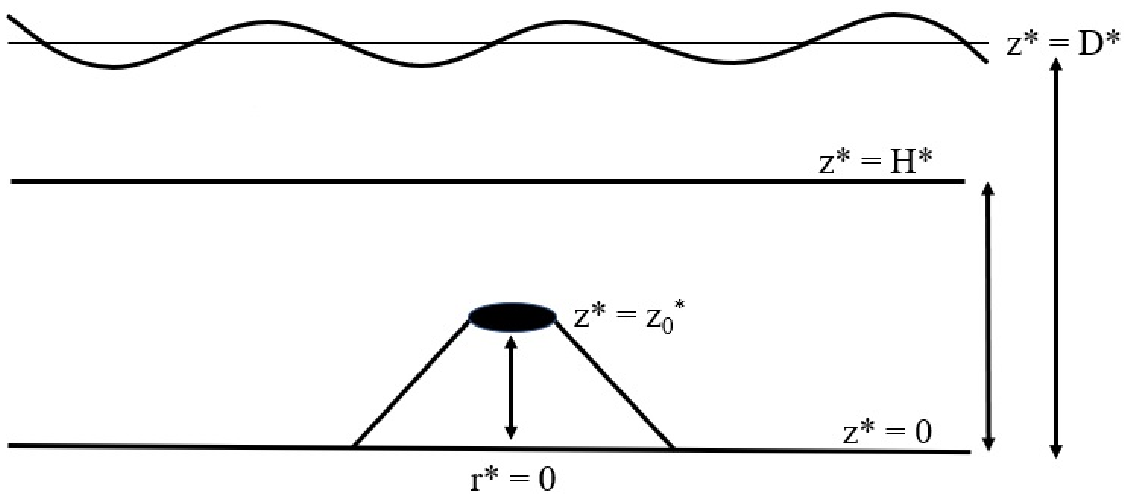

Figure 7.1: Schematic of sub-aquatic volcano, with z^* as the vertical coordinate (positive upwards) and r^* as the radial coordinate. Volcano is located at the point $(0, z_0^*)$ with stratified layer at $z^* = H^*$, free surface at $z^* = D^*$ and seabed is at $z^* = 0$. The volcano has a vent size r_0^*.

The seabed is described by the surface $z^* = 0$, while the unperturbed free surface of water is given by $z^* = \eta^*(r^*, t^*)$ at $z^* = D^*$. We denote the stratified layer by $z^* = \beta^*(r^*, t^*)$ at $z^* = H^*$. The coordinate r^* is the horizontal distance from the crater center (refer to Figure 7.1), and due to the assumed radial symmetry the angular variable does not enter the equations, and thus can be omitted. Potential function in the top and the bottom stratified layer are denoted by ϕ_1^* and ϕ_2^* respectively.

Boundary conditions at the free surface are typically nonlinear [112]. For the potential function the kinematic and dynamic boundary conditions on the free surface are given as

$$\frac{\partial \phi_1^*}{\partial z^*} = \frac{\partial \eta^*}{\partial t^*} + \frac{\partial \phi_1^*}{\partial r^*}\frac{\partial \eta^*}{\partial r^*} \text{ on } z^* = \eta^*(r^*, t^*) \tag{7.2}$$

$$\frac{\partial \phi_1^*}{\partial t^*} = -\frac{1}{2}(\nabla \phi_1^*)^2 - g\eta^* \text{ on } z^* = \eta^*(r^*, t^*) \tag{7.3}$$

respectively, where $\eta^*(r^*, t^*)$ is the free surface and g is the acceleration due to gravity. For a substantial eruption, i.e., when the ratio of wave height to the ocean depth near the crater is not small, the use of nonlinear boundary conditions becomes important. However, in our case as the surface elevation is small compared to the water depth from the volcanic source, we may ignore the nonlinear terms. Hence, we use the following linearized condition on the free surface [112, 62, 61]:

$$\frac{\partial^2 \phi_1^*}{\partial t^{*2}} + g\frac{\partial \phi_1^*}{\partial z^*} = 0 \text{ on } z^* = D^*. \tag{7.4}$$

On the seabed the kinematic boundary condition is given as follows

$$\frac{\partial \phi_2^*}{\partial z^*} = 0 \text{ on } z^* = 0. \tag{7.5}$$

where ϕ_2^* is the potential function below the stratified layer till the sea bed.

There is a possibility of sheet vorticity appearing at the interface of the two stratified layers as mentioned in [81]. Since this effect is localized, a simplification is to consider the average of the two tangential velocities at the top and the bottom layers. This would eliminate the tangential velocity imbalance. However, a condition on the vertical velocity is still required to be imposed at the interface of the two stratified layers and this is satisfied by the kinematic boundary conditions. Following [81], the kinematic boundary conditions at the stratification are given by

$$\frac{\partial \phi_1^*}{\partial z^*} = \frac{\partial \beta^*}{\partial t^*} + \frac{\partial \phi_1^*}{\partial r^*}\frac{\partial \beta^*}{\partial r^*} \text{ on } z^* = \beta^*(r^*, t^*)$$

$$\frac{\partial \phi_2^*}{\partial z^*} = \frac{\partial \beta^*}{\partial t^*} + \frac{\partial \phi_2^*}{\partial r^*}\frac{\partial \beta^*}{\partial r^*} \text{ on } z^* = \beta^*(r^*, t^*).$$

since change in β along r is small [20, 81], we linearize to get

$$\frac{\partial \phi_1^*}{\partial z^*} = \frac{\partial \phi_2^*}{\partial z^*} \text{ on } z^* = H^*. \tag{7.6}$$

We also introduce a combined dynamic and kinematic boundary condition on the stratified layer for ϕ_2^*, similar to the one imposed on the free surface to capture the movement of particles, around the stratified layer, which is expressed as

$$\frac{\partial^2 \phi_2^*}{\partial t^{*2}} + g\frac{\partial \phi_2^*}{\partial z^*} = 0 \text{ on } z^* = H^*. \tag{7.7}$$

It should also be noted that the stratified layer manifests an oscillatory behaviour due to the presence of internal waves [81, 113, 114].

The volcano is considered as a point-source suspended in the water at some elevation z_0^* from the sea level. We justify this by the fact that the generated waves are studied at a distance of much larger scale than the horizontal and vertical size of the volcano.

7.1.2 Density distribution

We introduce a stratification at $z^* = H^*$ and consider the density distribution motivated by [20]. The stratified layer separates a layer of relatively warm water (and so less dense) from a deeper layer of denser, colder water; the difference in density between these two layers is nearly 0.5%. We consider a uniform density ρ_0 from the free surface $z^* = D^*$ till the stratification level $z^* = H^*$ and $(1 + \alpha)\rho_0$ below the stratification, where α is a small scalar constant.

It should also be noted that, when a volcano releases heat, the resulting effect is the coalescence of the heated water into a turbulent column characterized by predominantly vertical convective motion [6]. This column of heated water is commonly referred to as the stem of the vertical plume. The vertical plume will grow laterally and cools down as it entrains ambient sea water. It has been reported [115] that the temperature in the vertical plume falls off rapidly reaching nearly 30° Celsius at 10 m from the vent and nearly 6° Celsius at 100 m from the vent, and implies that by the time the vertical plume reaches near the stratification the temperature of the plume is nearly the same as of the sea water around it. Hence it may be assumed that the vertical temperature increase in the vicinity of the volcano will have insignificant effect on the stratified layer separating the layer of warm water with the layer of relatively cold water. Thus it can be assumed that the stratification is preserved even in the presence of volcanic eruption, justifying our stratified model.

Assuming water to be at rest before the beginning of eruption, we can set all potential functions and its derivatives with respect to time equal to zero. This gives us the following initial conditions:

$$\phi_1^*(r^*, z^*, t^* = 0) = 0 \quad \text{and} \quad \frac{\partial \phi_1^*(r^*, z^*, t^* = 0)}{\partial t^*} = 0; \tag{7.8}$$

$$\phi_2^*(r^*, z^*, t^* = 0) = 0 \quad \text{and} \quad \frac{\partial \phi_2^*(r^*, z^*, t^* = 0)}{\partial t^*} = 0. \tag{7.9}$$

The following are a few additional assumptions used in this modeling. First of all, the conic structure of the volcano creating localized variation in ocean relief is not taken into account. Another assumption is about the radial symmetry of the sea bed. In reality, sea beds have two-dimensional heterogeneity, but it is not so important in our analysis. As it was shown [38], the energy of tsunami waves propagate along the ray tubes, and inside each (narrow) tube the depth variation along the coordinate orthogonal to the ray can be ignored [62, 38]. We also impose the continuity of pressure at the stratified layer i.e., $P_- = P_+$ where $P_\pm$ refer to the limits of the pressure P from above and below the interface [81].

7.2 Non-dimensionalisation

The governing equations are given by

$$\frac{\partial^2 \phi^*}{\partial r^{*2}} + \frac{1}{r^*}\frac{\partial \phi^*}{\partial r^*} + \frac{\partial^2 \phi^*}{\partial z^{*2}} = \frac{-2\delta(r^*)\delta(z^* - z_0^*)}{r^*\rho} q^*(t^*), \tag{7.10}$$

where $\phi^* = \phi_1^*$ is the potential function in the top stratified layer and $\phi^* = \phi_2^*$ is the potential function in the bottom stratified layer. The boundary and initial conditions are given as follows

$$\frac{\partial^2 \phi_1^*}{\partial t^{*2}} + g\frac{\partial \phi_1^*}{\partial z^*} = 0 \text{ on } z^* = D^*, \tag{7.11}$$

$$\frac{\partial^2 \phi_2^*}{\partial t^{*2}} + g\frac{\partial \phi_2^*}{\partial z^*} = 0 \text{ on } z^* = H^*, \tag{7.12}$$

$$\frac{\partial \phi_1^*}{\partial z^*} = \frac{\partial \phi_2^*}{\partial z^*} \text{ on } z^* = H^*, \tag{7.13}$$

$$\frac{\partial \phi_2^*}{\partial z^*} = 0 \text{ on } z^* = 0, \tag{7.14}$$

$$\phi_1^*(r^*, z^*, t^* = 0) = 0 \quad \text{and} \quad \frac{\partial \phi_1^*(r^*, z^*, t^* = 0)}{\partial t^*} = 0, \tag{7.15}$$

and

$$\phi_2^*(r^*, z^*, t^* = 0) = 0 \quad \text{and} \quad \frac{\partial \phi_2^*(r^*, z^*, t^* = 0)}{\partial t^*} = 0. \tag{7.16}$$

It is assumed that the function $2q^*(t^*)$ is finite and is represented by Heaviside step function in time. This can be interpreted as an eruption starting at $t^* = 0$.

For non-dimensionalisation we consider the following: $r^* = D^* r, z^* = D^* z, t^* = \sqrt{\frac{D^*}{g}}t, \phi^* = S_0 D^* \sqrt{D^* g}\phi, q^*(t^*) = \rho_0 S_0 D^{*2}\sqrt{D^* g}q(t), \delta(r^*) = \frac{\delta(r)}{D^*}, \delta(z^* - z_0^*) = \frac{\delta(z-z_0)}{D^*}$, where S_0 is the non-dimensional amplitude of the displacement source related to the total volume of the explosion, $S_0 = \frac{V}{\pi r_0^{*2} z_0^*}$ and V represents the volume of explosion. D^* is the total depth, g is the acceleration due to gravity.

The governing equations with the boundary and initial conditions now take the form

$$\frac{\partial^2 \phi}{\partial z^2} + \frac{\partial^2 \phi}{\partial r^2} + \frac{1}{r}\frac{\partial \phi}{\partial r} = \frac{-2\delta(r)\delta(z - z_0)\rho_0}{r\rho} q(t), \tag{7.17}$$

where $\phi = \phi_1$ is potential function in top stratified layer and $\phi = \phi_2$ is the potential function in the bottom stratified layer.

$$\frac{\partial^2 \phi_1}{\partial t^2} + \frac{\partial \phi_1}{\partial z} = 0 \text{ on } z = 1, \tag{7.18}$$

$$\frac{\partial^2 \phi_2}{\partial t^2} + \frac{\partial \phi_2}{\partial z} = 0 \text{ on } z = H, \tag{7.19}$$

$$\frac{\partial \phi_1}{\partial z} = \frac{\partial \phi_2}{\partial z} \text{ on } z = H, \tag{7.20}$$

$$\frac{\partial \phi_2}{\partial z} = 0 \text{ on } z = 0, \tag{7.21}$$

$$\phi_1(r, z, t = 0) = 0 \quad \text{and} \quad \frac{\partial \phi_1(r, z, t = 0)}{\partial t} = 0, \tag{7.22}$$

and

$$\phi_2(r, z, t = 0) = 0 \quad \text{and} \quad \frac{\partial \phi_2(r, z, t = 0)}{\partial t} = 0 \tag{7.23}$$

where $H = \frac{H^*}{D^*} < 1$.

7.3 Method of solution

We will solve the problem in two parts. First, in the region below the stratified layer where the point source is located (with the potential function by ϕ_2) and then in the region above the stratified layer (with the potential function by ϕ_1). We find the Green's functions

$$G_1(r, z, t) = \frac{1}{2\pi i} \int_{c-\infty i}^{c+\infty i} e^{pt} \int_0^\infty \hat{G}_1(k, z, p) J_0(kr) k dk dp$$

and

$$G_2(r, z, t) = \frac{1}{2\pi i} \int_{c-\infty i}^{c+\infty i} e^{pt} \int_0^\infty \hat{G}_2(k, z, p) J_0(kr) k dk dp$$

for the governing equations in both the cases. Where G_1 and G_2 are green's functions in the bottom and top stratified layers respectively. The solution for an arbitrary source can be found by convoluting it with the Green's functions [61, 60]. Here G_1

and G_2 denote the Green's function in the region below and above the stratified layer respectively, J_0 is the Bessel function of the first kind of order zero, k is Hankel-transformed r coordinate, p is Laplace-transformed t variable, and $\hat{G}_1$ and $\hat{G}_2$ denote the joint Hankel and Laplace transform of Green's function in the top and the bottom stratified layers respectively. The term $q(t)$ is assumed to be a Heaviside step function in time.

7.3.1 Region in the bottom stratified layer

In the region below the stratified layer, applying Laplace transform with respect to t and Hankel transform with respect to r will give a system of equations as follows

$$\frac{d^2\hat{G}_1}{dz^2} - k^2\hat{G}_1 = 0, \tag{7.24}$$

$$p^2\left(\hat{G}_1\right)_{z=H} + \left(\frac{d\hat{G}_1}{dz}\right)_{z=H} = 0, \tag{7.25}$$

$$\frac{d\hat{G}_1}{dz} = 0 \text{ at } z = 0 \tag{7.26}$$

with continuity and jump conditions

$$\left(\hat{G}_1\right)_{z=z_0+\Delta z} = \left(\hat{G}_1\right)_{z=z_0-\Delta z}, \tag{7.27}$$

and

$$\left(\frac{d\hat{G}_1}{dz}\right)_{z=z_0+\Delta z} - \left(\frac{d\hat{G}_1}{dz}\right)_{z=z_0-\Delta z} = -\frac{2}{(1+\alpha)p} \tag{7.28}$$

where $\hat{G}_1$ denotes the joint Hankel and Laplace transform of Green's function below the stratified layer. The solution of the above equations is given as follows

$$\hat{G}_1(k,z,p) = \frac{2cosh(kz_0)}{(1+\alpha)kp}\frac{(k(e^{kz}+e^{k(2H-z)})+p^2(e^{k(2H-z)}-e^{kz}))}{(p^2(1+e^{2kH})+k(e^{2kH}-1))};\text{ for } z_0 \le z \le H \tag{7.29}$$

and

$$\hat{G}_1(k,z,p) = \frac{2cosh(kz)}{(1+\alpha)kp}\frac{(k(e^{kz_0}+e^{k(2H-z_0)})+p^2(e^{k(2H-z_0)}-e^{kz_0}))}{(p^2(1+e^{2kH})+k(e^{2kH}-1))};\ \text{for } 0 \leq z \leq z_0. \tag{7.30}$$

7.3.2 Region in the top stratified layer

In the region above the stratified layer there is no point source and hence the governing equations become the Laplace equation in this region. Applying Laplace transform with respect to t and Hankel transform with respect to r will lead the system of equation as follows

$$\frac{d^2\hat{G}_2}{dz^2} - k^2\hat{G}_2 = 0, \tag{7.31}$$

$$p^2\left(\hat{G}_2\right)_{z=1} + \left(\frac{d\hat{G}_2}{dz}\right)_{z=1} = 0, \tag{7.32}$$

and

$$\frac{d\hat{G}_1}{dz} = \frac{d\hat{G}_2}{dz} \text{ at } z = H. \tag{7.33}$$

The solution of the above equations is given as follows

$$\hat{G}_2(k,z,p) = -\frac{2cosh(kz_0)}{kp(ksinh(kH)+p^2cosh(kH))}\left(\frac{p^2(k(e^{kz}+e^{k(2-z)})+p^2(e^{k(2-z)}-e^{kz}))}{(1+\alpha)(k(e^{kH}-e^{k(2-H)})-p^2(e^{k(2-H)}+e^{kH}))}\right). \tag{7.34}$$

It should be noted that with $H = 1$ and $\alpha = 0$ (i.e., the case when there is no stratification and hence uniform density), $\hat{G}_2(k,z,p)$ becomes

$$\bar{G}(k,z,p) = \frac{2cosh(kz_0)}{kp(ksinh(k)+p^2cosh(k))}(kcosh(k(1-z))+p^2sinh(k(1-z))) \tag{7.35}$$

which is the solution ($\bar{G}(k,z,p)$) without stratification presented in [61].

7.4 Surface elevation

The elevation of the free surface can be calculated using the boundary condition and the fact that the solution is the convolution of the Green's function and any source function [61, 60]. Hence the joint Laplace and Hankel transformed surface elevation is

$$\hat{\eta}(k,p) = p^2 \hat{G}_2(k,1,p)\hat{S}(k,p) \tag{7.36}$$

where $\hat{S}$ is the displacement potential source function and $\hat{G}_2$ is joint Laplace and Hankel transformed Green's function in the region above the stratified layer. We will now analyze the surface water waves generated by a source situated at $(0, z_0)$ with vent radius r_0. It should also be noted that we are considering $\hat{G}_2$ because we are interested in the surface waves and $\hat{G}_2$ represents the solution in the region above stratified layer and till free surface.

7.4.1 Instantaneous Duffy Source

Introduced by Unoki and Nakano in 1953 [63] and adopted by Duffy in 1992 [60] the instantaneous Duffy source function corresponds to instantaneously adding mass to the system at $z = z_0$, $0 < r < r_0$, where r_0 is the radius of the vent. The waves modeled due to a Duffy source could be considered as a conservative estimate of the expected Tsunami waves [61]. The Duffy displacement potential source function for the vent size of radius r_0 is represented as follows

$$S = [\theta(r) - \theta(r - r_0)]\theta(t) \tag{7.37}$$

where $\theta(\cdot)$ is the Heaviside step function. Using equation (7.36) and applying inverse Laplace and Hankel transforms we get surface elevation as a function of time t and distance from the source r as follows

$$\eta(r,t) = \frac{2r_0}{(1+\alpha)} \int_0^\infty \frac{N}{M} dk \tag{7.38}$$

where,

$$N = cosh(kz_0)J_1(kr_0)J_0(kr)(\omega_1 sin(\omega_1 t) - \omega_2 sin(\omega_2 t))$$

$$M = k(cosh(k(|H-1|))sinh(kH) - sinh(k(|H-1|))cosh(kH))$$

where η denotes the elevation due to instantaneous Duffy source, J_m denotes the Bessel function of the first kind of order m, $\omega_2^2 = ktanh(k(|H-1|))$ and $\omega_1^2 = ktanh(kH)$. Also, at $H = 1$ and $\alpha = 0$ elevation η becomes the elevation for Duffy source presented in [61] given by

$$\eta(r,t) = 2r_0 \int_0^\infty \omega J_0(kr)J_1(kr_0)\frac{sin(\omega t)cosh(kz_0)}{ksinh(k)}dk; \text{ (for } H = 1 \text{ and } \alpha = 0) \quad (7.39)$$

with $\omega^2 = ktanh(k)$.

7.5 Numerical implementation and parametric analysis

Equations (7.38) and (7.39) were integrated numerically using global adaptive quadrature [116, 117] and the results were plotted. Figure 7.2 (a) and (b) were plotted for a total depth $D = 1$, stratified layer H situated at 0.8, a volcano located at $z_0 = 0.5$ with vent size $r_0 = 0.05$, $\alpha = 0.005$ and for different values of non-dimensional distance $r = 2.5, 5, 7.5,$ and 10 and Figure 7.3 (a) and (b) were plotted for the case with no stratification while keeping all other parameters same as the previous case.

It can be inferred from Figure 7.2 (a) and (b) that the wave amplitude decreases with time and distance which is consistent with the case with no stratification (see Figure 7.3 (a) and (b)). However, from time histories in Figure:7.3 (b), it can be seen that the waves show a beating behaviour as they travel gradually away from the source, which is not observed in the case without stratification (Figure 7.3 (b)). From equation (7.38), it can be seen that there are two frequencies ω_1 and ω_2, which cause the beating phenomenon in the case when the stratified layer is present, where ω_1 and ω_2 corresponds to the non-dimensional angular frequency of the free surface waves and the oscillating stratified layer respectively. Also, it should be noted that the case with stratification has surface elevation of higher amplitude as compared to the case without stratification, refer to Figure 7.2 and Figure 7.3. In particular the maximum amplitude observed near the source for the case with stratification is 6.02351×10^{-3} as compared to 5.66999×10^{-3} for the case without stratification. Increase in amplitude of the surface elevation for the case with stratification may have been due to the effect of the presence of the waves traveling along the stratified layer. The waves present at the stratified layer may be considered as some form of transient internal waves (see [114, 113, 81] for discussion on coupling of surface and internal waves).

From Figure 7.2 (b), it can be seen that the waves slowly die out at a point with time. This is also the case when there is no stratification (Figure 7.3 (b)). From equations (7.38) and (7.39), it can be seen that this decay is caused by the broad banded frequency spectra over an infinite support leading to a decaying time function. Figure 7.2 (b) and Figure 7.3 (b) shows that the decay time for the waves for the case with stratification is larger than the wave decay time for the case without stratification, which is caused due to the beating phenomenon present in the case with stratification. It should be also noted from equations (7.38) and (7.39) that the solution tends to zero as $r \to \infty$.

From Figure 7.4, it can be seen that the amplitude of the surface waves increase with increasing z_0 i.e., the higher amplitudes were observed for the source which was closer to the surface. From equation (7.38), the increase in wave amplitude with increasing z_0 can be explained due to the presence of the term $cosh(kz_0)$, which is a strictly increasing function. Comparing Figure 7.2 (b) and Figure 7.5 (a) and (b), it can be seen that the beating behaviour is strong for the case when the source is located near the stratified layer (say $z_0 = 0.5$ in Figure 7.2 (b)) and it is weak for the case when the source is located away from the stratified layer (say $z_0 = 0.25$ and 0 in Figure 7.5 (a) and (b) respectively).

From Figure 7.6 (a), (b) and (c) it is observed that for a fixed location z_0 of the source in the ocean, on increasing the vent size r_0 the amplitude of the surface waves increases substantially which is an obvious observation from equation (7.38), as the amplitude of the surface waves is directly proportional to the vent size. It can also be explained in terms of more eruptive mass being added to the system, for higher values of r_0, which require higher energy to generate and sustain the waves, hence leading to a faster decay.

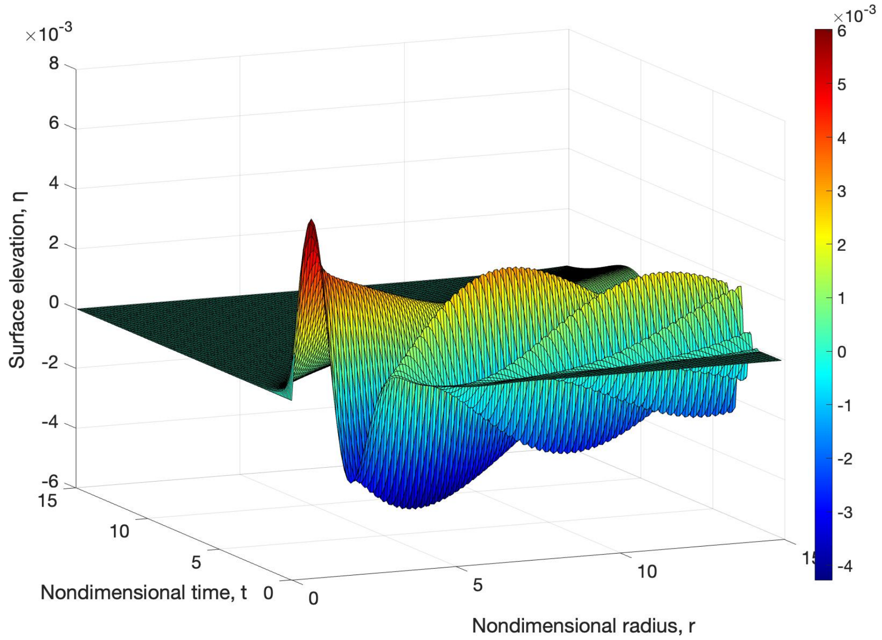

(a)

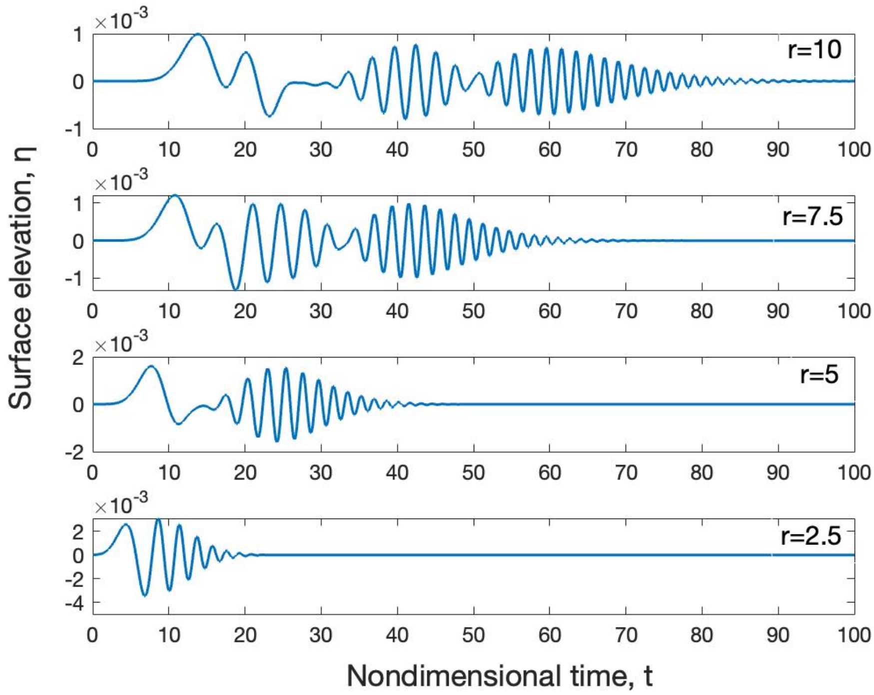

(b)

Figure 7.2: Spatial and temporal evolution of surface elevation for total depth $D = 1$, stratified layer situated at $H = 0.8$, volcano located at $z_0 = 0.5$ with vent size $r_0 = 0.05$ and $\alpha = 0.005$. The plots show a beating behavior with waves eventually decaying out.(a) A three dimensional plot of surface elevation and (b) Time histories of surface elevation for different values of r.

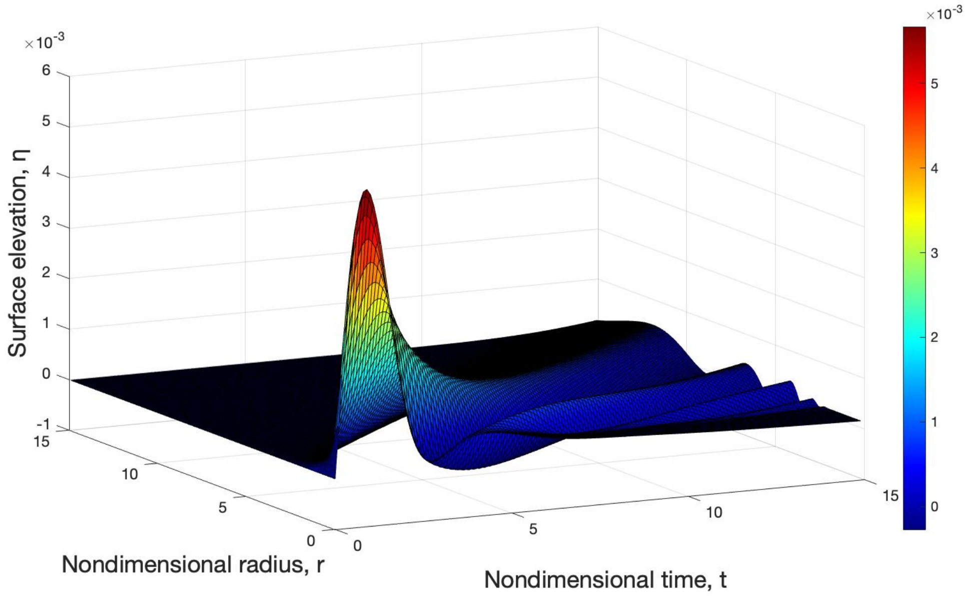

(a)

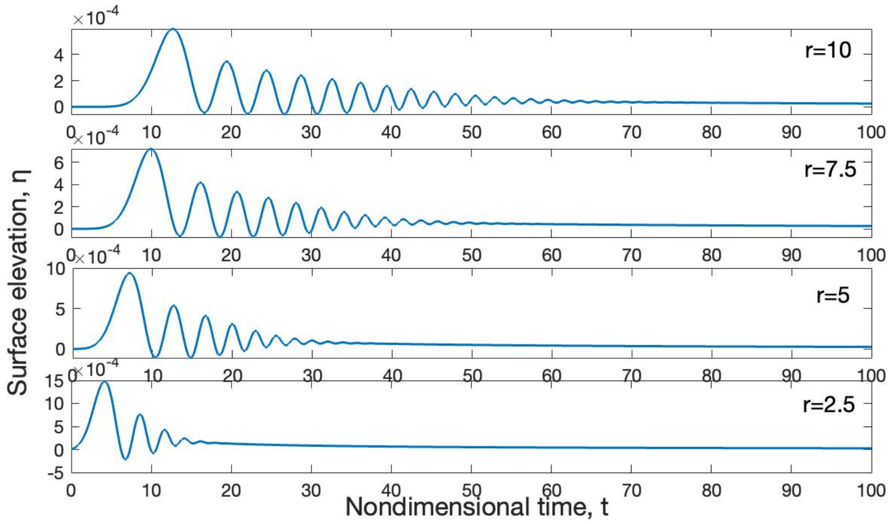

(b)

Figure 7.3: Spatial and temporal evolution of surface elevation for total depth $D = 1$, without stratified layer, volcano located at $z_0 = 0.5$ with vent size $r_0 = 0.05$ and $\alpha = 0.005$. No beating phenomenon observed. (a) A three dimensional plot of surface elevation and (b) Time histories of surface elevation for different values of r.

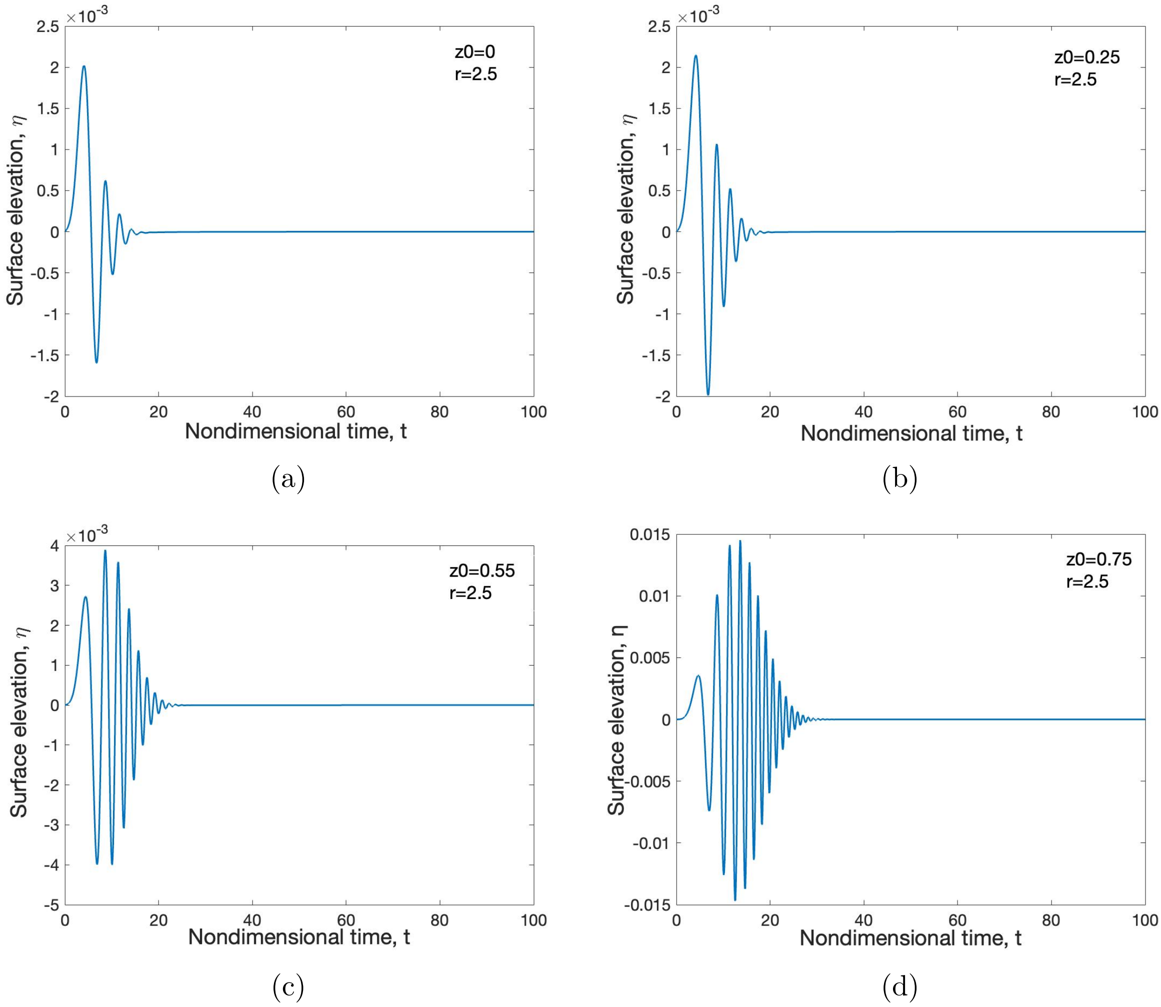

Figure 7.4: Surface elevation plots for different values of z_0 at a fixed value of $r = 2.5$, i.e., near the source, $\alpha = 0.005$, stratified layer at $H = 0.8$ and vent size $r_0 = 0.05$. Plot for elevation (a) when volcano is situated at $z_0 = 0$ (at the sea bed), (b) when volcano is situated at $z_0 = 0.25$, (c) when volcano is situated at $z_0 = 0.55$ and (d) when volcano is situated at $z_0 = 0.75$ (near the stratified layer).

Comparing Figure 7.2 (b), Figure 7.3 (b) and Figure 7.7 it can be seen that as H is approaching the free surface $Z = 1$, for a fixed location of a volcano, z_0 and a fixed vent size, r_0 the solution is converging to the case with no stratification, which is consistent with the analytical claim (see equations (7.38) and (7.39)). In particular, for a volcano located at $z_0 = 0.5$ with a vent size $r_0 = 0.05$, the maximum elevation observed at a radial distance of $r = 2.5$ from the volcano, when the stratified layer is located at $H = 0.8$ is 2.5739×10^{-3}, when the stratified layer is located at $H = 0.9$ is 1.9104×10^{-3} and when the stratified layer is at $H = 1$ (i.e., there is no stratification) is 1.4788×10^{-3}.

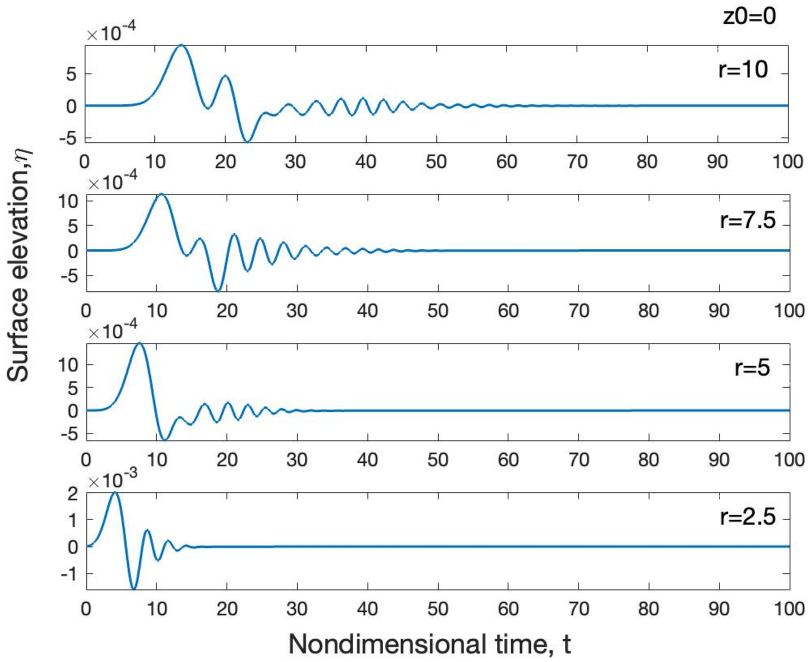

(a)

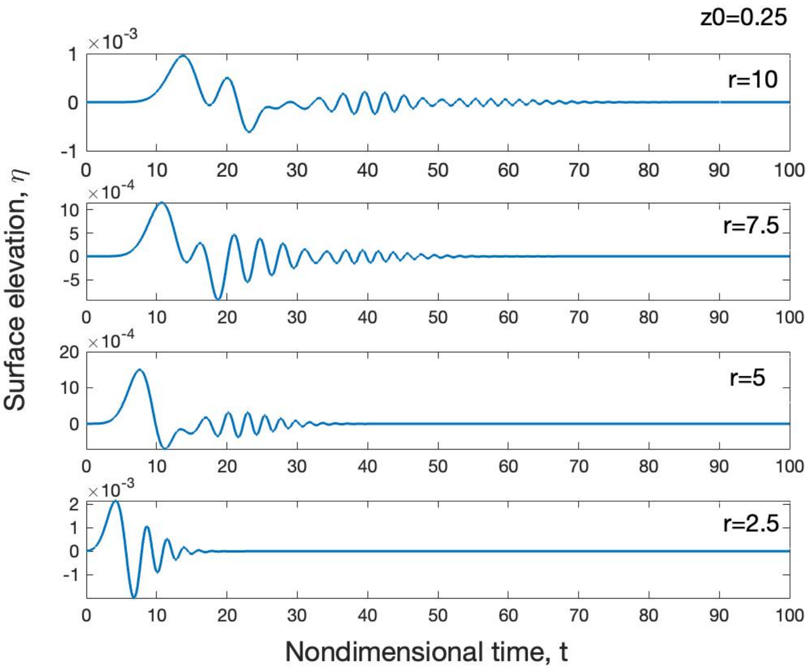

(b)

Figure 7.5: Surface elevation plots for $r = (2.5, 5, 7.5, 10)$, $H = 0.8$, $\alpha = 0.005$, $r_0 = 0.05$, (a) for $z_0 = 0$ and (b) $z_0 = 2.5$. A faint beating phenomenon is observed for the case when volcano was near the seabed, i.e., far away from the surface.

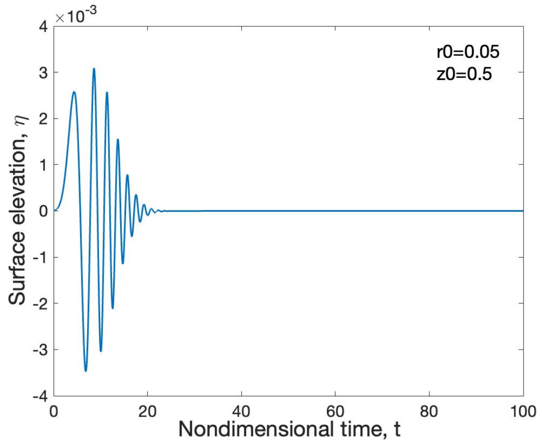

(a)

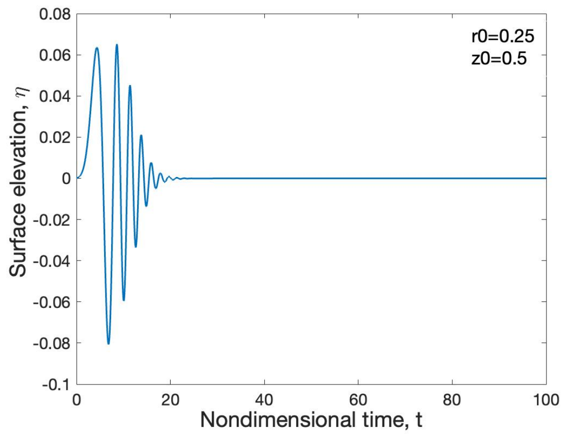

(b)

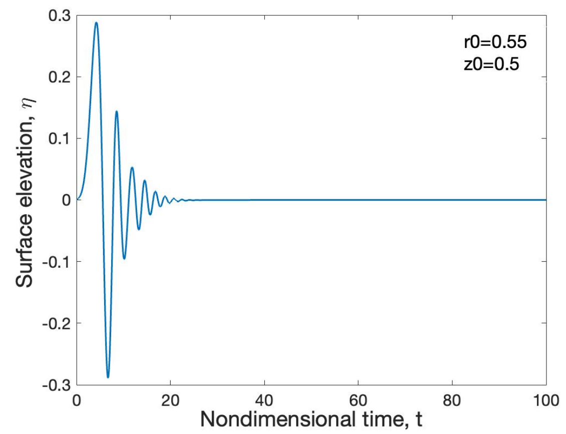

(c)

Figure 7.6: Surface elevation plotted for different vent sizes with fixed location of stratified layer $H = 0.8$, fixed location of volcano $z_0 = 0.5$, $\alpha = 0.005$ and various values of radial distance from the source $r = 2.5$. (a) $r_0 = 0.05$, (b) $r_0 = 0.25$ and (c) $r_0 = 0.55$. Higher amplitudes were observed for higher values of r_0.

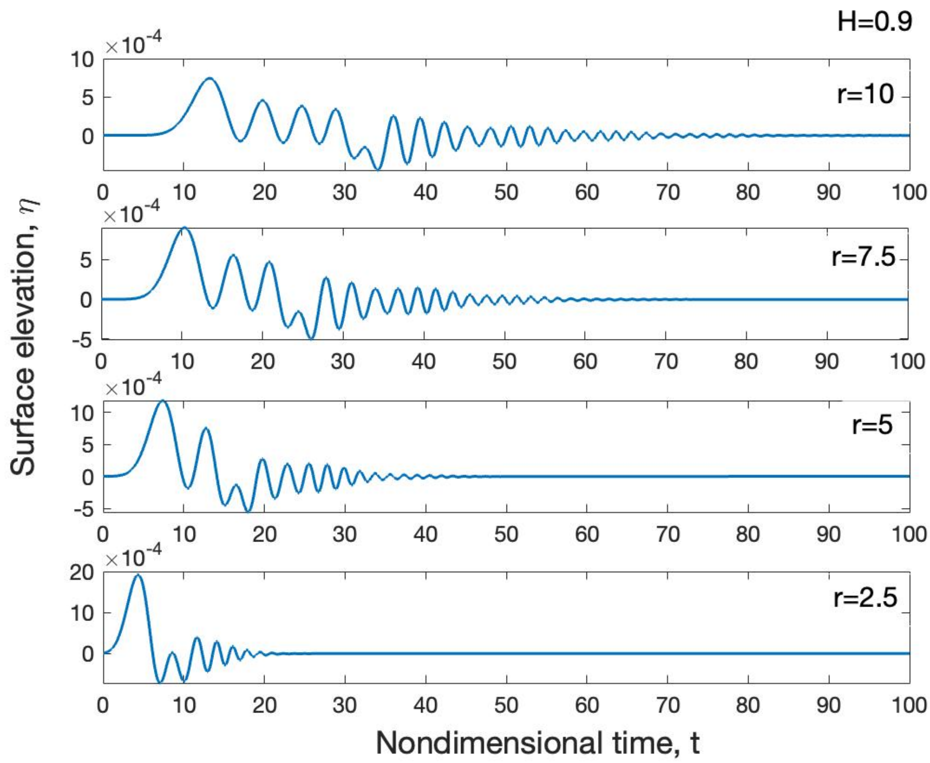

Figure 7.7: Surface elevation plots for stratified layer at $H = 0.9$, volcano at $z_0 = 0.5$, $\alpha = 0.005$, vent size $r_0 = 0.05$.

7.6 Remarks

In this chapter, an analytical model for tsunami generated by sub-aquatic volcanic eruption was formulated using potential function and by introducing stratified layer in the ocean. The fluid is considered to be inviscid because viscous forces in the ocean are negligible as compared to the buoyant and gravitational forces. It is observed that the analytical solution of the case with stratification converges to the case without stratification when the stratified layer approaches the free surface. The wave elevation in both the cases tends to zero as the radial distance tends to infinity. The free surface waves with higher amplitude and beating behaviour were observed in the case with stratification unlike the case without stratification. It is observed that the wave amplitude increases with the vent size and with decreasing the distance of the vent from the free surface.

Chapter 8

Three dimensional modelling of surface waves generated by shallow submarine volcanic eruption

As mentioned in Chapter 2, substantial submarine volcanic eruptions occurring within the top 500 meters from the water's surface are likely to produce waves on the surface. Traditional tsunami generation models employ a displacement potential function to account for the initial displacement caused by seismic or non-seismic events at the sea surface, as done in Chapter 7. This approach incorporates the addition of mass flux or seabed displacement due to various factors such as landslides or other geological activities. However, submarine volcanic eruptions not only introduce mass to the system but also generate a significant heat flux which is the focus of this chapter. Some of the recent studies [118, 119] also discuss the same mechanism for surface wave generation due to submarine volcanic eruptions.

8.1 Scenarios explored through computational modeling

The tsunami generation process is complex but can be summarized as follows: As the volcano erupts, it forces an initial upward movement of the water column directly above the site of the eruption. This sudden displacement creates a dome-shaped structure on the ocean's surface, a visible bulge formed by the rapid rise of water. Following the initial uplift, the water that was forced upward begins to collapse back. This collapse results in the formation of a trough directly above the volcanic site. The water rushes back down, creating a localized depression in the ocean surface. From this trough, waves start to propagate outward in all directions. The energy from the eruption causes these waves to travel rapidly across the ocean surface. As they move away from the trough, the waves grow in height and spread out [52, 53, 54, 55, 56, 57, 40, 58, 46, 59].

The heat flux causes convection flows driven by buoyant forces acting on the high-temperature, less dense water near the volcano. Consequently, this results in the upward movement of water. In a shallow environment with substantial heat flux, this vertical flow can penetrate the free surface and generate surface waves. Incorporating the heat flux introduces high temperatures near the volcano and includes the phenomenon of plume generation and the entrainment of water into the plume. This affects the vertical velocity (as discussed in Chapter 5), consequently impacting the generation of the surface waves.

We will utilize the three-dimensional ocean flow model outlined in Chapter 4 to examine the surface waves generated by the introduction of a high heat flux at the seabed in a shallow environment. A Gaussian heat flux profile, as depicted in Figure 4.1, will be applied at the seabed with significant heat flux values. We will investigate two different heat flux levels ($10000, 20000$ watts/m^2) at the seabed and compare the resulting surface waves. Additionally, we will analyze the surface elevation for the cases with different depth of volcano from free surface. This analysis aims to identify the best-case scenario for shallow volcanoes near the coast, which could potentially cause damage to infrastructure and coastal communities.

8.2 Model parameters and initial conditions

The model parameters will remain consistent with those assumed in Chapter 5, with the exception that the total depth will be set to 300 meters for both the cases. The initial velocities u, v, and w, along with the initial surface elevation h, are all set to zero. The boundary conditions will be the same as those assumed in Chapter 5. Initial salinity is set to be 35 ppt, initial temperature varies from 15° C to 9.16° C (see Figure. 8.1) and initial density varies from 1027.09 to 1025.97 kg/m^3.

(a) Initial temperature

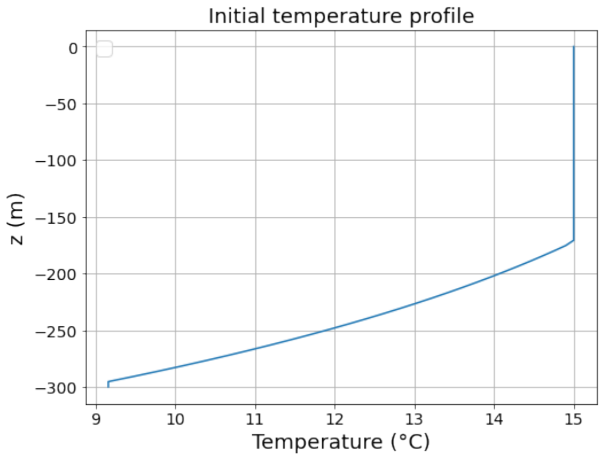

(b) Initial density

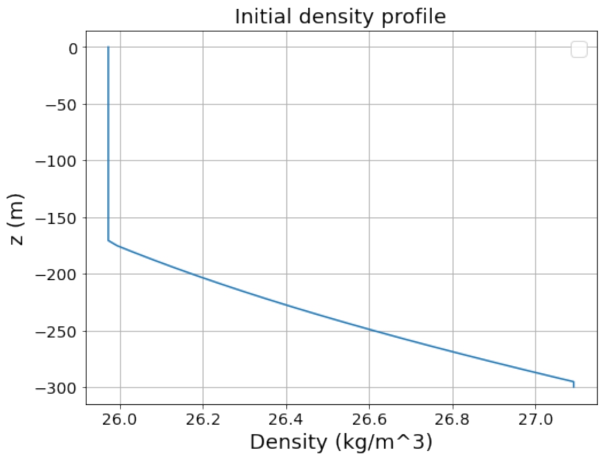

Figure 8.1: Plots for initial temperature and density profile.

8.3 Results

8.3.1 Case 1: Heat flux $20,000$ watts/m^2

A Gaussian heat flux profile was applied to the seabed, with the peak heat flux reaching $20,000$ watts per square meter at the coordinates $(x, y) = (0, 0)$ and gradually decreasing to zero in both directions.

Figure 8.2 (a) illustrates that one minute after the eruption begins, a dome-shaped structure forms on the free surface. Following this, the vertical dome undergoes a gravity collapse, creating a trough from which waves propagate outward on both sides (see Figure. 8.2 (b)-(d)), as discussed in [118, 119]. Figure 8.2 (b)-(d) demonstrate that with the continuous addition of heat flux at the seabed, the surface elevation increases, reaching approximately 1 meter at $t = 11$ minutes and 2 meters at $t = 13$ minutes. Additionally, these figures show that as the heat flux continues to be added and the wave elevation rises, the domain of influence of the waves on the surface expands. Specifically, in fig 8.2 (b), at $t = 6$ minutes, the waves dissipate within a range of 5000 meters on both sides, with the elevation reaching zero at this distance. However, Figure. 8.2 (c) and (d) indicate that there is a positive elevation at 5000 meters from the source, with the elevation decreasing to zero around 6000 meters from the source in both directions.

8.3.2 Case 2: Heat flux $10,000$ watts/m^2

In this case, a Gaussian heat flux, peaking at 10000 watts/m^2 at the coordinates $(x, y) = (0, 0)$, was applied to the bottom boundary.

In case 2, the initial upward displacement of the surface is observed six minutes after the eruption. As more heat flux is added, the initial dome-like structure collapses due to gravity, forming a trough. Subsequently, waves begin to propagate outwards from both sides of the trough (see Figure 8.3 (a)-(d)). Even after 13 minutes post-eruption, the surface elevation remains minimal, with a maximum of 0.02 meters. However, with continuous heat flux input (eruption) for over 20 minutes, the surface elevation increases significantly, reaching approximately 1.5 meters at 24 minutes after the initial eruption. At this point, the influence of the surface waves extends up to a range of 5000 meters (see Figure 8.3 (d)).

8.3.3 Comparison of case 1 and 2

It should be noted that in case 1, a heat flux of $20,000$ watts/m^2 was introduced at the seabed. Due to the large energy input, the simulations were executed for 15 minutes to ensure numerical stability.

In both cases, the phenomenon of surface wave generation is consistent with the findings discussed in [118, 119]. However, higher elevations were observed in a shorter

(a) h at time $t = 1$ minute

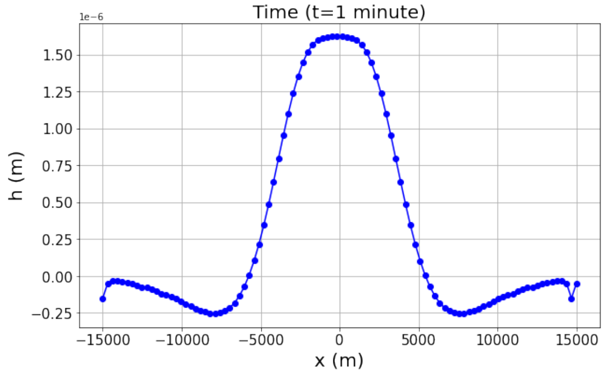

(b) h at time $t = 6$ minutes.

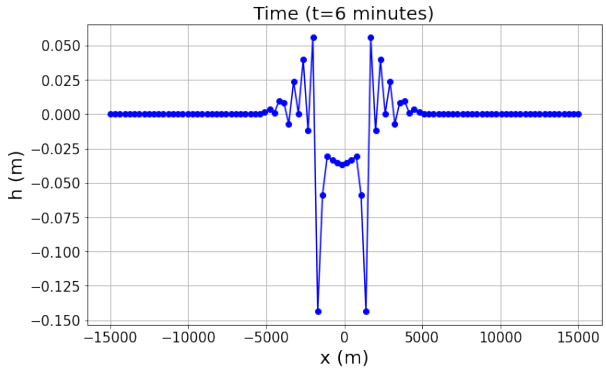

(c) h at time $t = 11$ minutes.

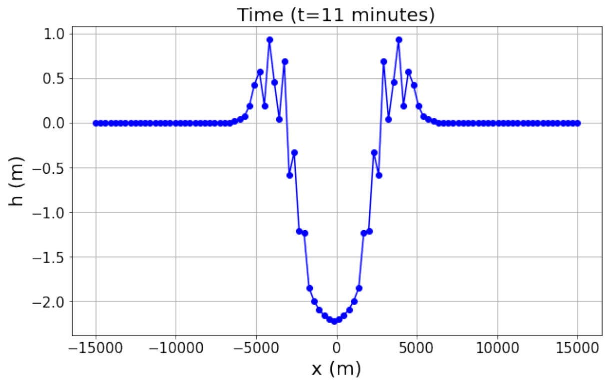

(d) h at time $t = 13$ minutes.

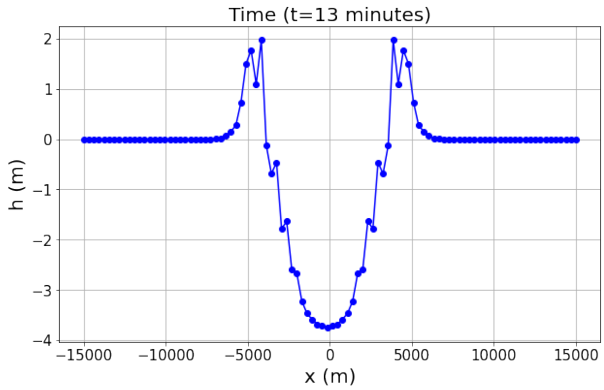

Figure 8.2: Plots of h for case 1 at different time from the eruption.

(a) h at time $t = 6$ minute

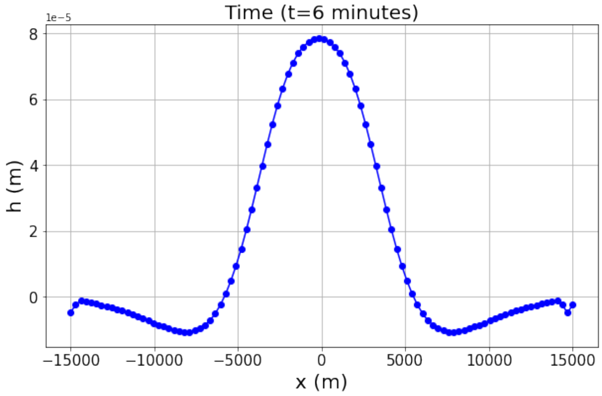

(b) h at time $t = 13$ minutes.

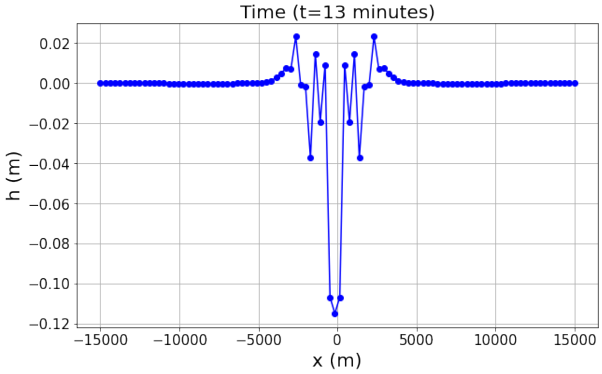

(c) h at time $t = 20$ minutes.

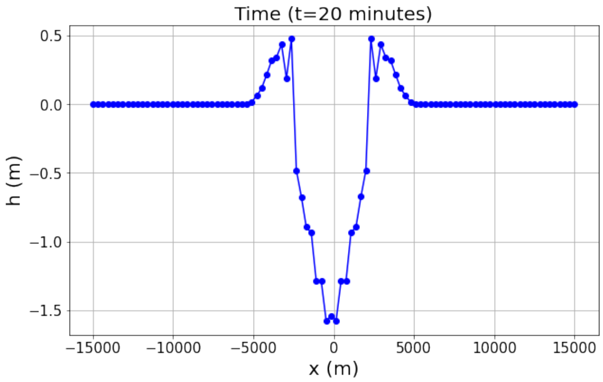

(d) h at time $t = 24$ minutes.

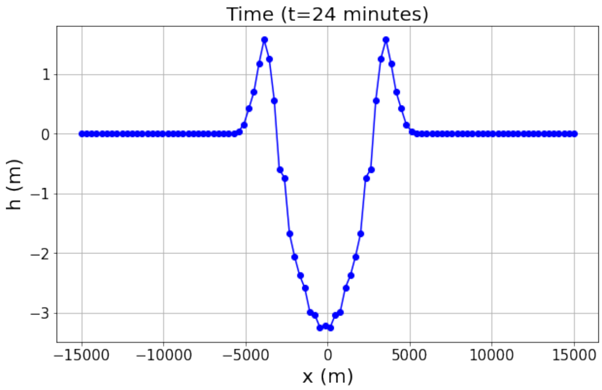

Figure 8.3: Plots of h for case 2 at different time from the eruption.

time span in case 1, where a larger heat flux was introduced at the seabed. This is because a larger heat flux rapidly heats the water around the volcano, increasing the temperature more significantly compared to case 2, for example after 6 minutes from the eruption the temperature near the volcano in case 1 was 600°C whereas in case 2 it was around 110°C (see Figure 8.4). Consequently, the water becomes less dense, resulting in a larger buoyant force. This causes the water to be convected upward more quickly, reaching the surface sooner and with higher impact velocity creating larger waves. It can further be noted from Figure 8.2 (d) and 8.3 (b) that at 13 minutes after the eruption the highest wave elevation in case 1 was 2 meters where as in case 2 it was around 0.03 meters.

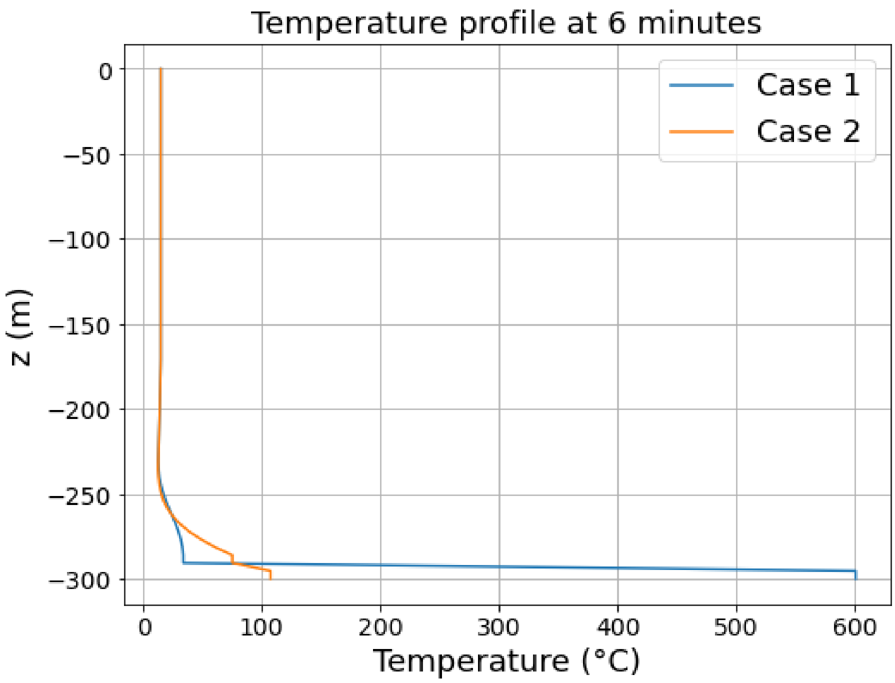

Figure 8.4: Temperature profile above the volcano for case 1 and 2 at 6 minutes.

The extent of the wave impact on the free surface varies between the two cases, despite observing nearly the same wave elevation. In the first case, when a two-meter wave was observed, the domain of influence extended approximately 6000 meters in both directions (see Figure 8.2 (d)). However, in the second case, with a nearly two-meter wave, the domain of influence was limited to within 5000 meters in both directions from the source (see Figure 8.3 (d)).

8.3.4 Comparison of the surface elevation with different depth values and fixed heat flux

For a fixed heat flux of 10,000 watts/m^2, the total depth of the system was reduced to 200 meters with heat flux at the seabed. This scenario corresponds to the crater of the volcano being closer to the free surface compared to case 2. In both cases, a constant heat flux was applied continuously for 24 minutes.

As depicted in Figure 8.6 (a) and 8.3 (a), six minutes after the eruption, an initial uplift with very small elevation was observed when the volcano was 300 meters from the free surface. In contrast, when the volcano was located 200 meters from the free surface, a trough and waves were observed six minutes after the eruption. Figure 8.5 (b) illustrates that 24 minutes after the eruption, a higher wave elevation was observed when the volcano was closer to the free surface. Specifically, a wave elevation of approximately 7.5 meters was recorded when the volcano was 200 meters from the free surface. In comparison, a wave elevation of approximately 1.7 meters was observed when the volcano was situated 300 meters from the free surface. These observations of increased wave elevation when the volcano is closer to the free surface have been corroborated in other studies [61].

8.4 Remarks

In this Chapter, a Gaussian heat flux was applied to the seabed to simulate the surface waves generated by submarine volcanic eruptions. The study explored the mechanism behind surface wave generation during major shallow submarine volcanic eruptions by applying heat flux to the seabed and found a strong correlation with previous research [118, 119]. It was observed that larger waves resulted from higher heat flux values and when the heat source was closer to the water surface. These findings are consistent with earlier studies and observations, such as those reported in [61]. This study proposes an alternative methodology for modeling tsunamis generated by submarine volcanic eruptions. By incorporating heat flux at the bottom boundary, the tsunami generation process accounts for the complex phenomena of vertical tephra transport

(a)

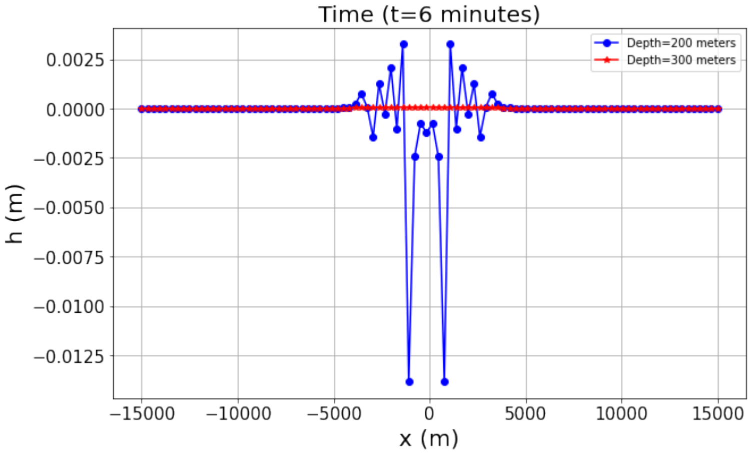

(b)

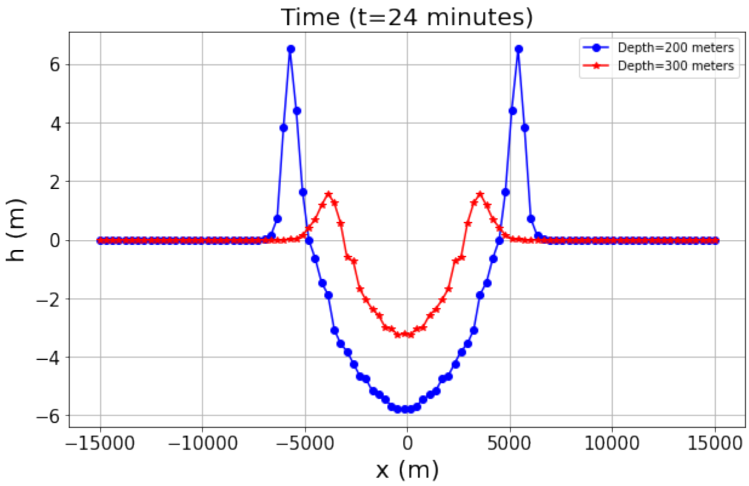

Figure 8.5: Surface wave elevation for the cases with variable depth and fixed heat flux.

(plume generation) and the entrainment of ambient seawater into the vertical plume, which impacts vertical velocity, as discussed in previous studies [71, 72].

Chapter 9

Conclusion and future work

This thesis has centered on developing mathematical models and conducting numerical simulations to analyze the flows generated by submarine volcanic eruptions in a stratified environment.

To simulate deep submarine volcanic eruptions, we utilized the well-established geophysical model PSOM [19, 18], introducing a moderate heat flux at the seabed. The simulations considered two primary cases for domain stratification—one based on (a) salinity and the other on (b) temperature—as well as two sub-cases with reduced stratification intensity for each primary scenario. Stratification intensity emerges as a key factor in controlling the vertical ascent of the plume in both stratified scenarios: in cases of strong stratification, the plume remains confined below the free surface, whereas under weak stratification, the plume reaches the free surface within 48 hours of eruption.

In both the stratified scenarios, rotational effect was observed throughout the entire domain. Near the heat source, cyclonic rotation occurred, which gradually transitioned into anti-cyclonic rotation extending up to the free surface. This pattern divided the domain into two distinct structured cells: the lower cell exhibited cyclonic rotation, while the upper cell maintained anti-cyclonic rotation. Radial flows showed radially convective cells in both the stratified cases, with the temperature-stratified environment yielding more stable flows. In contrast, salinity stratification induced thermal instability over time, resulting in axially symmetric cells at the plume's periphery and chaotic flow patterns. This finding underscores the sensitivity of convective flows in salinity stratified case to thermal gradients and stratification intensity.

Vertical flows showed consistent plume behavior across both stratification scenarios, with heated, buoyant water rising from the seabed. In temperature-stratified conditions, vertical velocity was initially high but decreased as the plume stabilized, while the salinity-stratified case exhibited a narrower flow due to limited buoyancy. Both cases displayed symmetrical vertical velocity patterns, with alternating upward and downward flows around the plume (more pronounced in the salinity case) due to interactions between warm and cool water. Surface elevation was found to be localized,reaching a maximum of 1.5 cm in the temperature stratified case and 0.7 cm in the salinity stratified case.

To examine the impact of submarine volcanic eruptions on equatorial oceanic flows, a detailed three-dimensional model was developed, building on the work of Constantin and Johnson [20, 81]. This model incorporated a density function designed to capture the density variations resulting from the formation of the vertical plume and its umbrella structure due to the eruption in a stratified domain. Analytical solutions indicated that flow velocities of the currents in the ocean domain are influenced by eruption-related factors, including the width of the buoyant vertical plume containing volcanic ash and the temperature gradient along the plume's vertical axis. Moreover, any changes in horizontal velocities were found to impact vertical velocity dynamics.

To simulate surface waves generated by submarine volcanic eruptions in domains with and without stratification a two-dimensional model based on potential function theory was developed. Analytical solutions indicated that, as the stratified layer approaches the free surface, the solution for the stratified case converges to that of the non-stratified case. In both cases, wave elevation diminishes to zero as the radial distance approaches infinity. However, in the stratified case, the free surface waves displayed higher amplitudes and a beating pattern, a behavior not observed in the non-stratified case, this was due to the internal waves generated at the stratified layer. Additionally, wave amplitude was found to increase with the vent size and as the vent's depth relative to the free surface was decreased.

Finally, the three-dimensional computational model PSOM was utilized to investigate surface wave generation due to high heat flux introduced at the seabed within a shallow domain. This study presents an alternative theory for modeling tsunamis triggered by submarine volcanic eruptions. By incorporating heat flux at the bottom boundary, the model captures the complex dynamics of vertical tephra transport (plume formation) and the entrainment of surrounding seawater into the plume, which significantly influences vertical velocity. The surface waves generated exhibited a strong correlation with previous studies that modeled wave generation from submarine eruptions using velocity potential source functions and laboratory experiments. It was observed that larger surface waves resulted from higher heat flux values and when the heat source was positioned closer to the water surface, findings that align with earlier research and the two-dimensional model developed in this thesis.

9.1 Broader implications of the work

This research work is crucial for advancing our understanding of the far-reaching impacts of submarine volcanic eruptions. By developing detailed mathematical models and simulations, this work lays the foundation for assessing the implications of eruptions on underwater infrastructure, such as fiber-optic cables, which are vital for global communications and are vulnerable to the intense pressures, thermal dynamics, and high velocities generated by such eruptions. Furthermore, the findings contribute to tsunami modeling, offering insights into potential wave patterns and heights that could threaten coastal communities. Understanding the dynamics of plume formation and flow velocities in a stratified ocean has important implications for predicting the spread of volcanic ash and other particulates, which can affect marine ecosystems, fisheries, and the deposition of metals.

Submarine eruptions also pose a significant threat to coral reefs, which are essential to marine biodiversity and support fish populations that are crucial to the economies of small island nations, particularly those in the Ring of Fire and near subduction zones. Damage to these ecosystems can lead to declines in fish stocks, impacting food security and livelihoods in these regions. On a broader scale, this research aids in understanding geological changes in volcanic regions, which could impact territorial boundaries, leading to geopolitical implications as countries evaluate underwater territory and resources. Additionally, the study of subaqueous flows and their interactions with equatorial ocean currents offers valuable insights into how large-scale eruptions can influence broader oceanic circulation patterns, potentially affecting climate and ocean health on a global scale. By providing a comprehensive look at the dynamics of submarine volcanic eruptions, this work is a step toward more resilient infrastructure, improved early-warning systems, and better-informed policies to safeguard communities, ecosystems, and economic stability.

9.2 Future work

Future work could expand on this study by incorporating additional environmental variables and refining the accuracy of the numerical model to better capture the complex dynamics of submarine volcanic eruptions. One key area for exploration is the inclusion of more intricate seabed topographies, which would help simulate eruptions in diverse geological settings and assess how uneven or layered seabeds influence plume behavior and wave generation. Additionally, future studies could integrate chemical reactions between volcanic gases and seawater, providing a more comprehensive understanding of underwater volcanic effects on ocean chemistry, which has significant implications for marine life and carbon cycles. The models could also be expanded to analyze the interaction of multiple, simultaneous eruptions within a regional system, offering insights into cumulative effects on ocean currents, sediment displacement and regional seismicity. Beyond improving the physical models, future work could also focus on coupling these simulations with real-time data from undersea monitoring networks, using machine learning techniques to predict eruption impacts on a faster timescale. Such advancements would enhance predictive capabilities, allowing for proactive measures to mitigate risks to underwater infrastructure, marine ecosystems, and coastal populations.

Appendix A

Mathematical functions and definitions

A.1 Heaviside step function

The Heaviside step function $\theta(x)$, also called the unit step function, is a discontinuous function, whose value is zero for negative arguments $x < 0$ and one for positive arguments $x > 0$,

$$\theta(x) = \left\{ \begin{array}{ll} 0 & \text{if } x < 0 \\ 1 & \text{if } x > 0 \end{array} \right\} \tag{A.1}$$

The function is often used in control theory and signal processing mathematics to describe a signal that switches on at a specific moment and stays on eternally.

A.2 Dirac delta function

The Dirac delta function on a real line can be defined as a function which is zero everywhere except the origin, where it is infinite,

$$\delta(x) = \left\{ \begin{array}{ll} 0 & \text{if } x \neq 0 \\ +\infty & \text{if } x = 0 \end{array} \right\} \tag{A.2}$$

which is also constrained to satisfy

$$\int_{-\infty}^{+\infty} \delta(x)dx = 1. \tag{A.3}$$

The Heaviside function can also be viewed as an antiderivative of the Dirac delta function,

$$\theta(x) = \int_{-\infty}^{x} \delta(t)dt. \tag{A.4}$$

A.3 Stream function

An incompressible fluid satisfy the conservation equation

$$\nabla.\mathbf{v} = 0, \tag{A.5}$$

where $\mathbf{v}$ is the velocity field, in two-dimensional cartesian coordinate system (A.5) can be written as

$$\frac{\partial u}{\partial x} + \frac{\partial v}{\partial y} = 0 \tag{A.6}$$

where u and v are horizontal and vertical velocity components respectively. Equation (A.6) implies the existence of a function ψ such that

$$u = \frac{\partial \psi}{\partial y}, \ v = -\frac{\partial \psi}{\partial x} \tag{A.7}$$

called the stream function. A family of curves $\psi =$ constant represent "streamlines", hence, the stream function remains constant along a stream line.

A.4 Euler equation

Let $\mathcal{B}$ be any property of the fluid (mass, momentum, energy, etc.) and let $b = d\mathcal{B}/dm$ be the intensive value of $\mathcal{B}$ (amount of $\mathcal{B}$ per unit mass) in any small element of the fluid. For the arbitrary moving and deformable control volume, the instantaneous total change of $\mathcal{B}$ in the material volume (MV) is equal to the instantaneous total change of $\mathcal{B}$ within the control volume (V) plus the net flow of $\mathcal{B}$ into and out of the control volume through its control surface (S). Let ρ denotes the density of the fluid, $\mathbf{n}$ the outward normal to the control volume surface, $\mathbf{v}(t, \mathbf{x})$ the velocity of the fluid, $\mathbf{v}_s(t, \mathbf{x})$ the velocity of the deforming control volume surface, and $\mathbf{v}_r(t, \mathbf{x})$ the relative velocity by which the fluid enters/leaves the control volume, then the Reynolds transport theorem gives

$$\left(\frac{d\mathcal{B}}{dt}\right)_{MV} = \frac{d}{dt}\left(\int_{V(t)} b\rho \, dV\right) + \int_{S(t)} b\rho \mathbf{v}_r \cdot \mathbf{n} \, dS, \tag{A.8}$$

which can be reduced to

$$\left(\frac{d\mathcal{B}}{dt}\right)_{MV} = \int_V \left(\frac{\partial}{\partial t}(\rho b) + \nabla \cdot (\rho b \mathbf{v})\right) \, dV, \tag{A.9}$$

using material derivative we will have

$$\left(\frac{d\mathcal{B}}{dt}\right)_{MV} = \int_V \left(\frac{D}{Dt}(\rho b) + \rho b \nabla \cdot \mathbf{v}\right) \, dV. \tag{A.10}$$

Newton's law in Lagrangian coordinates can be written as

$$\left(\frac{d(m\mathbf{v})}{dt}\right)_{MV} = \left(\int_V f \, dV\right) \tag{A.11}$$

where f is the external force per unit volume acting on the material volume.

A.4.1 Non-conservative form

Taking $\mathcal{B} = \mathbf{v}$ in equation (A.10) we will get

$$\int_V \left(\frac{D}{Dt}(\rho \mathbf{v}) + (\rho b \nabla \cdot \mathbf{v}) - f\right) \, dV = 0 \tag{A.12}$$

for integral to be zero at any control volume, the integrand has to be zero. Expanding the material derivative and using equation of continuity we will have

$$\rho \left(\frac{\partial \mathbf{v}}{\partial t} + (\mathbf{v} \cdot \nabla)\mathbf{v}\right) = f. \tag{A.13}$$

Equation (A.13) is the non-conservative form of the Euler equation.

A.4.2 Conservative form

Conservative form is obtained by taking $b = \mathbf{v}$ in equation (A.9)

$$\int_V \left(\frac{\partial}{\partial t}(\rho \mathbf{v}) + \nabla \cdot (\rho \mathbf{v}\mathbf{v}) - f \right) \, dV = 0 \tag{A.14}$$

for integral to be zero at any control volume, the integrand has to be zero. We will get conservative form of Euler equation as

$$\frac{\partial}{\partial t}(\rho \mathbf{v}) + \nabla \cdot (\rho \mathbf{v}\mathbf{v}) = f \tag{A.15}$$

where $\rho \mathbf{v}\mathbf{v}$ is the dyadic product.

Appendix B

Key ocean-related phenomena

B.1 Mesoscale and submesoscale flows

Mesoscale flows refer to atmospheric or oceanic circulations that occur on a spatial scale of tens to hundreds of kilometers and have a time scale of several hours to several days. These flows are typically generated by horizontal pressure gradients and are influenced by Earth's rotation, as well as variations in temperature and moisture.

Submesoscale flows, on the other hand, occur on smaller spatial scales of less than 10 kilometers and have a shorter time scale of hours to days. They are often generated by turbulence and are influenced by a range of factors, including wind, currents, and temperature gradients.

Both mesoscale and submesoscale flows play important roles in the Earth's atmosphere and oceans, and they can have significant impacts on weather, climate, and marine ecosystems. Understanding these flows and their interactions is important for improving our ability to predict and mitigate natural disasters and for managing marine resources.

B.2 Phytoplankton

Phytoplankton are microscopic, photosynthetic organisms that float in the ocean and other bodies of water. They produce about half of the planet's oxygen and form the base of the marine food web, providing essential nutrients for other marine organisms.

Phytoplankton come in many shapes and sizes, including diatoms, dinoflagellates, and cyanobacteria. They are found in all types of aquatic environments and play an important role in nutrient cycling, food web dynamics, and carbon dioxide uptake. Changes in their abundance and distribution can have significant impacts on marine ecosystems, making monitoring and understanding phytoplankton populations important for managing the health of our oceans and other bodies of water.

Phytoplankton are an important indicator of water quality and ecosystem health. Changes in their abundance and distribution can be caused by a range of factors, including climate change, nutrient pollution, and over fishing. Understanding phytoplankton populations is important for managing the health of our oceans and other bodies of water, as they play a critical role in maintaining the health of marine ecosystems and the planet as a whole.

B.3 Spice

In the realm of oceanography, the term "spice" (symbolized by τ) refers to fluctuations in both temperature and salinity within seawater, either across space or time. These fluctuations maintain the water's density at a constant level. Essentially, for a given spice level, any rise in temperature is counteracted by a corresponding change in salinity to uphold the density of the water. When temperature increases, density typically decreases, yet an increase in salinity counterbalances this by boosting density. This phenomenon of density-compensated thermohaline variability is prevalent throughout the upper layers of the ocean. In simpler terms, warmer and saltier water is considered "spicier," while cooler and less salty water is described as "mintier." This concept provides vital insights into the intricate dynamics of oceanic processes, serving as a fundamental principle in understanding the behavior of marine environments. When the density ratio is 1, any variations in thermohaline properties constitute spice, and there are no density fluctuations present.

Seawater density, determined by salinity and temperature, controls much of the movement of water and thermohaline flow in the ocean. Changes in potential temperature Θ and salinity s, are multiplied α with their thermal expansion and haline contraction coefficient β equal to each other; $\alpha d\Theta$ and βdS are both proportional to a change in density and are both terms of the linearized equation of state of the ocean. This similarity ($\alpha d\Theta = \beta dS$) is supposed to be relevant for understanding the consequences of sea water mixing.

B.4 Baroclinic mode

Baroclinic modes describe the vertical structure of waves in a stratified fluid like the ocean. They arise due to variations in density with depth, leading to different responses to forces (such as wind or tidal forces) at different depths. These modes help in analyzing the internal waves and currents that propagate through the ocean's layers.

B.4.1 Characteristics of the first baroclinic mode

1. **Vertical structure:** The first baroclinic mode is characterized by a single zero crossing in the vertical profile of the velocity field, indicating a change in the direction of wave velocity once with depth. In this mode, the surface and deeper layers move in opposite directions, meaning they are out of phase.

2. **Density and Pressure:** In this mode, the density perturbations are such that the upper layer (above the zero crossing) and the lower layer (below the zero crossing) move in opposite directions. The pressure gradients are aligned to maintain this structure, balancing the horizontal differences in density.

3. **Wavelength and Speed:** This mode generally has a longer wavelength compared to higher-order modes and usually propagates faster because it involves the interaction of the entire water column.

4. **Energy Propagation:** The first baroclinic mode is essential for transferring energy from the surface, where wind and atmospheric forces act, to the deeper ocean layers. It significantly impacts the dynamics of large-scale ocean circulation and mixing.

5. **Thermocline Involvement:** The thermocline, a layer with a steep temperature gradient, typically marks the transition point (zero crossing) for the first baroclinic mode. Water above and below this layer moves in opposite directions.

B.4.2 Mathematical representation

The vertical structure of the first baroclinic mode can be described by solving the linearized equations of motion for a stratified fluid, leading to an eigenvalue problem. The first eigenfunction corresponding to the lowest eigenvalue represents the first baroclinic mode of the equation,

$$\frac{\partial^2 \Phi}{\partial z^2} + \Big(\frac{N^2(z)}{c^2}\Big)\Phi = 0. \tag{B.1}$$

Here: $\Phi(z)$ is the vertical structure function, $N(z)$ is the buoyancy frequency, a measure of the stratification and c is the phase speed of the wave.

B.4.3 Steps to calculate the first baroclinic mode

1. The buoyancy frequency $N(z)$, which measures the stratification of the ocean, is given by:

$$N(z) = \sqrt{\frac{-g}{\rho_0}\frac{d\rho}{dz}}$$

where: g is acceleration due to gravity, ρ_0 is a reference density and $\frac{d\rho}{dz}$ is the vertical density gradient.

2. Set up the eigenvalue problem (B.1).

3. Apply boundary conditions.

4. Solve the eigenvalue problem. Numerical methods are typically used to solve this problem, such as:

   - **Finite Difference Method**: Discretize the vertical domain into grid points and solve the resulting matrix eigenvalue problem.

- **Shooting Method**: Integrate the differential equation from the surface to the bottom and adjust the phase speed c until the boundary conditions are satisfied.

B.5 Haline Contraction and Thermal Expansion in Seawater

Haline contraction and thermal expansion are key physical properties that determine how seawater density responds to changes in salinity and temperature. These mechanisms are essential for understanding ocean dynamics, influencing circulation, stratification, and mixing processes in the ocean.

B.5.1 Haline contraction

Haline contraction describes the increase in seawater density as salinity rises. When more salts dissolve in the water, the overall mass per unit volume increases, resulting in higher density. The haline contraction coefficient (β) quantifies how seawater density varies in response to changes in salinity and is given by:

$$\beta = \frac{1}{\rho_0}\left(\frac{\partial \rho}{\partial S}\right)_T \tag{B.2}$$

where, ρ_0 is reference density, rho is the density of sea water, S is salinity and T is constant temperature.

Haline contraction is most significant in regions where evaporation exceeds precipitation, such as subtropical gyres, or where sea ice formation leaves behind saltier water, such as in polar regions. Salty water is denser than freshwater and tends to sink, driving deep ocean currents and contributing to the global thermohaline circulation.

B.5.2 Thermal Expansion

Thermal expansion refers to the tendency of water to become less dense (expand) as its temperature increases. As seawater is heated, the kinetic energy of the water molecules increases, causing them to move apart and occupy more space. This reduces the overall density of the water. The degree to which seawater expands with temperature is characterized by the thermal expansion coefficient (α), defined as:

$$\alpha = -\frac{1}{\rho_0}\left(\frac{\partial \rho}{\partial T}\right)_S \tag{B.3}$$

where, ρ_0 is reference density, rho is the density of sea water, S is constant salinity and T is the temperature.

For typical seawater, the thermal expansion coefficient increases with both rising temperature and salinity. In warm tropical regions, this effect is particularly pronounced, contributing to significant stratification of the water column.

B.5.3 Combined effects

The interplay between haline contraction and thermal expansion is the driving force behind thermohaline circulation, a vital component of the global ocean system characterized by large-scale currents shaped by density differences stemming from variations in temperature and salinity. In colder regions, the effects of haline contraction dominate, resulting in denser water that sinks to the depths of the ocean, while in warmer areas, thermal expansion decreases density, allowing water to rise and spread out.

This complex interaction not only facilitates vertical and horizontal movement of seawater but also plays a crucial role in regulating climate by redistributing heat and nutrients throughout the world's oceans. As warm, nutrient-rich surface waters flow toward the poles, they cool and sink, creating a dynamic system that influences weather patterns and marine ecosystems.

Understanding these processes is essential for accurately modeling ocean circulation, assessing the impacts of climate change, and predicting sea-level rise. As global temperatures continue to rise and salinity patterns shift, the delicate balance of thermohaline circulation becomes increasingly important for maintaining the health of the oceans.

B.6 Thermohaline circulation in Bay of Bengal

The Bay of Bengal, a large and dynamic body of water bordered by India, Bangladesh, and Myanmar, is significantly influenced by thermohaline circulation, which is driven by variations in temperature and salinity. This circulation is essential for understanding the region's ocean dynamics, as it plays a crucial role in nutrient distribution, climate regulation, and marine ecosystem health.

B.6.1 Freshwater Input and Salinity Gradients

One of the most significant factors affecting thermohaline circulation in the Bay of Bengal is the influx of freshwater from major rivers such as the Ganges, Brahmaputra, and Meghna. These rivers discharge substantial volumes of freshwater into the bay, resulting in lower salinity levels near the river mouths. This freshwater input creates a stratified water column, where less dense, lower-salinity surface waters float above denser, saltier waters. The salinity gradient is a critical driver of density differences, leading to the vertical and horizontal movement of seawater.

B.6.2 Seasonal Variability

The seasonal variations in the Bay of Bengal, especially during the monsoon season, have a significant effect on thermohaline circulation. This period sees heavy rainfall and increased river discharge, which elevate freshwater levels and subsequently reduce surface salinity, disrupting circulation patterns. Conversely, during the dry season, higher evaporation rates can raise salinity and density in certain regions, causing water to sink and trigger downward currents.

B.6.3 Nutrient Transport and Marine Productivity

Thermohaline circulation is crucial for nutrient transport within the Bay of Bengal, significantly influencing the region's marine ecosystem. As currents carry nutrient-rich waters from the depths to the surface, they bolster productivity, sustaining vital fisheries that support local communities. This dynamic circulation not only enhances the availability of essential nutrients but also facilitates the upwelling of cold, nutrient-dense water, which is fundamental for the growth of phytoplankton the foundation of the marine food web.

Furthermore, the interplay between thermohaline circulation and local biogeochemical processes fosters a diverse and vibrant ecosystem, contributing to rich biodiversity. Various marine species, including commercially important fish, thrive in these nutrient-laden waters, making the bay an essential area for both fishing communities and marine life. By supporting various habitats, such as mangroves and coral reefs, thermohaline circulation helps maintain the ecological balance, underscoring the bay's significance not only as a resource for local economies but also as a critical environment for global marine health.

References

[1] R. Paris, A. Switzer, M. Belousova, A. Belousov, B. Ontowirjo, P. Whelley, and M. Ulvrova, "Volcanic tsunami: a review of source mechanisms, past events and hazards in southeast asia (indonesia, philippines, papua new guinea)," *Natural Hazards*, vol. 70, pp. 447–470, 2014.

[2] B. Mutaqin, F. Lavigne, D. Hadmoko, and M. Ngalawani, "Volcanic eruption-induced tsunami in indonesia: A review," in *IOP Conference Series: Earth and Environmental Science*, vol. 256-1, p. 012023, IOP Publishing, 2019.

[3] NOAA, "Ripple effect: What the Tonga eruption could mean for tsunami research," *NOAA. Webpage accessed on 11/09/2023, https://www.noaa.gov/news/ripple-effect-what-tonga-eruption-could-mean-for-tsunami-research*, 2022.

[4] A. Gusman and J. Roger, "Hunga Tonga-Hunga Ha'apai volcano-induced sea level oscillations and tsunami simulations," *GNS Sci. Webpage accessed on 31/01/2023*, 2022.

[5] N. Iverson, R. Lieb-Lappen, N. Dunbar, R. Obbard, E. Kim, and E. Golden, "The first physical evidence of subglacial volcanism under the west antarctic ice sheet," *Scientific Reports*, vol. 7, no. 1, p. 11457, 2017.

[6] S. Pegler and D. Ferguson, "Rapid heat discharge during deep-sea eruptions generates megaplumes and disperses tephra," *Nature Communications*, vol. 12, no. 1, p. 2292, 2021.

[7] J. Crisp, "Rates of magma emplacement and volcanic output," *Journal of Volcanology and Geothermal Research*, vol. 20, no. 3-4, pp. 177–211, 1984.

[8] S. Beaulieu, T. Graedel, and M. Hannington, “Should we mine the deep seafloor?,” *Earth’s Future*, vol. 5, no. 7, pp. 655–658, 2017.

[9] C. Van Dover, C. German, K. Speer, L. Parson, and R. Vrijenhoek, “Evolution and biogeography of deep-sea vent and seep invertebrates,” *Science*, vol. 295, no. 5558, pp. 1253–1257, 2002.

[10] S. Sander and A. Koschinsky, “Metal flux from hydrothermal vents increased by organic complexation,” *Nature Geoscience*, vol. 4, no. 3, pp. 145–150, 2011.

[11] D. Butterfield, G. Massoth, R. McDuff, J. Lupton, and M. Lilley, “Geochemistry of hydrothermal fluids from axial seamount hydrothermal emissions study vent field, juan de fuca ridge: Subseafloor boiling and subsequent fluid-rock interaction,” *Journal of Geophysical Research: Solid Earth*, vol. 95, no. B8, pp. 12895–12921, 1990.

[12] J. Lupton, E. Baker, and G. Massoth, “Helium, heat, and the generation of hydrothermal event plumes at mid-ocean ridges,” *Earth and Planetary Science Letters*, vol. 171, no. 3, pp. 343–350, 1999.

[13] WHOI, “Five new hydrothermal vents discovered in the eastern tropical pacific ocean,” *Woods Hole Oceanographic Institution, https://www.whoi.edu/press-room/news-release/five-new-hydrothermal-vents-discovered-in-the-eastern-tropical-pacific-ocean/*, 2024.

[14] K. Rubin, S. Soule, W. Chadwick Jr, D. Fornari, D. Clague, R. Embley, E. Baker, M. Perfit, D. Caress, and R. Dziak, “Volcanic eruptions in the deep sea,” *Oceanography*, vol. 25, no. 1, pp. 142–157, 2012.

[15] D. Leonard, “The hidden power of submarine volcanoes,” *ScienceLine, https://scienceline.org/2022/05/the-hidden-power-of-submarine-volcanoes/*, 2022.

[16] J. Terry, J. Goff, N. Winspear, V. Bongolan, and S. Fisher, “Tonga volcanic eruption and tsunami, january 2022: globally the most significant opportunity

to observe an explosive and tsunamigenic submarine eruption since ad 1883 krakatau," *Geoscience Letters*, vol. 9, pp. 1–11, 2022.

[17] WHOI, "Submarine volcanoes: Mother nature's incredible phenomenon," *Ocean Info, Woods Hole Oceanographic Institution, https://oceaninfo.com/ocean/geology/submarine-volcanoes/*, 2019.

[18] A. Mahadevan, J. Oliger, and R. Street, "A nonhydrostatic mesoscale ocean model. part i: Well-posedness and scaling," *Journal of Physical Oceanography*, vol. 26, no. 9, pp. 1868–1880, 1996.

[19] A. Mahadevan, J. Oliger, and R. Street, "A nonhydrostatic mesoscale ocean model. part ii: Numerical implementation," *Journal of Physical Oceanography*, vol. 26, no. 9, pp. 1881–1900, 1996.

[20] A. Constantin and R. Johnson, "A nonlinear, three-dimensional model for ocean flows, motivated by some observations of the Pacific Equatorial Undercurrent and thermocline," *Physics of Fluids*, vol. 29, pp. 56–64, 2017.

[21] B. Basu, "On a three-dimensional nonlinear model of pacific equatorial ocean dynamics: velocities and flow paths," *Oceanography*, vol. 31, no. 3, pp. 51–58, 2018.

[22] D. Smith and T. Jordan, "Seamount statistics in the Pacific Ocean," *Journal of Geophysical Research: Solid Earth*, vol. 93, no. B4, pp. 2899–2918, 1988.

[23] E. Newland, N. Mingotti, and A. Woods, "Dynamics of deep-submarine volcanic eruptions," *Scientific reports*, vol. 12, no. 1, p. 3276, 2022.

[24] R. Cahalan and J. Dufek, "Explosive submarine eruptions: The role of condensable gas jets in underwater eruptions," *J. Geophysical Research: Solid Earth*, vol. 126, pp. 2169–9313, 2021.

[25] D. Clague, R. Batiza, J. Head III, and A. Davis, "Pyroclastic and hydroclastic deposits on loihi seamount, hawaii," *Geophysical Monograph Series*, vol. 140, pp. 73–95, 2003.

[26] M. Garcia, K. Rubin, M. Norman, J. Rhodes, D. Graham, D. Muenow, and K. Spencer, “Petrology and geochronology of basalt breccia from the 1996 earthquake swarm of loihi seamount, hawaii: magmatic history of its 1996 eruption,” *Bulletin of Volcanology*, vol. 59, pp. 577–592, 1998.

[27] A. Watts, C. Peirce, I. Grevemeyer, M. Paulatto, W. Stratford, D. Bassett, J. Hunter, L. Kalnins, and C. De Ronde, “Rapid rates of growth and collapse of monowai submarine volcano in the kermadec arc,” *Nature Geoscience*, vol. 5, no. 7, pp. 510–515, 2012.

[28] I. Wright, W. Chadwick Jr, C. de Ronde, D. Reymond, O. Hyvernaud, H. Gennerich, P. Stoffers, K. Mackay, M. Dunkin, and S. Bannister, “Collapse and reconstruction of monowai submarine volcano, kermadec arc, 1998–2004,” *Journal of Geophysical Research: Solid Earth*, vol. 113, no. B8, 2008.

[29] W. Chadwick Jr, S. Nooner, D. Butterfield, and M. Lilley, “Seafloor deformation and forecasts of the april 2011 eruption at axial seamount,” *Nature Geoscience*, vol. 5, no. 7, pp. 474–477, 2012.

[30] H. Staudigel, S. Hart, A. Pile, B. Bailey, E. Baker, S. Brooke, D. Connelly, L. Haucke, C. German, I. Hudson, *et al.*, “Vailulu’u seamount, samoa: Life and death on an active submarine volcano,” *Proceedings of the National Academy of Sciences*, vol. 103, no. 17, pp. 6448–6453, 2006.

[31] J. Ibáñez, S. De Angelis, A. Díaz-Moreno, P. Hernández, G. Alguacil, A. Posadas, and N. Pérez, “Insights into the 2011–2012 submarine eruption off the coast of el hierro (canary islands, spain) from statistical analyses of earthquake activity,” *Geophysical Journal International*, vol. 191, no. 2, pp. 659–670, 2012.

[32] C. López, M. Blanco, R. Abella, B. Brenes, V. Cabrera Rodríguez, B. Casas, I. Domínguez Cerdeña, A. Felpeto, M. F. de Villalta, C. Del Fresno, *et al.*, “Monitoring the volcanic unrest of el hierro (canary islands) before the onset of the 2011–2012 submarine eruption,” *Geophysical Research Letters*, vol. 39, no. 13, 2012.

[33] S. Manneela and S. Kumar, "Overview of the Hunga Tonga-Hunga Ha'apai volcanic eruption and tsunami," *Journal of the Geological Society of India*, vol. 98, no. 3, pp. 299–304, 2022.

[34] D. Squires, "Report on myojinsho (japan)," *Scientific Event Alert Network Bulletin*, vol. 4, no. 7, 1979. Smithsonian Institution.

[35] G. Li, L. Cheng, J. Zhu, K. Trenberth, M. Mann, and J. Abraham, "Increasing ocean stratification over the past half-century," *Nature Climate Change*, vol. 10, no. 12, pp. 1116–1123, 2020.

[36] E. Olmedo, A. Turiel, V. González-Gambau, C. González-Haro, A. García-Espriu, C. Gabarró, M. Portabella, I. Corbella, M. Martín-Neira, M. Arias, *et al.*, "Increasing stratification as observed by satellite sea surface salinity measurements," *Scientific reports*, vol. 12, no. 1, p. 6279, 2022.

[37] D. Thomas and D. Bowers, *Introducing oceanography*. Dunedin Academic Press Ltd, 2021.

[38] E. Pelinovsky, "Nonlinear dynamics of tsunami waves," *Applied Physics Institute Press, Gorky*, 1982.

[39] M. Smith and J. Shepherd, "Preliminary investigations of the tsunami hazard of Kick'em Jenny submarine volcano," *Natural Hazards*, vol. 7, pp. 257–277, 1993.

[40] M. Nakano, S. Unoki, M. Hanzawa, R. Marumo, and J. Fukuoka, "Oceanographic features of a submarine eruption that destroyed the kaiyo-maru no. 5," *Journal of Marine Research*, vol. 13, pp. 48–66, 1954.

[41] H. Miyoshi and Y. Akiba, "The tsunamis caused by the Myojin explosions," *Journal of the Oceanographical Society of Japan*, vol. 10, pp. 49–59, 1954.

[42] R. Dietz and M. Sheehy, "Transpacific detection of myojin volcanic explosions by underwater sound," *Geological Society of America Bulletin*, vol. 65, pp. 941–956, 1954.

[43] R. Cooke, "Eruptive history of the volcano at ritter island," *Geological Survey Papua New Guinea Mem*, vol. 10, pp. 115–123, 1981.

[44] W. Palfreyman, D. Wallace, and R. Cooke, "Langila volcano: summary of reported eruptive history, and eruption periodicity from 1961 to 1972," *Cooke-Ravian Volume of Volcanological Papers. Geological Survey of Papua New Guinea Memoir*, vol. 10, pp. 125–33, 1981.

[45] L. Mastin and J. Witter, "The hazards of eruptions through lakes and seawater," *Journal of Volcanology and Geothermal Research*, vol. 97, pp. 195–214, 2000.

[46] Y. Muraviev, S. Fedotov, V. Budnikov, A. Ozerov, M. Maguskin, V. Dvigalo, V. Andreev, V. Ivanov, L. Kartasheva, and I. Markov, "Volcanic activity in the Karymsky center in 1996: Summit eruption at Karymsky and phreatomagmatic eruption in the Akademii Nauk Caldera," *Journal of volcanology and Seismology*, vol. 19, pp. 567–604, 1998.

[47] A. Belousov, B. Voight, M. Belousova, and Y. Muravyev, "Tsunamis generated by subaquatic volcanic explosions: unique data from 1996 eruption in Karymskoye lake, Kamchatka, Russia," *Pure and Applied Geophysics*, vol. 157, pp. 1135–1143, 2000.

[48] A. Belousov and M. Belousova, "Eruptive process, effects and deposits of the 1996 and the ancient basaltic phreatomagmatic eruptions in Karymskoye lake, Kamchatka, Russia," *Volcaniclastic Sedimentation in Lacustrine Settings*, pp. 35–60, 2001.

[49] M. Heidarzadeh, A. Gusman, T. Ishibe, R. Sabeti, and J. Šepić, "Estimating the eruption-induced water displacement source of the 15 January 2022 Tonga volcanic tsunami from tsunami spectra and numerical modelling," *Ocean Engineering*, vol. 261, p. 112165, 2022.

[50] T. Kubota, T. Saito, and K. Nishida, "Global fast-traveling tsunamis driven by atmospheric Lamb waves on the 2022 Tonga eruption," *Science*, p. eabo4364, 2022.

[51] M. Yamada, T. Ho, J. Mori, Y. Nishikawa, and M. Yamamoto, "Tsunami triggered by the Lamb wave from the 2022 Tonga volcanic eruption and transition in the offshore Japan region," *Geophysical Research Letters*, vol. 49, p. e2022GL098752, 2022.

[52] B. Le Méhauté and S. Wang, *Water waves generated by underwater explosion*, vol. 10. World Scientific, 1996.

[53] T. Torsvik, R. Paris, I. Didenkulova, E. Pelinovsky, A. Belousov, and M. Belousova, "Numerical simulation of a tsunami event during the 1996 volcanic eruption in Karymskoye lake, Kamchatka, Russia," *Natural Hazards and Earth System Sciences*, vol. 10, pp. 2359–2369, 2010.

[54] R. Paris, "Source mechanisms of volcanic tsunamis," *Philosophical Transactions of the Royal Society A: Mathematical, Physical and Engineering Sciences*, vol. 373, 2015.

[55] R. Paris and M. Ulvrova, "Tsunamis generated by subaqueous volcanic explosions in Taal Caldera lake, philippines," *Bulletin of Volcanology*, vol. 81, pp. 1–14, 2019.

[56] V. Kedrinskii, *Hydrodynamics of Explosion: experiments and models.* Springer Science & Business Media, 2005.

[57] M. Morrissey, G. Gisler, R. Weaver, and M. Gittings, "Numerical model of crater lake eruptions," *Bulletin of Volcanology*, vol. 72, pp. 1169–1178, 2010.

[58] J. Moore, K. Nakamura, and A. Alcaraz, "The september 28–30, 1965 eruption of Taal Volcano, Philippines," *Bulletin Volcanologique*, vol. 29, pp. 75–76, 1966.

[59] Y. Nishimura, M. Nakagawa, J. Kuduon, and J. Wukawa, "Timing and scale of tsunamis caused by the 1994 Rabaul eruption, East New Britain, Papua New Guinea," in *Tsunamis*, pp. 43–56, Springer, 2005.

[60] D. Duffy, "On the generation of oceanic surface waves by underwater volcanic explosions," *Journal of Volcanology and Geothermal Research*, vol. 50, pp. 323–344, 1992.

[61] N. Lipiejko, C. N. Whittaker, E. Lane, J. White, and W. Power, “Tsunami generation by underwater volcanic explosions: Application to the 1952 explosions of Myojinsho Volcano,” *Pure and Applied Geophysics*, vol. 178, pp. 4743–4761, 2021.

[62] Y. Egorov, “Tsunami wave generation by the eruption of underwater volcano,” *Natural Hazards and Earth System Sciences*, vol. 7, pp. 65–69, 2007.

[63] S. Unoki and M. Nakano, “On the cauchy-poisson waves caused by the eruption of a submarine volcano (iii),” *Papers in Meteorology and Geophysics*, vol. 4, pp. 139–150, 1953.

[64] GFDRR, “The January 15, 2022 Hunga Tonga-Hunga Ha’apai eruption and tsunami, Tonga global rapid post disaster damage estimation (grade) report,” *Global Rapid Post Disaster Damage Estimation (GRADE) Report, Prepared in partnership with Government of Tonga, World Bank Group and GFDRR*, 2022.

[65] M. I. News, “Tonga eruption triggers peru oil spill.,” *https://marineindustrynews.co.uk/watch-tonga-eruption-triggers-peru-oil-spill/. Accessed:24 september 2023*, 2022.

[66] G. Dickie, “One year after volcanic blast, many of Tonga’s reefs lie silent, https://www.reuters.com/business/environment/one-year-after-volcanic-blast-many-Tonga’s-reefs-lay-silent-2023-01-15/ accessed 17 november 2023,” *Reuters*, p. 1, 2023.

[67] M. Clare, I. Yeo, S. Watson, R. Wysoczanski, S. Seabrook, K. Mackay, J. Hunt, E. Lane, P. Talling, and E. o. Pope, “Fast and destructive density currents created by ocean-entering volcanic eruptions,” *Science*, vol. 381, no. 6662, pp. 1085–1092, 2023.

[68] M. Clare, I. Yeo, L. Bricheno, Y. Aksenov, J. Brown, I. Haigh, T. Wahl, J. Hunt, C. Sams, J. Chaytor, *et al.*, “Climate change hotspots and implications for the global subsea telecommunications network,” *Earth-Science Reviews*, p. 104296, 2022.

[69] H. Jeffreys, "On fluid motions produced by differences of temperature and humidity," *Quarterly Journal of the Royal Meteorological Society*, vol. 51, no. 216, pp. 347–356, 1925.

[70] R. Huang, "Mixing and energetics of the oceanic thermohaline circulation," *Journal of Physical Oceanography*, vol. 29, no. 4, pp. 727–746, 1999.

[71] H. Rossby, "On thermal convection driven by non-uniform heating from below: an experimental study," in *Deep Sea Research and Oceanographic Abstracts*, vol. 12, pp. 9–16, Elsevier, 1965.

[72] T. Rossby, "Numerical experiments with a fluid heated non-uniformly from below," *Tellus A: Dynamic Meteorology and Oceanography*, vol. 50, no. 2, pp. 242–257, 1998.

[73] J. Mullarney, R. Griffiths, and G. Hughes, "Convection driven by differential heating at a horizontal boundary," *Journal of Fluid Mechanics*, vol. 516, pp. 181–209, 2004.

[74] S. Vogel and S. Tulaczyk, "Ice-dynamical constraints on the existence and impact of subglacial volcanism on west antarctic ice sheet stability," *Geophysical Research Letters*, vol. 33, no. 23, 2006.

[75] D. Blankenship, R. Bell, S. Hodge, J. Brozena, J. Behrendt, and C. Finn, "Active volcanism beneath the west antarctic ice sheet and implications for ice-sheet stability," *Nature*, vol. 361, no. 6412, pp. 526–529, 1993.

[76] H. Corr and D. Vaughan, "A recent volcanic eruption beneath the west antarctic ice sheet," *Nature Geoscience*, vol. 1, no. 2, pp. 122–125, 2008.

[77] J. Boyd, *Dynamics of the equatorial ocean.* Springer, 2018.

[78] A. Gill, *Atmosphere-ocean dynamics*, vol. 30. Academic press, 1982.

[79] A. Fedorov and J. Brown, "Equatorial waves. encyclopedia of ocean sciences," 2009.

[80] A. Constantin, “On the modelling of equatorial waves,” *Geophysical Research Letters*, vol. 39, p. L05602, 2018.

[81] A. Constantin and R. Ivanov, “Equatorial wave–current interactions,” *Communications in Mathematical Physics*, vol. 370, pp. 1–48, 2019.

[82] A. Constantin and R. Johnson, “On the nonlinear, three-dimensional structure of equatorial oceanic flows,” *Journal of Physical Oceanography*, vol. 49, no. 8, pp. 2029–2042, 2019.

[83] B. Basu, “Some numerical investigations into a nonlinear three-dimensional model of the pacific equatorial ocean flows,” *Deep Sea Research Part II: Topical Studies in Oceanography*, vol. 160, pp. 7–15, 2019.

[84] B. Morton, G. Taylor, and J. Turner, “Turbulent gravitational convection from maintained and instantaneous sources,” *Proceedings of the Royal Society of London. Series A. Mathematical and Physical Sciences*, vol. 234, no. 1196, pp. 1–23, 1956.

[85] J. McCreary Jr, “Modeling equatorial ocean circulation,” *Annual Review of Fluid Mechanics*, vol. 17, pp. 359–409, 1985.

[86] B. Basu, “On the nonlinear three-dimensional models in equatorial ocean flows,” *Communications on Pure and Applied Analysis*, vol. 21, p. 2271, 2022.

[87] B. Basu, “Some numerical investigations into a nonlinear three-dimensional model of Pacific equatorial ocean dynamics,” *Deep-Sea Res. IIs*, vol. 160, pp. 7–15, 2019.

[88] B. Basu, “On a three-dimensional nonlinear model of pacific equatorial ocean dynamics: Velocities and flow paths,” *Oceanography*, vol. 31, pp. 51–58, 2018.

[89] NOAA, “Underwater vents and volcanoes, https://oceantoday.noaa.gov/underwatervolcanoes// accessed 02-02-2024,” *NOAA Website*, p. 1, 2023.

[90] B. Basu and M. Kanojia, "Modelling the effect of submarine volcanic eruption on equatorial oceanic flows," *Nonlinear Analysis: Real World Applications*, vol. 74, p. 103956, 2023.

[91] R. Meakin and R. Street, "Simulation of environmental flow problems in geometrically complex domains. part i: A general coordinate transformation.," *Computer methods in applied mechanics and engineering*, vol. 68, no. 2, pp. 151–175, 1988.

[92] Y. Zang, R. Street, and J. Koseff, "A non-staggered grid, fractional step method for time-dependent incompressible navier-stokes equations in curvilinear coordinates.," *Journal of Computational physics*, vol. 114, no. 1, pp. 18–33, 1994.

[93] A. Mahadevan, "Modeling vertical motion at ocean fronts: Are nonhydrostatic effects relevant at submesoscales?," *Ocean Modelling*, vol. 14, no. 3-4, pp. 222–240, 2006.

[94] A. Mahadevan and A. Tandon, "An analysis of mechanisms for submesoscale vertical motion at ocean fronts," *Ocean Modelling*, vol. 14, no. 3-4, pp. 241–256, 2006.

[95] A. Mahadevan and D. Archer, "Modeling the impact of fronts and mesoscale circulation on the nutrient supply and biogeochemistry of the upper ocean," *Journal of Geophysical Research: Oceans*, vol. 105, no. C1, pp. 1209–1225, 2000.

[96] A. Mahadevan, A. Tandon, and R. Ferrari, "Rapid changes in mixed layer stratification driven by submesoscale instabilities and winds," *Journal of Geophysical Research: Oceans*, vol. 115, no. C3, 2010.

[97] A. Mahadevan and D. Archer, "Modeling a limited region of the ocean," *Journal of Computational Physics*, vol. 145, no. 2, pp. 555–574, 1998.

[98] A. Mahadevan, A. Pascual, D. Rudnick, S. Ruiz, J. Tintoré, and E. D'Asaro, "Coherent pathways for vertical transport from the surface ocean to interior," *Bulletin of the American Meteorological Society*, vol. 101, no. 11, pp. E1996–E2004, 2020.

[99] M. Freilich, C. Poirier, M. Dever, E. Alou-Font, J. Allen, A. Cabornero, L. Sudek, C. Choi, S. Ruiz, A. Pascual, *et al.*, “3d intrusions transport active surface microbial assemblages to the dark ocean,” *Proceedings of the National Academy of Sciences*, vol. 121, no. 19, p. e2319937121, 2024.

[100] G. Spiro Jaeger and A. Mahadevan, “Submesoscale-selective compensation of fronts in a salinity-stratified ocean,” *Science advances*, vol. 4, no. 2, p. e1701504, 2018.

[101] G. Spiro Jaeger, *Stratified and stirred: monsoon freshwater in the Bay of Bengal.* PhD thesis, Massachusetts Institute of Technology, 2019.

[102] S. Ruiz, A. Mahadevan, A. Pascual, M. Claret, J. Tintore, and E. Mason, “Multi-platform observations and numerical simulations to understand meso and submesoscale processes: A case study of vertical velocities in the western mediterranean,” *New Frontiers in Operational Oceanography*, pp. 117–130, 2018.

[103] S. Mukherjee, S. Ramachandran, A. Tandon, and A. Mahadevan, “Production and destruction of eddy kinetic energy in forced submesoscale eddy-resolving simulations,” *Ocean Modelling*, vol. 105, pp. 44–59, 2016.

[104] M. Freilich and A. Mahadevan, “Coherent pathways for subduction from the surface mixed layer at ocean fronts,” *Journal of Geophysical Research: Oceans*, vol. 126, no. 5, p. e2020JC017042, 2021.

[105] R. Laxenaire, S. Speich, B. Blanke, A. Chaigneau, and C. Pegliasco, “A new insight on the indo-atlantic exchange achieved by indian ocean eddies assessed by satellite altimetry and argo profiling float data.,” in *2016 Ocean Sciences Meeting*, AGU, 2016.

[106] G. Vieira, M. Allshouse, and A. Mahadevan, “Seagrass deformation affects fluid instability and tracer exchange in canopy flow,” *Scientific reports*, vol. 13, no. 1, p. 3910, 2023.

[107] V. Tupitsyn and Y. Chashechkin, “Free convection above a point source of heat in a stratified fluid,” *Fluid Dynamics*, vol. 16, no. 2, pp. 180–188, 1981.

[108] Y. Chashechkin and V. Belyaev, "Regimes of free thermally concentrated convection over a point heat source," in *Soviet Physics Doklady*, vol. 27, p. 923, 1982.

[109] Y. Chashechkin and V. Tupitsyn, "Structure of free convective flow over a point source of heat in a stratified liquid," in *Soviet Phys.–Doklady*, vol. 24, pp. 862–864, 1979.

[110] H. Jones and J. Marshall, "Convection with rotation in a neutral ocean: A study of open-ocean deep convection," *Journal of Physical Oceanography*, vol. 23, no. 6, pp. 1009–1039, 1993.

[111] M. Kanojia, S. Gurusamy, and B. Basu, "Modeling of tsunami generated in stratified oceans by sub-aquatic volcanic eruptions," *Physics of Fluids*, vol. 35, no. 5, 2023.

[112] L. Sretenskii, "Theory of wave motions in a fluid," *Moscow Izdatel Nauka*, 1977.

[113] D. Henry and G. Villari, "Flow underlying coupled surface and internal waves," *Journal of Differential Equations*, vol. 310, pp. 404–442, 2022.

[114] D. Henry and G. Villari, "Flow dynamics for coupled surface and internal deep-water waves," *Annali di Matematica Pura ed Applicata (1923-)*, pp. 1–26, 2022.

[115] E. Baker, J. Lavelle, R. Feely, G. Massoth, S. Walker, and J. Lupton, "Episodic venting of hydrothermal fluids from the juan de fuca ridge," *Journal of Geophysical Research: Solid Earth*, vol. 94, no. B7, pp. 9237–9250, 1989.

[116] A. Quarteroni, R. Sacco, and F. Saleri, *Numerical mathematics*, vol. 37. Springer Science & Business Media, 2010.

[117] L. Shampine, "Vectorized adaptive quadrature in matlab," *Journal of Computational and Applied Mathematics*, vol. 211, no. 2, pp. 131–140, 2008.

[118] Y. Liu and H. Fritz, "Physical modeling of spikes during the volcanic tsunami generation," *Physics of Fluids*, vol. 35, no. 6, 2023.

[119] F. Schindelé, L. Kong, E. Lane, R. Paris, M. Ripepe, V. Titov, and R. Bailey, "A review of tsunamis generated by volcanoes (tgv) source mechanism, modelling, monitoring and warning systems," *Pure and Applied Geophysics*, pp. 1–48, 2024.